ROMA TRE
UNIVERSITÀ DEGLI STUDI

Department of Science
Graduate School in Earth Science - Geodynamics
XXXII PhD cycle

Modeling the Tectonic Styles of Icy Planetary Surfaces and their Terrestrial Analogs

---

by

COSTANZA ROSSI

Supervisor: Prof. Francesco Salvini

Co-Supervisor: Dr. Paola Cianfarra

2019

This thesis entitled:

Modeling the Tectonic Styles of Icy Planetary Surfaces and their Terrestrial Analogs

written by Costanza Rossi, has been reviewed and approved by:

- Dr. ERNST HAUBER, German Aerospace Center, Institute of Planetary Research, Planetary Geology.

- Prof. GORO KOMATSU, Università degli Studi "G. D'Annunzio", Dipartimento di Ingegneria e Geologia, International Research School of Planetary Sciences.

Table of Contents

ABSTRACT 4
CHAPTER 1 INTRODUCTION 6
1.1 Tectonics of icy surfaces: scientific perspectives 6
1.2 Ice properties 8
1.3 Investigated icy surfaces 10
1.4 Tectonic modeling 11
1.5 Dissertation outline 12
CHAPTER 2 GANYMEDE 14
2.1 Evidence of transpressional tectonics on the Uruk Sulcus region, Ganymede 14
Abstract 14
1. Introduction 14
2. Geological setting 15
3. High-Resolution Mosaic Preparation 18
4. Structural Analysis - Method 21
5. Structural analysis - Results 30
6. Lineament domain analysis 36
7. Discussion 43
8. Conclusions 49
2.2 Structural geology of Ganymede regional groove systems (60°N – 60°S) 51
Abstract 51
1. Introduction 51
2. Data 57
3. Structural mapping 57
4. Groove super - systems 63
5. Discussion 64
6. Conclusions 66
2.3 Terrestrial analog of Ganymede 68
CHAPTER 3 ENCELADUS 74
3.1 Tectonics of Enceladus South Pole: Block rotation of the Tiger Stripes 74
Abstract 74
1. Introduction 74
2. Geological and structural setting 77
3. Structural analyses and results 80
4. Discussion 92
5. Conclusions 99
3.2 Terrestrial analog of Enceladus 100
CHAPTER 4 MARS NORTHERN ICE CAP 103
4.1 The Tectonic origin of Planum Boreum spiral troughs, Mars 103
Abstract 103
1. Introduction 103

2. Mars North Pole 105
3. Data 109
4. Methods 111
5. Results 113
6. Structural evolution of the North Polar troughs 118
7. Discussion 121
8. Conclusions 125
CHAPTER 5 DISCUSSION 126
5.1 Study case comparison 126
5.1.1 Ganymede and Enceladus 126
5.1.2 Mars northern ice cap 127
5.1.3 Antarctica 127
5.2 Tectonic style endmembers 128
5.3 Topographic flattening 128
5.3.1 Thin-skinned tectonics and fault inversion 130
5.4 Geodynamic processes 131
5.4.1 Polar wander 131
5.4.2 Coriolis force 132
5.4.3 Flow 132
CHAPTER 6 CONCLUSIONS 134
6.1 Perspectives 136
ACKNOWLEDGEMENTS 137
REFERENCES 138

ABSTRACT

Tectonics on icy surfaces of the Solar System present a number of issues relevant for understanding the geologic evolution and the geodynamic processes of icy bodies. The recognized strong evidence of extensional tectonic regimes and the paucity of compressional structures leave unclear their structural balancing. This assumption opens the issue on the existence of a prevalent tectonic regime and a preferential style of deformation affecting the icy planetary surfaces. The present dissertation addresses this problem by improving our understanding on the tectonic regimes that deform the icy surfaces. The investigation is performed by the modeling of the tectonic setting of selected study areas in confined (closed) and unconfined (open) icy surfaces. These were identified in the icy satellites Ganymede and Enceladus (confined study cases), and in the northern polar cap of Mars (unconfined study case). Their comparison with their terrestrial analogs, identified in the Antarctic ice sheet, supports the investigation.

The tectonic structures in the investigated regions are studied by a multidisciplinary structural geology approach that includes remote sensing, structural mapping, geomorphology, and quantitative (geo)statistical analyses. A total of three tectonic models are prepared and describe the kinematic evolution of the investigated icy surfaces.

Ganymede model suggests transpressional tectonics in the Uruk Sulcus region, and the identification of regional groove systems proposed in the structural map of Ganymede grooves allow to recognize significant regional strike-slip tectonics affecting its surface. Transpression is also recognized by the model proposed in the South Polar Terrain of Enceladus, where block rotation tectonics characterizes the Tiger Stripes kinematics. The tectonic model proposed for the northern polar cap of Mars attributes the origin and evolution of the spiral troughs to the activity of low-angle normal faults that fade in a ductile detachment at depth.

These models allow to recognize two endmembers of tectonic styles affecting the icy planetary surfaces. Strike-slip and low-angle dip-slip faulting characterize their regional scale tectonics. These endmembers are framed into a preferential way of deformation that follows the thin-skinned model and contributes to preserve the overall flat topography of the icy surfaces. The obtained results open the discussion on the possible geodynamic implications related to the polar wander, the Coriolis force and the ice flow.

CHAPTER 1

INTRODUCTION

1.1 Tectonics of icy surfaces: scientific perspectives

From the mid-1900s the consciousness that ice is a common component throughout the solar system was developed (Whipple, 1950; Kuiper, 1952). Ice is present since the birth of the solar system, and its distribution depends on how it originally formed from the solar nebula (Prockter, 2005). Many volatiles of ice occur in the solar system and the most familiar is the water ice that presents approximately 15 different crystalline forms where the water molecules become more densely packed as pressure is increased (from ice-Ih, present in the Earth, to high-pressure ice-VIII). It is present both as polar caps and as ground ice in permafrost regions of rocky bodies, such as the Earth and Mars, and as the main component, in the comets and in several outer system bodies and satellites. Icy worlds are sites of extreme scientific interest in planetary exploration from the geological and astrobiological point of view. Many of them present subsurface liquid water layers that are considered potential habitable environments to host life beyond the Earth. In this way, their icy surface characteristics provide information on their formation and evolution, and on the eventual underlying ocean.

As the rocky surfaces, the icy ones present tectonic features. Brittle failure in Earth glacial environments is frequent as well as the abundance of tectonics in icy planetary surfaces. Tectonics in Solar System bodies is often referred to as “tectonism” to avoid the confusion with Earth plate-tectonics. This dissertation refers to “tectonics” as deformational activity and processes that control structural evolution. In the Solar System, tectonics in rocky bodies is one of the most important processes that affect the surfaces. This also applies to the icy surfaces that require a separate description to understand what tectonics of icy surfaces reveals and which information it provides. Icy surface tectonics is relevant for the understanding of the geologic evolution and the geodynamic processes of an icy body. These present complex features that are often difficult to unravel, and their

formation relates to puzzling origin, that might be misinterpreted. When their tectonic origin is defined, this provides knowledge about what these features exhibit. Tectonic features in icy environments provide information on the internal setting and represent possible way of interchange between surface and deep layers (i.e. ocean when present; Prockter, 2005, Porco et al., 2006). They allow to infer the direction and (possibly) the amount of the driving stresses. The investigation of the ice deformation represents also a predictive means to identify the fracturing preferential ways for atmosphere-inner body exchanges.

The Solar System icy surfaces exhibit evidence for tectonic features of extensional origin, rather than compressional origin that appears to be rare (Parmentier and Head, 1979). Almost every deformed icy surface show evidence for extensional tectonic feature, while minor evidence of strike-slip is observed, and compression features are rarely observed. This opens the debate to answer several questions connected with the problem of the balancing of the recognized extensional processes. The amount of extension should be somehow balanced, and the lack of compressional features and the strike-slip paucity make difficult the solution of this problem.

In this way, this dissertation attempts to improve our understanding on the tectonic regimes that deform the icy surfaces. Is extension the main tectonic process or other regimes play a similar role to deform the icy surfaces? Are there other tectonic processes that were not yet recognized due to their complex interpretation? How the recognized tectonic styles contribute to balance the acting stresses? Which geodynamic processes could frame the recognized tectonic setting?

From the general point of view, this project was born and focuses to verify whether icy surfaces develop preferential ways of deformation (dip- and strike-slip). Despite the amount of information gathered in the last 50 years of space exploration, many features of icy surfaces remain still unexplained. In this way, the tectonic setting modeling of deformed region in icy surfaces can be performed, and the structural geology approach to this issue is decisive.

This is the starting point for the formulation of the "Modeling the tectonic styles of icy planetary surfaces and their terrestrial analogs" project. This dissertation aims to unravel the tectonic setting observed at the regional scale in icy planetary surfaces. It addresses two topics: tectonic modeling of icy surface regions and comparison among the case studies.

Results of this work will show how the local scale features are part of a larger scale mechanism that frames several tectonic styles. Resulting evidence of tectonic deformation is discussed, by taking into account possible processes of formation. The investigation begins from the modeling of study areas in the icy satellites Ganymede and Enceladus, then moves to modeling of the features of the northern ice cap of Mars, and finally to the comparison with terrestrial analogs in Antarctica. Thus, from the regional-scale investigation of surface features (Ganymede, Enceladus), to the buried structures by cross-sections (Mars). The tectonic styles found in icy surfaces represent the common thread that links the case studies, and the comparison represents the foundation that connects and frames this study. The proposed models allow to recognize two main tectonic styles formed in a preferential way of deformation that refers to thin-skinned tectonics in icy planetary surfaces.

1.2 Ice properties

In the Solar System the rocks and ices provide precise distribution, and their proportion variates with distance from the Sun. Their amount depends to the "frost line" that represents the line between the areas where rocks and metals condense (closer to the Sun) and where carbon and ice grains begin to condense (away from the Sun; Prockter, 2005). Many volatiles can exist in frozen form, and several types of ices have been found in the Solar System. The most familiar is water ice that often includes other volatiles such as methane, nitrogen, CO_2, and noble gases in the lattice (Prockter, 2005). At the pressure and temperature variation, water ice reorganizes its structure. The terrestrial form of the water ice is the ice-I (or ice-Ih), and it undergoes phase transformations to denser phases at elevated pressures (Fig. 1). The rheological properties of high-pressure ice phases are not as well-known as the properties of ice-I. These are typically only found at depths of several hundred kilometers within

the largest icy satellites (ice-III, ice-V, ice-VI; e.g. Hussman et al., 2007), and are usually less directly relevant to near-surface tectonic processes. In this way, this dissertation will consider ice-I that will be simply mentioned as ice.

Its density, lower than its molten equivalent (water), makes the surface eruption of water difficult (when subsurface liquid water layer/ocean occur). From the tectonics point of view, ice is rather similar to silicate materials, and a close parallelism between the behavior of ice and the behavior of rocks under stress exists (Chamberlin, 1936; Jaumann et al., 2009). At near surface conditions its behavior is brittle, while at greater depths it is ductile. At the surface, ice behavior resembles that of rocks on Earth. Indeed, many tectonic features observed on icy surfaces have terrestrial counterparts. Ice is intrinsically weaker than rock, in that it is less rigid (lower Young's modulus around 1-11 GPa, Petrovic, 2003; Nimmo, 2004) and close to its melting point flows more readily than silicates (Chamberlin, 1936). Thus, viscous flow timescales are much shorter in icy surfaces than in their silicate equivalents, and a ductile layer may be shallower, with more influence on the surface, than in the terrestrial context (Collins et al., 2009; Watters and Schultz, 2010). An ice layer in the upper crust of an icy satellite can be modelled as a simple elastic layer that may be influenced by a near-surface ductile layer beneath. In this way, this thesis addresses the issue with the structural geology approach and relates the ice behavior under deforming stresses to the rock mechanical principles.

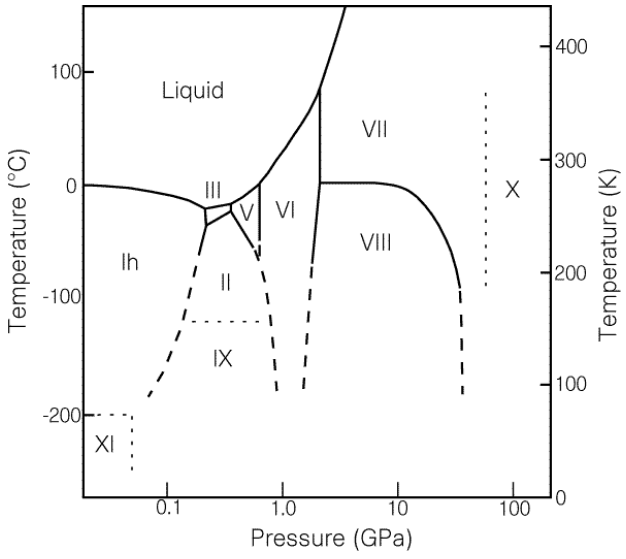

Fig. 1: Phase diagram of pure water ice. The different high-pressure ice phases are shown. Most relevant for the icy satellites are ice-I, ice-II, ice-III, ice-V and ice-VI (Hussman et al., 2007).

1.3 Investigated icy surfaces

This dissertation focuses on investigating a series of study areas and to compare them. Icy surfaces are considered, not limiting the work on icy satellite crusts. The complete investigation concerns tectonic features in map-view and in section. In this way, several bodies present two distinct types of icy surfaces: confined and unconfined icy surfaces. Confined icy surfaces refer to "enclosed" systems where mass deformation has to be balanced in the same space, and the unconfined ones refer to "open" systems where space availability exists. Study areas of confined icy surfaces were selected in the icy satellites Ganymede and Enceladus, and the unconfined investigated icy surface is represented by the Mars north polar caps. These were compared with their terrestrial analogs in Antarctica.

The icy satellites Ganymede and Enceladus belong to two systems, the jovian system and the saturnian one. These present a global (Ganymede) or regional (possibly Enceladus) liquid ocean underlying their icy crusts, deformed by internal activity (Ganymede) often tidally driven (Enceladus). These satellites present past (Ganymede) or present (Enceladus) tectonic activity that formed globally widespread (Ganymede) or localised (Enceladus) tectonic features. For these satellites, their icy composition and surface temperature makes difficult to get liquid ocean water up to the icy surface. This should either be forced upward through over pressurized cracks, or reduced density such as by gas bubbles, or else tectonic regimes that could contribute to the rising of internal material at the surface.

Ganymede opens the investigation. This satellite presents a global ocean that underlies an icy surface globally deformed by tectonic features. The strike-slip regime of Uruk Sulcus is studied, with the mapping and classification of regional-scale systems of tectonic features that characterize the results of the ancient tectonics that affected its surface.

Enceladus internal activity is centered at its south polar region, where plumes depart, and complex setting of tectonic features deforms its surface. Block rotation tectonics allows to unravel the south pole tectonic evolution.

These two case studies refer to the modeling of features in map-view in confined icy surfaces. The third one considers the third dimension, and is located in the unconfined Mars northern ice cap. The modeling of their structure at depth allows to understand the internal dynamics of the cap and the behavior that ice failure provides at depth.

Although the tectonic features of the icy planetary surfaces have also rocky analogies on Earth, to better frame this issue the terrestrial analog is maintained in icy environment and it is represented by the Antarctica ice sheet. This is an unstable polar cap (formed at about 34 Ma) that presents dynamics and features similar to those observed both in the icy satellites and in the polar cap of Mars.

All these study areas present in a different way brittle deformation that creates weakness features, fractures and faults.

1.4 Tectonic modeling

The investigation of the study areas allows to prepare tectonic models that represent the evolution of the region under consideration. These are developed by using the data from the Outer Solar System missions (e.g. Voyager, Galileo, Cassini), and the mission to Mars (e.g. Mars Reconnaissance Orbiter). By means of the original approach of remote sensing, structural geology, statistical, and quantitative analyses a total of three regional-scale tectonic models are proposed.

Structural mapping and azimuthal analysis allow to recognize and classify tectonic feature populations into systems. The statistical analyses of their characteristics (e.g. the Length/Spacing ratio; L/S), their integration and relation with found lineament domains within the study area allow to relate systems to tectonic activity and to infer the tectonic styles that affect the areas. A new method of image processing (used for Enceladus south pole region) is proposed to confirm the recognized regimes. Balanced cross-sections (by Hybrid Cellular Automata methodology, HCA) allow to model the deep structure evolution of the tectonic features (used for the Mars case study and its Antarctic analog). In this way, the proposed evolutionary tectonic models describe both the dynamics and kinematics that create the investigated tectonic features. The three proposed tectonic models are then

compared. Several investigation scales relate to the same tectonic interpretation where each model shows several tectonic styles framed into a unique regional-scale event responsible of the local-scale tectonics. Ganymede and Enceladus models depict the evolution of the brittle deformation of their icy crusts; Mars model describes the cross-section evolution of the internal ice cap dynamics. Analogies with Antarctica are discussed to relate the results in icy surfaces with what known on Earth. The tectonic modeling allows to identify the main tectonic styles. Obtained result comparison allows to infer differences and analogies, and to recognize two endmembers that characterize icy surface tectonics. These are represented by strike-slip and low-angle dip-slip that suggest the preferential way of ice deformation exhibited by thin-skinned tectonics (Rodgers, 1949; Harris and Milici, 1977; Vendeville and Jackson, 1992; Lundin, 1992; Lankreijer et al., 1995; Pfiffner, 2017). Findings allow to infer geodynamic implications.

1.5 Dissertation outline

Part of this thesis is divided into a collection of articles. The flow of chapters represents the passage from the tectonics of the Outer Solar System icy surfaces to the terrestrial-type ice caps.

The ice tectonic topics are investigated in detail to reach the conclusion that two tectonic style endmembers affect icy surfaces. Obtained results show that strike-slip regime is significant for the confined icy satellite crusts and low-angle dip-slip regime play a secondary role. On the other hand, in unconfined ice cap low-angle dip-slip structures prevail and follow flow directions accommodated by secondary strike-slip regimes.

In Chapter 2 the case study Ganymede and its tectonic features are considered. Structural geology analysis is performed in a study area, called Uruk Sulcus, and in turn extended to the satellite surface in order to prepare the structural map of the tectonic features of Ganymede. This chapter includes the scientific papers “Evidence of transpressional tectonics on the Uruk Sulcus region, Ganymede” and “Structural geology of Ganymede regional groove system (60°N – 60°S)”. The first is a published article that presents the study of Uruk Sulcus region, deformed by transpressional kinematics. The

second represents a published paper, where the tectonic features of Ganymede surface are classified into regional systems and are object of further structural investigations. The last paragraph shows the structures recognized in the Rennick glacier in Antarctica that present analogies with Ganymede grooves setting.

Chapter 3 concerns Enceladus tectonics. The paper "Tectonics of Enceladus South Pole: Block rotation of the Tiger Stripes" presents the kinematic model of the South Polar Terrain of the satellite, where recent tectonic activity is reported. Enceladus icy surface presents regional strike-slip that frames into block rotation tectonics. The second section show its Antarctic analog.

Chapter 4 presents the results of "The tectonic origin of Planum Boreum spiral troughs, Mars". In this paper, the depth of the northern ice cap of Mars is investigated by analysing radargrams. The internal dynamic model of the cap is presented. It proposes the structural origin of the spiral troughs of Mars north pole. This section supports the suggestion that the spiral troughs are structural features that testify the deformational history of the ice cap.

In Chapter 5 the correlation of the mentioned study cases is discussed in order to identify differences and analogies. This comparison allows to propose two tectonic style endmembers characterized by the prevalence of thin-skinned tectonics in icy planetary surfaces. The discussion opens to possible geodynamic processes.

Chapter 6 presents the conclusions and the perspective for further investigations in preparation of the future mission programs (e.g. ESA Jupiter Icy Moons Explorer and NASA Europa Clipper).

CHAPTER 2

GANYMEDE

2.1 Evidence of transpressional tectonics on the Uruk Sulcus region, Ganymede

The material of this section has been published in the Tectonophysics journal: Rossi, C., Cianfarra, P., Salvini, F., Mitri, G., Massé, M. (2018). Evidence of transpressional tectonics on the Uruk Sulcus region, Ganymede. Tectonophysics, 749, 72-87. https://doi.org/10.1016/j.tecto.2018.10.026

Abstract

The surface of Ganymede is characterized by intense tectonic deformation. The two terrains, light and dark, show morphotectonic features, namely, grooves and furrows. These represent kilometric systems at the regional scale, interpreted as extensional structures (e.g., horst and graben systems). Currently, evidence of significant compression has not yet been recognized, leaving open the opportunity to clarify the tectonic balance of Ganymede's surface. Debate still exists on the geodynamics responsible for surface deformation, and the investigation of these features contributes to understanding the internal processes. To understand the deformation that shapes the surface of the satellite, we explore the tectonic setting of the light terrain region of Uruk Sulcus. Using structural geology methodologies by remote sensing and systematic analysis of grooves, we recognize three groove systems within the sulcus and one furrow system in the neighboring dark terrain. Uruk Sulcus is also characterized by the presence of two domains of lineaments, subtle linear texture anisotropies related to the influence of tectonic processes on morphology. Comparison of the combined results from the analyses of the recognized groove systems with the lineament domains allowed us to infer the stress field responsible for their development in the studied area. According to these results, an evolutionary tectonic scenario for Uruk Sulcus is proposed: a tectonic corridor characterized by dextral transpression, with 58% of the internal compressional component approximately N-S oriented and responsible for localized, E-W extensional features among crustal blocks of the shear zone.

1. Introduction

Ganymede images of regional resolution obtained by the Voyager (1977) and Galileo (1989) missions show an icy surface globally subdivided into two region types, the dark terrain and the light terrain (Patterson et al., 2010), and deformed by landforms such as craters and linear structures. The linear structures correspond to kilometric, subparallel, linear to subcircular ridge and trough systems and are considered evidence of intense tectonic activity that deformed the lithosphere (Pappalardo et al., 1998; Prockter et al., 1998; Prockter et al., 2000; Patterson et al., 2010).

Despite some similarity, these structures are referred as furrows when they occur in the dark terrain, and the term grooves is limited to those structures that intensely etch the light terrain (Lucchitta, 1980; Bianchi et al., 1986; Murchie et al., 1990; Prockter et al., 1998; Prockter et al., 2000; Patterson et al., 2010; Hargitai and Kereszturi, 2015). The investigation of these features prompted an interest in understanding their origin and geologic relationships, as well as their relationship with the internal processes of Ganymede. Furrows and grooves were interpreted as extensional morphotectonic structures (e.g., horst and graben faulting style, McKinnon and Melosh, 1980; Pappalardo et al., 1998; Pappalardo et al., 2004; Pizzi et al., 2017). However, compressive tectonic evidence has not yet been identified; therefore, the existence of compressional deformation on Ganymede's surface is an open issue, as is the relationship between its internal dynamics and surface geology.

We investigate possible evidence of compression within a strike-slip corridor, proposing a novel geological model. This study focuses on the area centered on the light terrain of Uruk Sulcus, a NW-SE trending region (in the anti-Jovian northern hemisphere) where evidence of intense surface deformation has been imaged. Structural analysis of remote sensing images shows that the area is influenced by both extensional and contractional features within a regional transpressional framework.

2. Geological setting

Ganymede, with a radius of 2631.2 +/- 1.7 km (Anderson et al., 2001), is the largest moon in the Solar System. Its interior consists of an iron core several hundred kilometers in radius, covered by a silicate rocky mantle, and approximately 600 - 900 km of water and ice in the outer layer (Anderson et al., 1996; Deschamps and Sotin, 2001; Schubert et al., 2001; Sohl et al., 2002; Hussmann et al., 2007). This outer water layer is subdivided into ice-I at the top, which overlies a subsurface liquid water ocean, and high-pressure ice (ice-III, -V and -VI) at the bottom (Hussmann et al., 2007). The existence of a subsurface ocean is also demonstrated by the presence of a magnetic field induced by convection

within an internal conducting fluid layer rich in electrolytes such as salts and acids (Sarson et al., 1997; Kivelson et al., 2002; Schubert et al., 2004).

The water ocean layer may occur at approximately 150 km depth (Kivelson et al., 2002; Bland et al., 2009), below the outer ice-I shell. Ganymede also generates its own intrinsic magnetic field that is produced by convection in a viscous iron core (Schubert et al., 1996).

The satellite surface has landforms related to tectonic activity, suggesting the existence of interior processes that can deform the lithosphere (Watters and Schultz, 2010). The surface is divided into two terrain types, identified by differences in albedo, crater density and surface morphology, namely, the dark and light terrains (Shoemaker et al., 1982; Bianchi and Casacchia, 1986; Pappalardo et al., 2004; Patterson et al., 2010). The dark terrain occupies 35% of the surface and represents the older preserved surface of the satellite (Patterson et al., 2010). It is intensely cratered (Shoemaker et al., 1982) and structurally etched by furrows, structures whose origin has been broadly discussed in literature (e.g., McKinnon and Melosh, 1980; Squyres, 1980; Hartmann, 1980; Shoemaker et al., 1982; Casacchia and Strom, 1984; Hillgren and Melosh, 1989; Murchie et al., 1990; Schenk and McKinnon, 1991; Lucchitta et al., 1992; Schenk and Moore, 1995; Prockter et al., 2000; Jones et al., 2003). Furrows form concentric ring arcs, a few tens to thousands of kilometers long, in isolated sets that crosscut other furrow sets at high angles (Prockter et al., 2000). They have been interpreted as grabens generated by stress resulting from the collapse of large ancient impacts (McKinnon and Melosh, 1980). Although they are not recognized as endogenic tectonic features, their characteristics may indicate the nature of the crust in which they formed, which should be relatively thin (McKinnon and Melosh, 1980; Casacchia and Strom, 1984). Furrows are the oldest features recognized on Ganymede, having been systematically overprinted by all craters (Passey and Shoemaker, 1982). Patterson et al. (2010) subdivided this terrain into three units, i.e., cratered, lineated and undivided. In this work, we investigate the dark lineated terrain that is supposed to represent an intermediate stage between dark and light terrain units.

The light terrain constitutes the larger part of the satellite surface (65%), and it is younger than the dark terrain, as proved by the significant lower crater density (Schenk et al., 1991). It presents as wide globe-encircling swaths characterized by a relatively higher albedo (Patterson et al., 2010). The light terrain is strongly deformed by sets of grooves, observed both at the regional (groove length > 100 km and average spacing of 10 km) and the local scales (groove length between 50 and 100 km, and average spacing of 1 km) (Casacchia and Strom, 1984; Bianchi and Casacchia, 1986; Pappalardo and Greeley, 1995; Pappalardo et al., 1998; Prockter, 1998; Pappalardo et al., 2004; Patterson, et al. 2010). Grooves represent a significant component of light terrain tectonics. Thus, understanding their origin would aid in understanding deformation processes and the evolution of the satellite and its internal crustal processes. Various authors (Lucchitta, 1980; Golombek, 1982; Herrick and Stevenson, 1990; Pappalardo et al., 1998; Bland and Showman, 2007; Bland et al., 2009) recognized the grooves as evidence of extensional deformation on the surface of Ganymede. In particular, Pappalardo et al. (1998) inferred that the grooves within Uruk Sulcus appear to exhibit tilt-block normal faulting. These Authors interpreted the grooves to be the result of extensional tectonic processes, referred to as "necking instabilities" (Fink and Fletcher, 1981; Collins et al. 1998; Dombard and McKinnon 2001; Bland and Showman, 2007). Their model suggests that the morphotectonic features of Ganymede are similar to those of mid ocean ridges or rift valleys on Earth and are recognizable as normal faults that develop in response of extensional stress in a brittle/plastic lithosphere over a ductile substrate of warmer ice. In addition to extensional deformation, strike-slip motion is also observed to be a component of Ganymede tectonics (Pappalardo et al., 1998; Yin and Hansen, 2014; Seifert et al., 2015; Cameron et al., 2016). Evidence of strike-slip displacement, indicating local transtension, has been often identified within several fault zones, which are organized into en-echelon segments and sigmoidal blocks (Pappalardo et al., 1998). Patterson et al. (2010) subdivided this terrain into four units, i.e., grooved, subdued, irregular and undivided. We investigate the light, grooved terrain that

presents a surface dominated by structural grooves and represents most of the light terrain of Uruk Sulcus.

According to the literature, Ganymede's tectonic setting results from several factors, including tidal heating and past phases of global expansion (Showman et al., 1997; Bland et al., 2009), internal processes (Schubert et al., 2001) and cryovolcanism, to a lesser extent (Pappalardo et al., 2004). These scenarios do not identify evidence for contractional strain, which would be expected to balance extension assuming a constant surface area.

3. High-Resolution Mosaic Preparation

We prepared two co-registered mosaics by integrating images from multiple platforms that have different spatial resolutions (Voyager 1 and 2, Galileo missions) to perform the morphotectonic analysis of Ganymede. A total of 59 Narrow Angle Camera (NAC) images from the missions Voyager 1 and Voyager 2 (1977) were used to produce two new grayscale mosaics, which have different resolutions due to the variability of the original images in the different regions.

The lower-resolution mosaic was prepared at a nominal resolution of 1006 m/pixel and was derived from interpolating images with resolutions ranging from 2468.06 to 1006.5 m/pixel. It covers the surface from approximately lat 56°N to lat 48°S and from long 122°E to long 109°W (Fig. 1, lower right, in yellow color).

The higher-resolution mosaic was produced at a nominal resolution of 485.7 m/pixel and was obtained from interpolating images with resolutions ranging from 997.8 to 485.7 m/pixel. This implies that the pixel values were interpolated for regions where only lower-resolution images were available and allowed us to obtain the best suitable images for our morphotectonic study. The higher resolution mosaic covers a more limited area, between lat 43°N and lat 75°S and between long 122°E and long 115°W (Fig. 1, lower right, in dark yellow color).

The images were extracted from the Planetary Data System (PDS) (http://pdsimage.wr.usgs.gov/) on the basis of overall quality, best available input resolution, and availability of high angles of sight and

sun elevation. Precise geodetic adjustments and noise removal (e.g., null pixels or excessive variation in brightness among neighbor pixels) were performed for all images using the public-domain Integrated Software for Imagers and Spectrometers (ISIS), developed by the Astrogeology Program at the USGS and available at: https://isis.astrogeology.usgs.gov/. ISIS applications used in the present study include data processing tools for image geometry findings, map projection and mosaicking, mathematical and statistical operations, spatial filtering, radiometric calibration and photometric correction, and often have mission specific packages available (Gaddis et al., 1997). Following these procedures, we prepared the two NAC image mosaics at different resolutions.

We extracted Solid State Imaging (SSI) images of the study area taken during the Galileo mission from the PDS 60. These images are characterized by a higher spatial resolution than the NAC images (ranging from 291 meters/pixel to 41.73 meters/pixel). The SSI images were processed using specific ISIS procedures to remove noise. A final shift correction for each SSI image was required to geographically match the NAC mosaic produced. The final mosaic was prepared by combining the two co-registered NAC mosaics with the SSI images. The merging was performed by selecting pixels from the highest resolution image available in each location. The final mosaic is illustrated in Fig. 1. It covers an area of 28,000,350 km^2, and is centered at 6° 05’ 00.8” S, 164° 30’ 20” W.

The Uruk Sulcus study area is the NW-SE trending light terrain, which is approximately 400 km wide and 2500 km long and occurs in the northern sector of this mosaic. The Uruk Sulcus structure envelops slices of dark lineated terrain. The mosaic also includes part of the dark terrain of the Galileo Regio, located NE of Uruk Sulcus. To better understand the regional kinematics deforming Uruk Sulcus, furrows from nearby sectors were included in the study, wherever the higher-resolution mosaic was available.

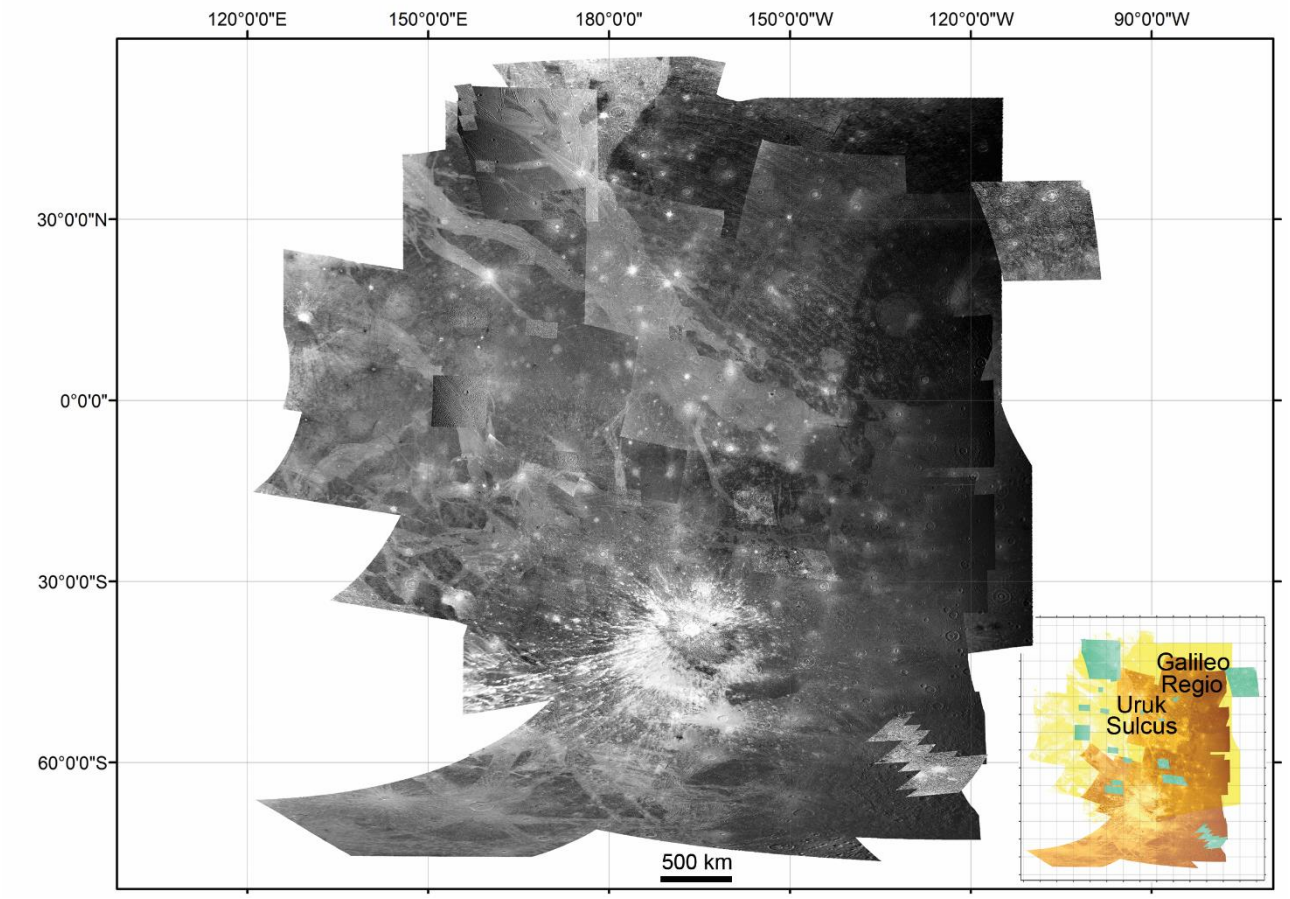

Fig. 1: High resolution mosaics of the anti-Jovian hemisphere of Ganymede. Voyager images with resolution ranging from 2468.06 to 1006.5 m/pixel and overlapping Galileo images (ranging from 291 meters/pixel to 41,73 m/pixel) were used. The northern part of the mosaic includes the study area: the NW-SE trending light terrain of Uruk Sulcus, which is approximately 400 km wide and 2500 km long. The NE sector of the mosaic includes the dark terrain of the Galileo Regio. In the lower right, the merge of the two mosaics is represented in false color yellow (lower resolution) and dark yellow (higher resolution) and the Galileo images are shown above the mosaic (light blue). The high-resolution version is available in the data repository.

4. Structural Analysis - Method

Grooves in Uruk Sulcus and furrows in the adjacent lineated dark terrain (Patterson et al., 2010) were identified (Fig. 2 shows examples of these structures). A total of 1679 elements were mapped on the mosaic (Fig. 3).

These structures were grouped into separate groove and furrow systems based on their characteristics and their spatial and crosscutting relationships (Fig. 4). Systems were identified by recognizing bands of grooves/furrows with similar appearance and orientation. This initial classification was then extended to the elements in the surroundings bands that had homogeneous characteristics. This process was propagated in a forest-fire model (Turcotte, 1997) until all elements were classified.

We quantitatively analyzed these elements in two ways.

- As multiple elements, where each structure was represented as a series of contiguous straight segments characterized by azimuth and length. Each structure is segmented to form a unique configuration.
- As single straight segments, where structures were characterized as simple elements by connecting the two vertices with the minimum length and azimuth needed.

Groove and furrow morphologies were quantitatively characterized by sinuosity, location, azimuth, length, and spacing and were stored in a GIS database (ArcGis software). All of the analyses were performed using DAISY3 software (Salvini, 2004; freely distributed at http://host.uniroma3.it/progetti/fralab).

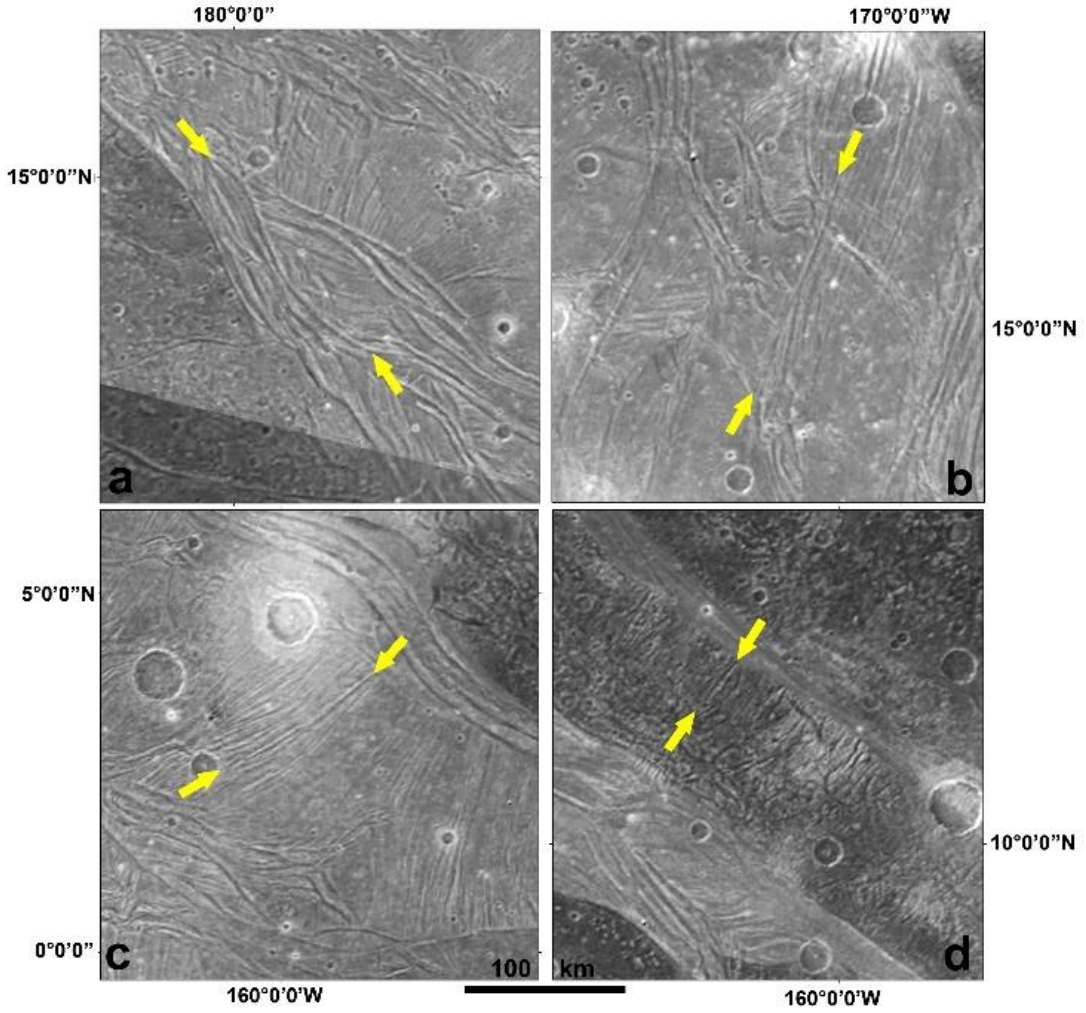

Fig. 2: Examples of grooves and furrows of the identified systems on the produced NAC mosaics. a) groove GUS1 – Identity number (ID) 4; b) groove GUS2 – ID 2; c) groove GUS3 – ID 154; d) furrow FUS – ID 88. The location of these areas is shown in Fig. 3.

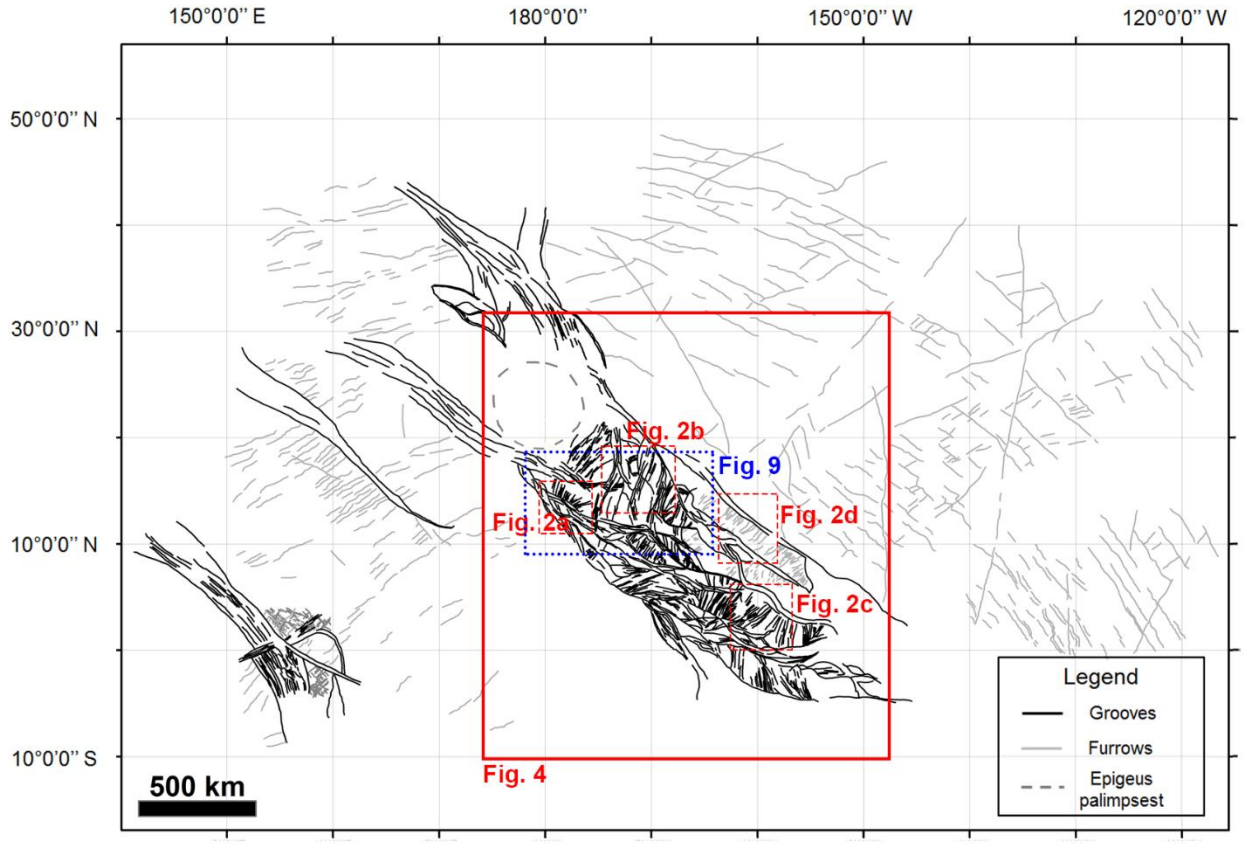

Fig. 3: Features detected in the light and dark terrain within the mosaics produced. The black lines are groove features and the gray lines are furrows. The circular dashed line delimits the Epigeus palimpsest in the northern part of Uruk Sulcus. The dashed red squares indicate the location of Fig. 2a-d; the red square indicates the location of the Uruk Sulcus region shown in Fig. 4; the dotted blue square is the location of Fig. 9.

4.1 Sinuosity

The sinuosity quantifies the variability in the azimuth of a given linear structure. This undulation may be ascribed to either their dependence on a kinematic process, in which case the undulation refers to the variability of the movements along the element, or to their deformation after formation. The latter case may indicate it could be used as a relative age indicator.

The sinuosity (Si) was defined as the ratio of the real structure length to the distance between its vertices. The variation in sinuosity is thus defined as the difference between the length of the multiple elements (l_m) and the single straight segments (l_s), according to the equation:

$$Si = \frac{l_m - l_s}{l_m} \quad (1)$$

In our application we approximated the average sinuosity value of each system using the equation:

$$Si_m = \frac{\sum l_m - \sum l_s}{\sum l_m} \quad (2)$$

4.2 Azimuth

For each system, azimuthal analysis was performed using frequency and cumulative length to characterize the orientations of multiple elements and single segments. In this way, a total of four analyses characterized each system (two analyses for the multiple elements and two for the single segments). The azimuthal analysis was performed by a polymodal procedure that includes a best fit with a family of Gaussian curves, which represent the independent azimuthal groups within each system (Wise et al., 1985; Maggi et al., 2015; Cianfarra and Salvini, 2016a). In this way, each Gaussian peak corresponds to a preferential orientation with its statistical parameter, namely, their modes, and corresponding mean azimuths and standard deviations. The standard deviation values (sd) obtained are representative of the variation within each system. The sd value may be related to the relative age of the systems. During deformation of the Ganymede lithosphere, it can be reasonably assumed that a ductile component occurs (more or less linearly) with time (e.g., Turcotte and Schubert, 2002). This assumption implies that the longer an area is deformed, the more it is deformed by the ductile component. The occurrence of this component will induce rotation/scattering of the linear elements formed by (early) brittle deformation processes (e.g., Riedel, 1929; Tchalenko, 1970). Therefore, it is inferred that brittle element groups, such as furrows and grooves families, will have relatively large sd, which indicates that the larger rotations and scattering are produced by the action of successive diffused and minor deformation. Conversely, younger systems are characterized by

relatively lower sd values. This condition can be quantified, in a polymodal distribution, with the computation of NorH/sd (Cianfarra and Salvini, 2014, 2015a; Lucianetti et al., 2017) for each azimuthal distribution (Gaussian curves) identified. The NorH/sd value represents the ratio between the relative height, or Normalized Height NorH, and the standard deviation, sd, of the Gaussian distribution that represents the corresponding population. A low NorH/sd, accordingly, indicates a relatively younger system. This ratio allows us to propose a relative chronological sequence among the systems identified. This process includes the Gaussian fitting of azimuthal distribution to its NorH/sd of elements calculated in the circular spot areas within the main zone of each system. These areas are circular within each system and selected so that the spatial rotation of the system is negligible with respect to its scattering (sd). In this way, we avoid biasing the analysis by adding the system regional rotations to the sd computation. In this study, the radius of each spot area was 140 km.

4.3 Length-Spacing ratio

To describe the spatial distribution texture of the systems, we introduce the Length/Spacing (L/S) parameter (derived from the Height/Spacing, H/S, in Salvini, 2013; Cianfarra and Salvini, 2016a). In structural geological analysis, the H/S parameter is the ratio between the height of a given fracture and its spacing from its neighbor. The term height is related to the term joint that is traditionally used to refer to extensional fractures in layered rocks. In this way, the height indicates the length of the fracture normal to the layering. In the H/S theory, the meaning of the term height includes the fracture dimension normal to the spacing, and thus the term height is maintained. This ratio represents a non-dimensional parameter that describes the fracture intensity at any scale as it is related to the applied stresses. This parameter can be used to quantitatively represent the expected fracturing history experienced by a rock and produced by tectonic stresses. Fracturing in rocks develops through time. Each new fracture forms by stress in between a pair of existing fractures, which halves the distance

between the new fracture and its adjacent fracture but doubles the total number of fractures. The mean value of the H/S ratio is linearly proportional to the amount of "work" associated with stress in brittle failure (Salvini, 2013).

In the case of icy shell of planetary bodies, the stresses on the lithosphere are produced by (relative) flow in the underlying liquid ocean through friction in the boundary surface, even if, compared to a rocky lithosphere, this coupling produces sensibly smaller stresses. In both cases the result is the deformation of the upper lithosphere layer, as the grooves and furrows in Ganymede.

The dimensions of the grooves and furrows were described by their lengths. This method was derived from the comparison with the lithosphere thickness, considered approximately 10 km (Golombek, 1982; Cameron et al., 2013), significantly smaller than the average length of the structures, at a ratio of approximately 1:5 (Tab. 1). This value implies that these structures involve the whole lithosphere. Their limited sinuosity (Tab. 1) suggests that these structures relate to sub-vertical tectonic features (i.e., fractures). Therefore, their length is proportional to the work associated with the tectonic activity occurring during their formation. A higher density of grooves/furrows is related to higher intensities of tectonic activity, either due to stronger stresses or a longer duration of stress application. This density is very difficult to quantify since it depends on the length range of the observed fracture and does not consider any fractures smaller than the image resolution, nor those larger than the image. The relationship between stress and deformation can be considered scale-independent (e.g. Turcotte and Schubert, 2002, pp. 80-94), and we collect data within a length range, which is an objective way to parametrize the fracture intensity and normalize values with the adimensional ratio Length/Spacing. In our application we used the length, L, of the structures and computed its ratio with the spacing, S. Spacing is defined as the distance between two straight lines that approximate two adjacent, nearly parallel structures from the same system. Fig. 5 shows examples of S measured in the various configurations.

We used the L/S parameter to characterize the relative stress/rheology properties of the Ganymede lithosphere in the regions where the systems are located at the time of their formation (Cianfarra and Salvini, 2016a). We computed the frequency of L/S values of the grooves/furrows, and we generated a frequency histogram to identify mean values for each system. We considered the stress-brittle deformation relationship scale-invariant (Turcotte, 1997) in the Ganymede lithosphere within the range of our observations. The comparison in the L/S adimensional parameters identified can represent differences in the state of brittle deformation of the lithosphere, including variation in its elastic thickness. Its variation can be inferred by considering that the stress on a material (i.e., a plate) depends also on its shape (i.e., thickness; Turcotte and Schubert, 2002). Therefore, a thinner lithosphere will behave in a more brittle manner, as well as undergo stronger solicitation. Therefore, we used the L/S parameter to indicate the amount of the brittle deformation experienced by the corresponding lithosphere and to infer lithospheric thickness variations. A more greatly deformed lithosphere, as measured by the L/S parameter, may result from a more brittle response of the lithosphere (i.e., thinner or lower brittle yield), a higher stress intensity, or a longer duration of stress activity.

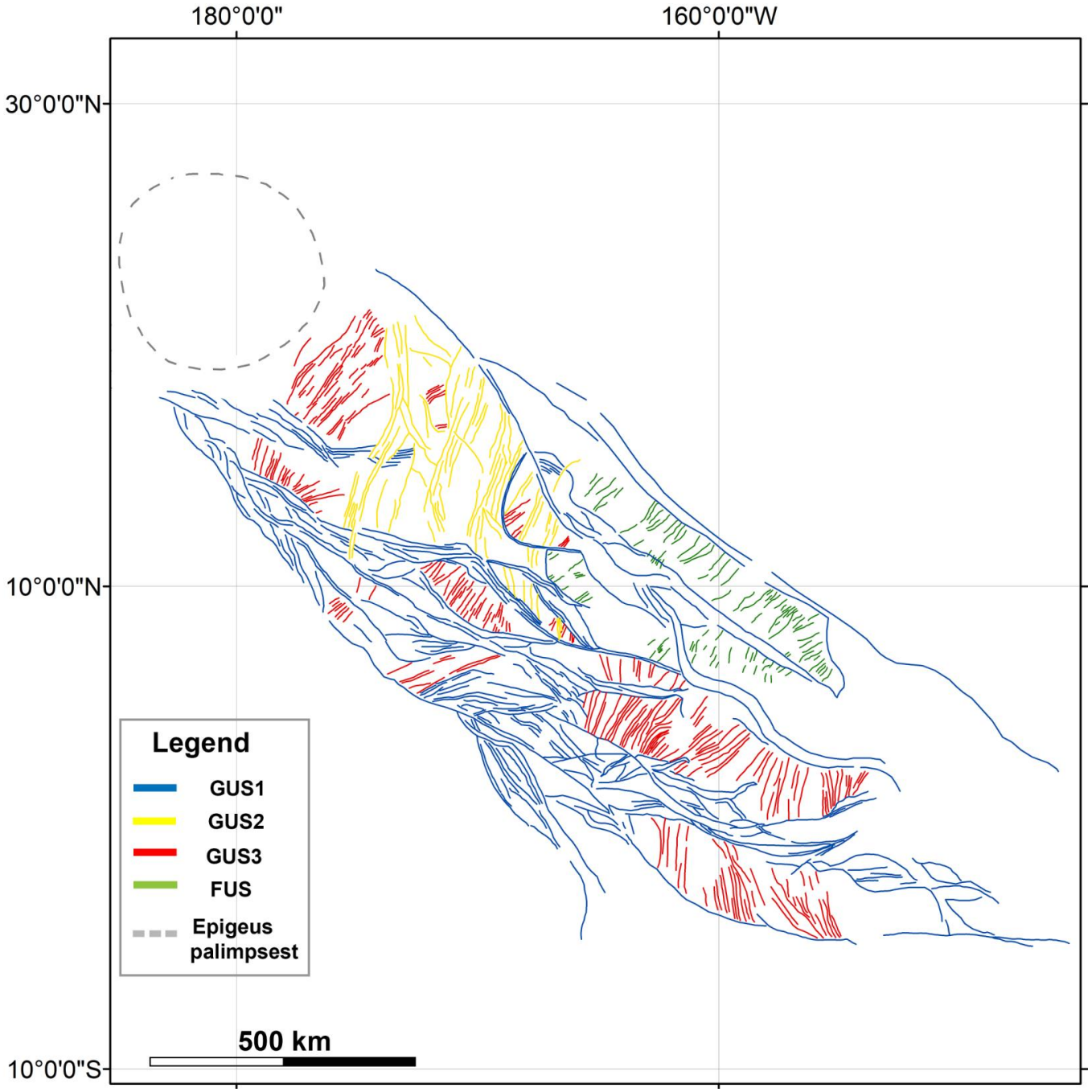

Fig. 4: Groove/furrow systems within the Uruk Sulcus area. Three groove systems were recognized. The NW-SE blue system that frames and dissects the sulcus is GUS1; the NNE-SSW trending yellow system, occurring in the NE part of the sulcus is GUS2; the NE-SW trending red system, occurring in localized sigmoidal areas, is GUS3. A NE-SW trending furrow system, FUS, borders the E edge of the sulcus and is represented by the green color. The location of this region is shown in Fig. 3.

Tab. 1: System parameters. N is the number of features composing the systems, Si_m is the mean feature sinuosity, NorH/sd is the ratio between the normalized height and the standard deviation of the Gaussian distribution of the main group analyzed in spot areas within each system, S is the Spacing, and mean L/S the average Length/Spacing value.

Systems	**GUS1**	**GUS2**	**GUS3**	**FUS**
N	306	104	276	190
Mean length (m)	93770	63730	45818	32025
Azimuth	N56°-58° W	N15°-17°E	N34°-37°E	N47°-55° E
NorH/sd	8.7	12.4	12.3	11.9
Si_m $(\Sigma lm-\Sigma ls) / \Sigma lm$	0.04	0.01	0.01	0.02
Mean L/S	12.1	8.9	62.5	6.2

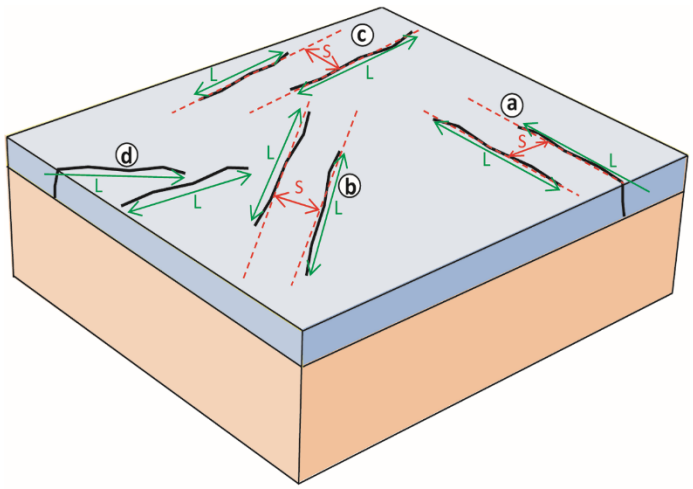

Fig. 5: Sketch illustrating the criteria used to measure the spacing S for the L/S parameter. Greysh color represent the Ganymede lithosphere overlying the mantle with pink color. Black lines indicate grooves/furrows. L is the linear length of elements (i.e., the distance between edges). Spacing was defined as the distance between two straight parallel lines approximating the groove/furrow. The sketch represents the various cases: a) spacing S measured between two nearly parallel elements; b) spacing S measured between two slightly parallel elements; c) spacing S measured between two partially offset, near parallel elements; d) no spacing is measured in this case, due to the excessive divergence between the two elements.

5. Structural analysis - Results

Our analysis allows us to group grooves and furrows into four main systems, named GUS1 (Grooves of Uruk Sulcus), GUS2, GUS3, and FUS (Furrows of Uruk Sulcus). In Table 1 are listed the parameters that characterize each system.

5.1 GUS1 - Main systems of Grooves of Uruk Sulcus

The main groove system, GUS1 (n=306; mean length= 93,770 km), frames the structure of the Uruk Sulcus (Fig. 4). It contains the longest grooves in the region (Fig. 2a), which range from tens to thousands of kilometers. This system develops along the sulcus boundaries and forms narrow bands that crosscut the sulcus. The longest GUS1 grooves delineate the well-defined NE and SW boundaries. At the southern side, the GUS1 grooves rotate to assume an approximately E-W orientation, following the sulcus boundary. Within the sulcus, GUS1 is characterized by the presence of bands of generally shorter grooves (length less than 100 km). The GUS1 grooves define the edges of the sulcus and eight main narrow bands trending approximately WNW-ESE that crosscut the sulcus (Fig. 6). These bands delimit zones that often form sigmoidal structures characterized by the grooves belonging to GUS3 and are arranged in a right-stepping, *en-echelon* geometry. Fig. 6 shows the bands' subdivisions and the sigmoidal areas where the GUS3 grooves are delimited. The bands a, g and h characterize the boundaries of the sulcus. The bands b, c, d and f delineate the sigmoids S1-6. The computed sinuosity factor for GUS1 is 0.04. This is the highest value among the systems and shows that grooves of this system are the most curved. The azimuthal analysis (Fig. 7a, e and Tab. 2) shows GUS1 trends approximately N56°-58° W, although this direction depends on whether a single segments or multiple elements are analyzed. The slight differences observed may be related to the asymmetry of the groove sinuosity. In the multiple element analysis, the sinuosity is responsible for the larger scattering (sd=19°-20°) compared to that of the single segment analysis (sd=9°-11°). The azimuthal analysis of the spot area of GUS1 gives a NorH/sd value of 8.7 (Table 1), which indicates

a large azimuthal scattering (sd) and suggests the presence of a relatively older generation of features. The spatial density of the GUS1 grooves, measured by the L/S analysis histogram, has a rather asymmetric distribution and a mean value of 12.1 (Fig. 8a).

5.2 GUS2 - Second system of Grooves of Uruk Sulcus

Grooves of GUS2 (n=104; mean length= 63,730 km, Fig. 2b) show a morphology similar to those of GUS1 (Fig. 4), although they present a lower sinuosity. Their NNE-SSW orientation is distinctly different from the orientation of the GUS1 grooves. The GUS2 system occurs in the NW side of the sulcus, centered at 14°51'N, 170°34'W (Fig. 4), and it is surrounded by the other systems. It develops along several bands up to 500 km long. To the east, it is delimited by the GUS1 grooves that form the NE boundary of the sulcus. To the south, the GUS2 grooves are truncated by the second band of GUS1. In this location, they terminate against the GUS1 grooves, except along their westernmost portion, where they crosscut the GUS1 grooves. To the west, the GUS2 grooves crosscut GUS1 and limit the GUS3 grooves along a well-defined, rather straight boundary. In the southeastern-most portion, a small part of GUS2 is surrounded by GUS1 bands. Contacts between the GUS1 and GUS2 grooves are always at a high angle (> 60°). The sinuosity factor computed for GUS2 is 0.014. This value is lower than that measured for GUS1. The azimuthal analysis of the grooves (Fig. 7b, f and Tab. 2) shows the main direction of GUS2 is approximately N15°-17°E, for both single segments and multiple elements. The single segments analyses show a secondary peak in the approximately NNW-SSE direction that corresponds to a slight rotation of the groove swarm in the central part of the GUS2 area. This relates to the branched structure of the GUS2 system. This is also indicated by the multiple element analysis by the larger standard deviations computed. The NorH/sd value of GUS2 is 12.4. This value may indicate that the GUS2 grooves are younger than those of GUS1. The L/S analysis histogram of the GUS2 grooves shows a relatively skewed distribution with a mean value of 8.9 (Fig. 8b). This suggests a brittle behavior similar to that inferred for the GUS1 area.

5.3 GUS3 - Third system of Grooves of Uruk Sulcus

Grooves of GUS3 (n=276; mean length= 45,818 km, Fig. 2c) are easily recognizable by their thin and straight morphology and are relatively close spaced. Their trend scatters around a NE-SW direction and they are confined into 6 main sigmoidal areas named S1-S6 within the sulcus (Fig. 6). Five of these grooves are E-W elongated and enveloped by the GUS1 groove bands. These five areas have different dimensions. The three northern ones (area ≈ 10000 km^2, S2-4) are smaller than the two southern ones (area ≈ 60000 km^2). The northernmost elongated zone terminates abruptly against the GUS2 groove zone, S5-6). The sixth area is located in the northernmost part of the sulcus and is delimited by the GUS2 grooves to the east and the GUS1 grooves to the south (S1). To the north, this area is delimited by the Epigeus palimpsest (Jones et al., 2003), which obliterates Uruk Sulcus structures due to its large dimensions. The computed sinuosity factor for GUS3 is 0.01. This is the lowest observed sinuosity value among the systems and indicates that the GUS3 grooves have a rather straight trace, which suggests the brittle response is stronger in the lithosphere where the systems occur. The azimuthal analysis of GUS3 (Fig. 7c, g and Tab. 2) shows its features mainly trend approximately N34°-37°E. The scattering calculated from the multiple elements analyses ranges between 12° and 13°, while the scattering calculated from the single segments analyses ranges between 15° and 8°. This scattering reflects the different azimuths of the grooves in the six areas, which contrast with the rather homogeneous strike they present in each area. This configuration may reflect the influence the shape and orientation of the sigmoidal areas has on their development. The NorH/sd of GUS3 shows a value of 12.3 that indicates a relative age similar to that of GUS2. The L/S analysis of GUS3 shows values significantly higher than those of the other systems (L/S mean value= 62.5, Fig. 8c).

These values indicate that the lithosphere where GUS3 occurs presents a more brittle response to deformation than that of the other systems. By assuming a similar lithosphere rheology and thickness

among the three systems, the presence of local, horizontal stress conditions is closer to the lithosphere strength within the sigmoidal areas and produced by their deformation during dislocation.

5.4 FUS - Furrow system of Uruk Sulcus

Zones of dark lineated terrain (Patterson et al., 2010) are adjacent and enveloped within the Uruk Sulcus in its eastern side (Fig. 2d). Furrows in these zones (n=109; mean length= 32,025 km) are characterized by a rather high density, which is different from the average value in the dark terrain. They occur in three areas enveloped by GUS1 grooves along the NE boundary of the sulcus. The most central area is centered at 160°30'W, 8°51'N, the outermost area is centered at 160°30'W, 6°11'N, and the southernmost area is centered at 158°11'W, 6°11'N (Fig. 4). The furrows have an average NE-SW trend and terminate nearly orthogonally against the GUS1 grooves. These furrows are characterized by a relatively thin appearance, associated with a poorly sinuous trajectory. These furrows are generally shorter than the grooves (mean furrow length is 32025 m, Tab. 1). The computed sinuosity factor for the FUS is 0.02. This value indicates that the furrows have a rather straight geometry that resembles the GUS3 grooves. The azimuthal analysis of FUS (Fig. 7d, h and Tab. 2) shows its elements are mainly oriented approximately N47°-55°E, similarly to those in GUS3. In N the multiple elements analysis, the directions are split into a main peak at N55°E and a secondary peak around N34°E. These two directions merge in the single segment analysis into a unique peak at N48°E. Their sd are relatively small, with values of approximately 6°-10°, which indicates a rather constant azimuth. The NorH/sd value for FUS is 11.9, similar to the values from the GUS2 and GUS3 systems, which suggests these systems have a similar age. The L/S analysis of FUS produces the lowest values in the Uruk Sulcus (L/S mean value= 6.2, Fig. 8d). This distribution of FUS suggests the dark terrain lithosphere has a more homogeneous brittle response than the light terrain lithosphere.

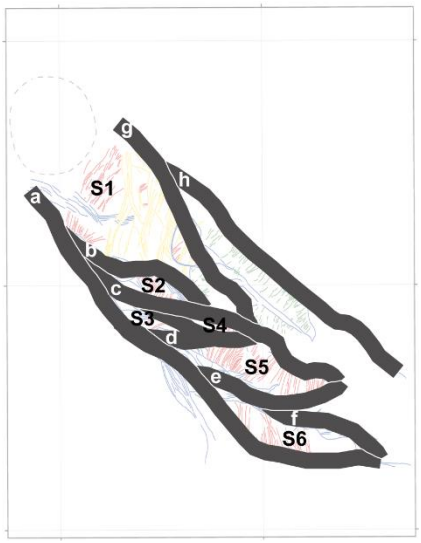

Fig. 6: Location of the GUS1 bands (a-h). Bands a, g and h represent the sulcus boundaries, and bands b-f delimit the sigmoidal area from S1 to S6.

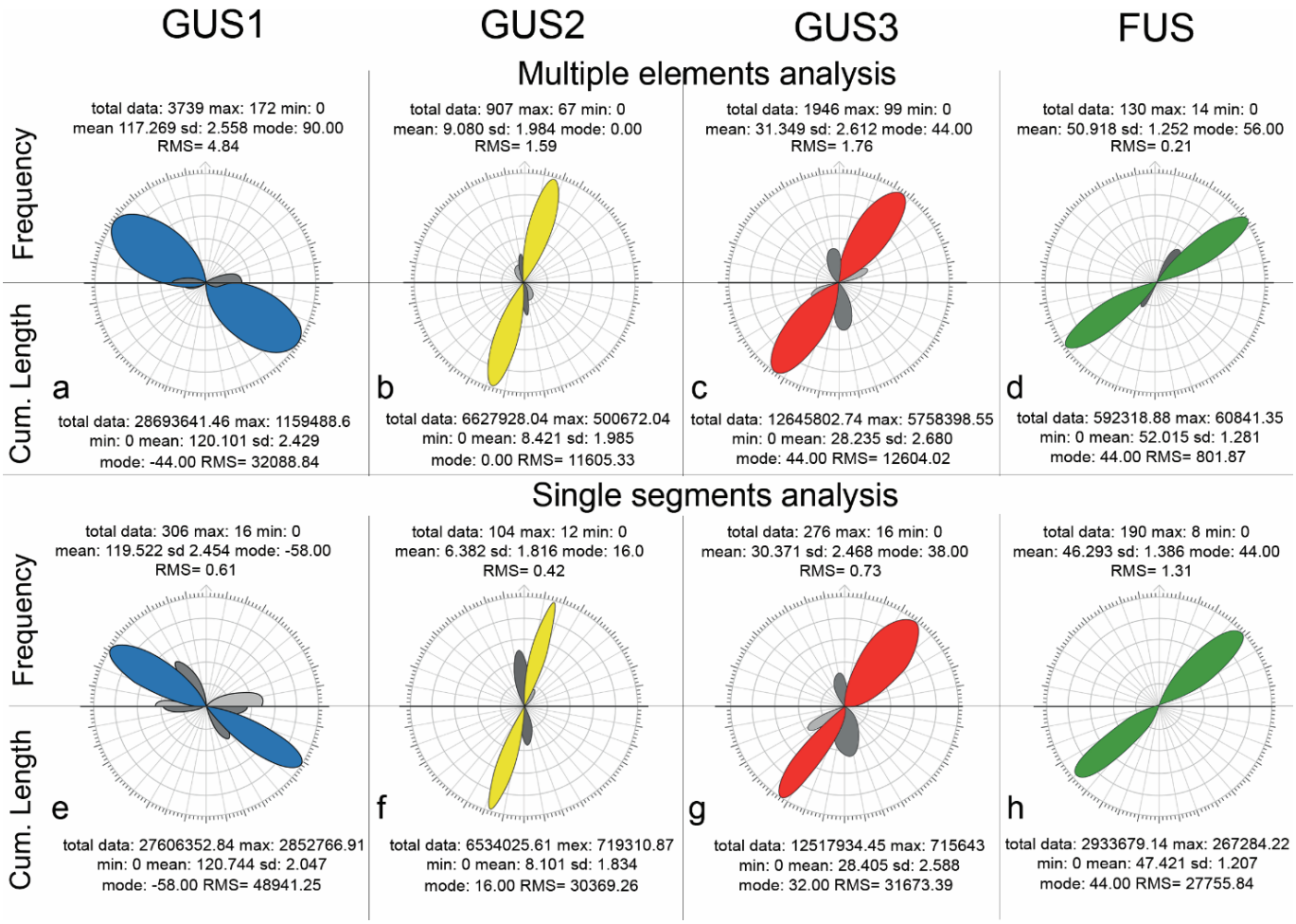

Fig. 7: Azimuthal analysis of the recognized groove/furrow systems represented as multiple elements of a) GUS1, b) GUS2, c) GUS3 and d) FUS and single segments of e) GUS1, f) GUS2, g) GUS3 and h) FUS. The wind-rose diagrams are subdivided into two semicircles, which show the analysis by frequency (the uppermost diagram) and the analysis by cumulative length (the lowermost diagram). Tab. 2 shows the Gaussian parameters of the azimuthal analyses.

Tab. 2: Tables of the Gaussian parameters of the azimuthal analysis. The number of Gaussian peaks (#), the percentage of occurrence (%), the Normalized height (NorH), the Maximum height (MaxH), the azimuth, and the standard deviation (sd) are reported.

Gaussian Parameters																								
Multiple elements													Single segments											
Systems	Frequency						Cum. Length						Frequency						Cum. Length					
GUS1	#	%	NorH	MaxH	Az	sd	#	%	NorH	MaxH	Az	sd	#	%	NorH	MaxH	Az	sd	#	%	NorH	MaxH	Az	sd
	1	100	100	121	-56.2°	20°	1	100	100	1024766	-56°	19.6°	1	100	100	12.6	-58°	11.7°	1	100	100	1573605	-57.9°	9°
	2	44.3	33	40	83.5°	13.7°	2	28	20.8	213395	83°	12.5°	2	64.8	45.8	5.7	-33.7°	11.4°	2	66	36	567090	-88.5°	10.7°
													3	74	49.8	6	83.9°	11.9°	3	55	33	524923	-34.8°	9.6°
GUS2	1	100	100	54.5	16.9°	8.6°	1	100	100	374353	17°	8.9°	1	100	100	7.8	15°	5°	1	100	100	596838	17°	5.8°
	2	27	26.5	14.5	-5.9°	5.6°	2	29	30	112464	-6.4°	5.7°	2	100	54.6	4	-5°	9°	2	91.8	36.5	218172	-5.6°	9°
	3	54.5	15.4	8.4	-21°	19.6°	3	56.5	17	65451	-20°	19°	3	36.9	20	1.5	27.6°	8°						
GUS3	1	100	100	90.4	34.7°	12.9°	1	100	100	533807	35°	13.7°	1	100	100	13	37°	15°	1	100	100	610296	36°	8°
	2	70	31	28	-9.7°	16°	2	85	42	226677	-8°	15.7°	2	58	33	4	-12°	12°	2	100	43.9	268031	-2°	18°
	3	33	29.7	26.8	67°	8°	3	24	27	144014	66.9°	7°							3	47	39.5	241411	60°	8°
FUS	1	100	100	10.7	55°	8.4°	1	100	100	48366	54.8°	9.5°	1	100	100	25.7	47.9°	10°	1	100	100	819360	48°	8.8°
	2	74	35	3.7	34.5°	8.5°	2	50	26	12759	31.5°	7.7°												

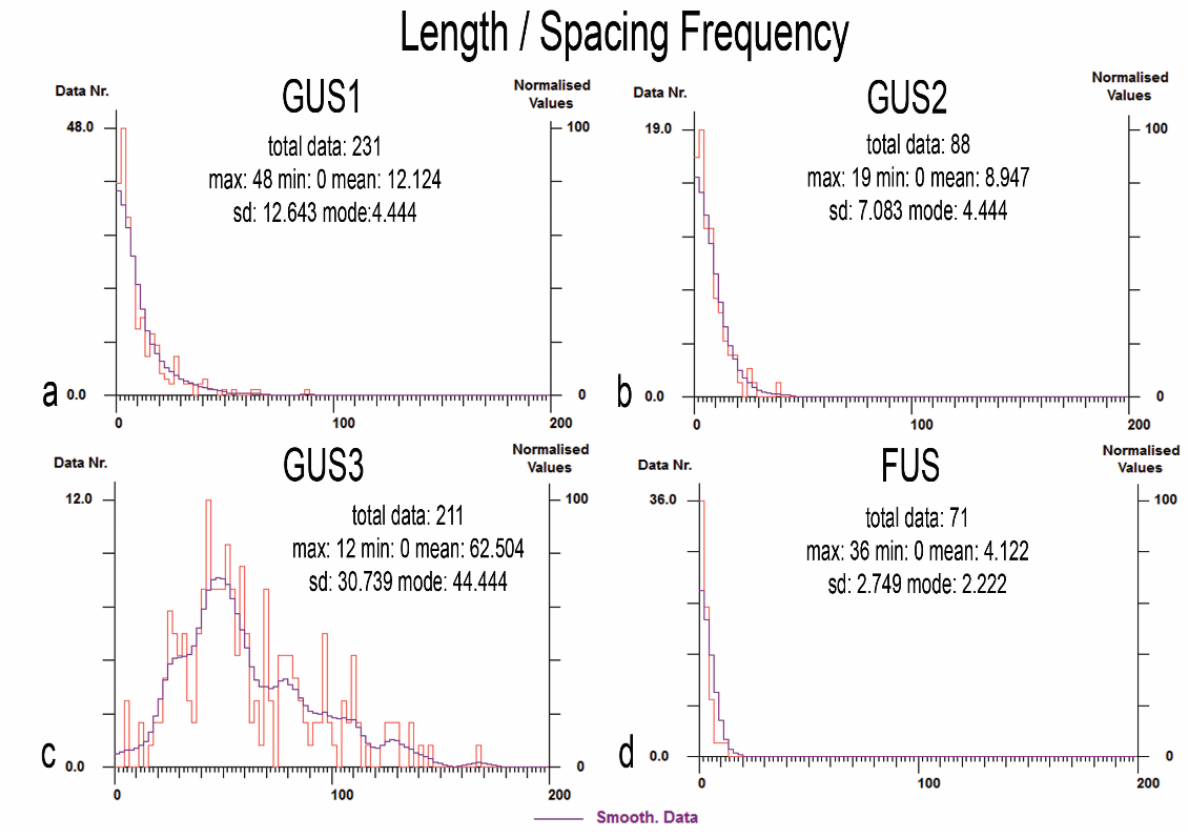

Fig. 8: Length/Spacing analyses of the groove systems a) GUS1, b) GUS2 and c) GUS3, and the furrow system d) FUS. Histogram of the L/S by frequency analysis in the data that range from 0-200 is shown. Purple curve represents the smoothed histogram (with an interval of 11.1) to ease the visualization of the frequency.

6. Lineament domain analysis

Planetary surfaces are characterized by the presence of linear topographic features. These are evident on available kilometric-resolution images and, despite the observation that they seldom correspond to known geologic elements, have been used to infer the geodynamic setting of tectonized regions.

Two detection methodologies are used for the identification of linear features in the images. The first is the visual observation of the images that have a high angle of sight. Linear feature identification is based more on their tonal contrast than on their straightness. This technique has been widely used in the studies of the Earth as well as of other bodies (e.g., Jordan and Schott, 2005; Masoud and Koike, 2011; Giordano et al., 2013; Gabrielsen and Braathen, 2014; Scheiber et al., 2015; Cremonese et al., 2016). The grooves and furrows were identified using this method.

The second technique identifies linear features by emphasizing their straightness. This necessitates visually inspecting the image with a low angle of sight to enhance this characteristic. Linear features belonging to this group are often faint and poorly visible, and special techniques have been suggested for their identification (Wise, 1982; Wise et al., 1985). Automatic techniques have been developed to identify these features and were applied in this work (Salvini, 1985).

These different methodologies allow the identification of two classes of linear features, with a partial overlap corresponding to tonal-contrasted and straight features. In this way some of the grooves/furrows belong to both classes. The two classes reflect different geological conditions. The former represents the effects of the tectonic activity on planetary surfaces and are referred to as lineaments. Lineaments of the latter class cluster around preferential orientations to form lineament domains that occupy well-defined spatial regions. These lineaments result from alignments of morphological features in the topography, whose shape is influenced by preferential erosion directions induced by upper crustal stresses/kinematic conditions. These do not correspond to a single morphology, but instead are the result of the presence of a series of well-aligned features that belong to different valleys and reliefs. This characteristic requires identification using the special technique described above.

The lineament class can be used to infer the stresses and kinematics of the planetary surfaces (Wise, 1982; Wise et al., 1985; Cianfarra and Salvini, 2014; Cianfarra and Salvini, 2016b; Lucianetti et al., 2017). The former class corresponds to the grooves and furrows in the present study.

In this way the identification of groove and furrow systems was integrated with the lineament domain analysis to elucidate the tectonic and geodynamic setting of the lithosphere of Uruk Sulcus. This comparison allowed us to characterize the geodynamic meaning of the recognized groove/furrow systems. Lineaments relate either to crustal stresses, dynamic lineaments, or to movements within shear zones, as evidenced by the kinematic lineaments along regional strike-slip faults (Cianfarra and Salvini, 2015). Both dynamic and kinematic lineament domains occur on planetary surfaces. In most

cases one domain largely prevails over the other, depending on the geodynamic setting. Regional kinematic zones, marked by the presence of (kinematic) lineament domains, often produce internal stress conditions in which a second, subordinate dynamic lineament domain develops. In these regions, kinematic lineaments are comparatively longer and more scattered than the dynamic lineaments. The latter are related to stress fields that are generally better iso-oriented than the kinematics pathways, which result from local (i.e., more variable) relative movement directions.

6.1 Method

Following Wise et al. (1985) and Cianfarra and Salvini (2015), we performed an automatic lineament domain analysis of the study area. We identified 2501 lineaments within the Uruk Sulcus central area, spanning 292 215 km^2, from latitude 18° 50' N to latitude 6° 40' N. The lineament domain azimuthal analysis was limited to the central area of Uruk Sulcus since it is a representative area for the comparison between groove/furrow systems and lineament domains. This selection avoids the bias introduced by spatial variation in the stress/kinematic directions along the sulcus. This rotation is evident in the groove/furrow system map in Fig. 4.

The lineament detection was performed on the NAC higher-resolution mosaic. A small portion of the investigated section is not covered by the higher-resolution mosaic, and for this section, the analysis was performed by integrating the lower-resolution mosaic. The mosaic image was subdivided into 45 partly overlapping subsets of 9500 km^2, corresponding to a ~220x220-pixel image. We carried out a lineament detection process on each subset. All identified lineaments were cumulated for the total data analysis to determine the regional tectonic setting. The lineament detection was performed using the SID software (in-house version 1.83) that allows to us identify lineaments as pixel alignments by a systematic search for all possible segments in a discrete image. Initial image processing was needed to enhance the presence of lineaments on the image and to remove image speckle (Salvini, 1985; Cianfarra and Salvini, 2015; Lucianetti et al., 2017). This processing includes image smoothing by a

3x3 kernel to reduce high frequency pixel DN scattering, followed by the use of directional edge half-filters (i.e., directional first derivative) that produce a set of images, according to N-S, NW-SE- W-E and NE-SW directions filtering (for the present study). Each image was then filtered by a Laplacian edge-enhancing filter, a threshold filter used to eliminate minor contrasts, and eventually, scattered and isolated pixels were removed by Life filtering (Cianfarra and Salvini, 2014, 2015). Eventually, lineaments detected in each image were cumulated to produce the final lineament domains of the image. The lineament identification by SID was performed by tuning the parameters that describe the geometric characteristics using a converging trial and error method. This process is iterated until a satisfactory result is achieved: the number of detected lineaments is statistically meaningful enough to perform a polymodal Gaussian fit, the azimuthal trends are clearly evident, the results are robust, i.e., results are persistent with slight variations in SID parameters. The minimum length of the detectable lineaments was 16,975 m, which corresponds to 35 pixels in the mosaic image. The maximum length was 48,500 m and corresponds to 100 pixels in the image. SID was set to identify a lineament if the corresponding portion of the image contained a density of pixels above a given threshold value (a minimum of 2 pixels within a running interval of 3 pixels). Interruptions in this density were allowed up to a maximum of 1 pixel. Each single sequence of meaningful pixel density was at least 5 pixels long. Lineaments were detected by a dynamic pattern recognition process consisting of the identification of specific portions of the image that have pixel patterns corresponding to the specified parameters. The search was conducted for all possible azimuths, with a resolution comparable to the orientations possible for the dimension of the given image and for a position with the resolution of the single pixel.

6.2 Result and interpretation

A total of 2501 lineaments with an average length of 49.45 km were automatically identified within the investigated area (Fig. 9a).

Following the methodology used for the groove/furrow systems analysis, the azimuthal analysis of the total lineament data was performed by frequency and by cumulative length and the results are illustrated in Fig. 9b. Both analyses provided very similar results and show the presence of two lineament domains with different scattering. The main domain has preferential orientations approximately N57.6°-56.2°W (by frequency and by cumulative length, respectively), and represents the NW-SE domain. The other domain is the NNE-SSW domain with mean azimuths of N19.7°-21.1°E. The two domains differ in their scattering: the NW-SE domain has standard deviations of 27.6° and 24.4°, while the NNE-SSW domain has a lower scattering, as shown by its standard deviations of 15.0° for both analyses. The two domains slightly differ also in the length of their lineaments (Fig. 9b). The difference in standard deviations allows us to identify the kinematic versus dynamic origin of the NW-SE and NNE-SSW lineament domains, and to frame them into a lithospheric geodynamic model (sketches in Fig. 10, following Cianfarra and Salvini 2014). The model of Cianfarra and Salvini (2014) describes, over the various transtension/transpression conditions within a shear zone, the angle between the kinematic movement (e.g., a strike-slip fault) and the internal brittle/failure regime (e.g., Riedel; 1929; Tchalenko and Ambraseys, 1970; Fossen, 2010; Cianfarra and Salvini, 2016b). This is illustrated by the associated extensional fractures. This angle is measured clockwise from the shear zones' boundaries to the internal fractures and varies from 0° in purely extensional regimes (Fig. 10a), to angles smaller than 45° in transtensional regimes (Fig. 10b), to 45° in purely strike-slip regimes (Fig. 10c), to angles larger than 45° in transpressional regimes (Fig. 10d), to 90° in purely compressional regimes (Fig. 10e). According to this model, the NW-SE domain represents the kinematic path along the Uruk Sulcus and reveals its parallel strike-slip component. On the other hand, the NNE-SSW orientation is parallel to the stress within the Uruk

Sulcus corridor. The internal angle measured of 77° indicates a right lateral transpression with 58% of the compressional component (Fig. 10; Rossetti et al., 2000; Cianfarra and Salvini, 2015). The large scattering of this domain reflects the kinematic conditions within the sulcus. The NNE-SSW domain is related to the dynamic setting within the sulcus and indicates horizontal maximum compression parallel to the lineament domain, i.e., NNE-SSW, with the maximum horizontal extension occurring in the WNW-ESE direction. This stress is located within the sulcus and it forms an angle between the maximum horizontal stress and the kinematic path at approximately 77.3°, i.e., the angle between the two lineament domains. The angle between the shear corridor boundaries and the internal fracture direction is related to the internal extensional/compressional stress component induced by the relative kinematics of the shear zone blocks (e.g., Cianfarra and Salvini, 2014; 2015; 2016b). This explains why the relative position of the internal stress orientation within the shear zone is representative of the sense of movement of the strike-slip component. The relative sense is computed as the relative movement of the block containing the inner lineaments from the sector of the obtuse angle towards the sector of the acute angle (Fig. 10; Cianfarra and Salvini, 2014).

Uruk Sulcus hence represents a strike-slip corridor characterized by right-lateral transpressional movement.

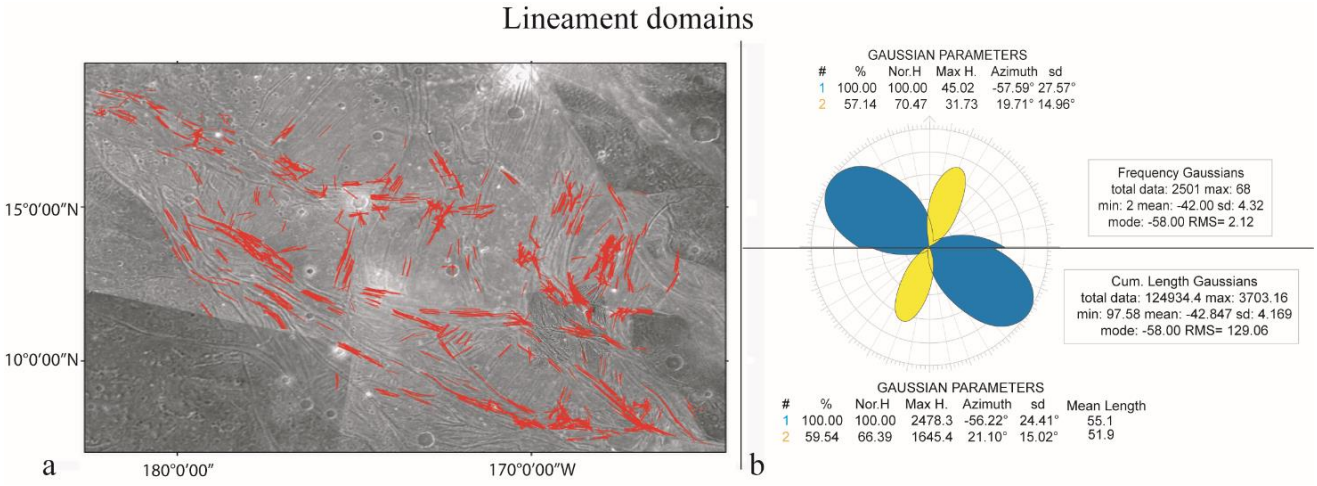

Fig. 9: Lineament domains detection (see text for details on the applied methodology). a) Lineaments automatically identified (red color) within the central area of Uruk Sulcus (total data: 2501 lineaments). The location of this analysis is shown in Fig. 3. b) Azimuthal analysis subdivided into two semicircles showing the analysis by frequency (upper) and the analysis by cumulative length (lower).

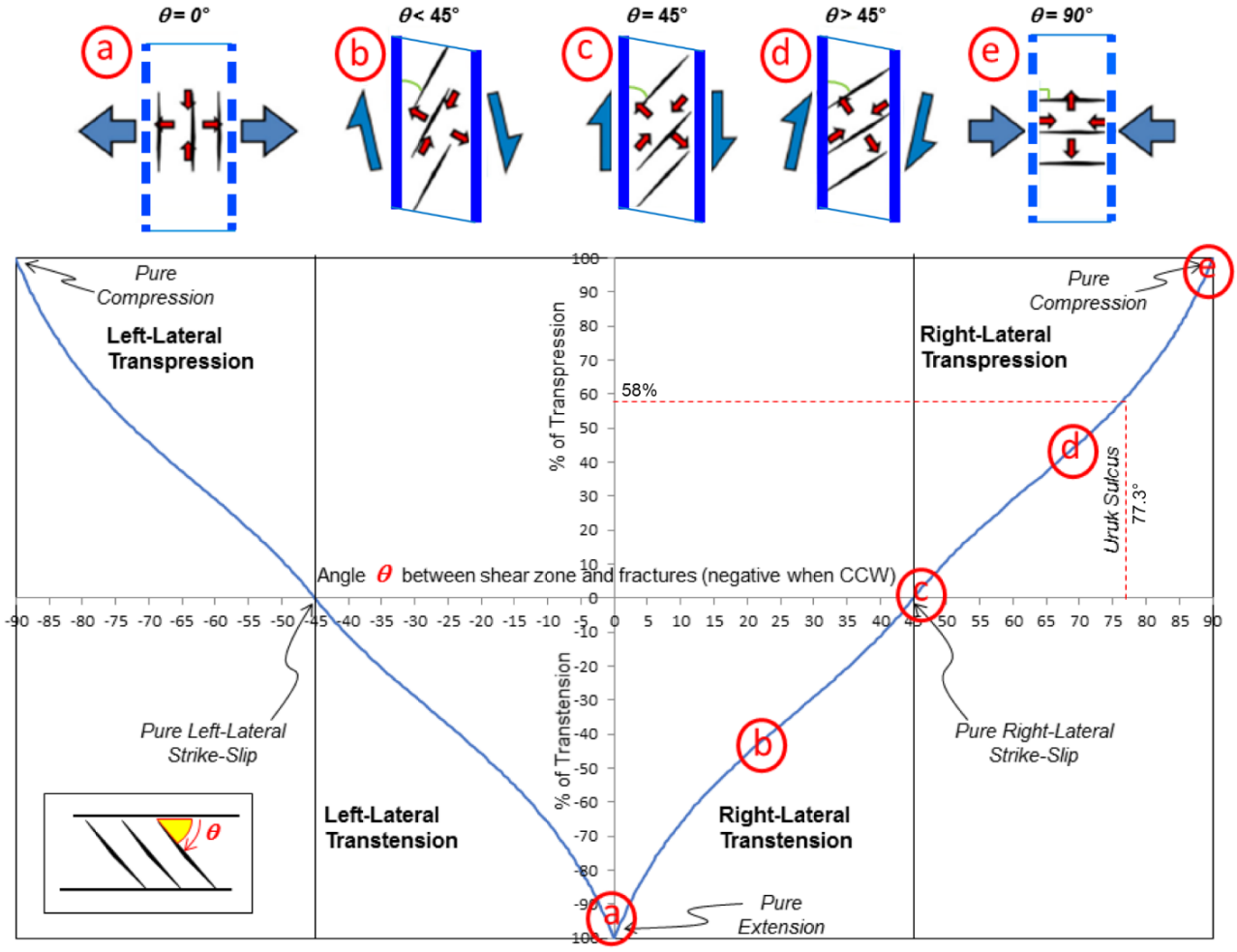

Fig. 10: Strike-slip conditions according to the clockwise angle between the shear zone and the internal fractures. The upper part of the figure (modified from Cianfarra and Salvini, 2014) shows the schema of the variation in the internal fracture angle θ within a shear zone according to the stress component (arrows): a) extension (θ = 0°), b) transtension (θ < 45°), c) strike-slip (θ = 45°), d) transpression (θ > 45°), e) compression (θ = 90°). a) and e) show dynamic conditions represented by the dashed boundaries (in blue color) and the internal fractures (in black color) that both constitute dynamic elements; b), c) and d) show tectonic conditions in which kinematic elements are represented by the boundaries and the dynamic elements by the internal fractures. The lower part of the figure shows different angles produced by different stress fields. These are shown in the diagram, where the x-axis shows the variation in the internal angle, and the y-axis shows the percentage of the extensional/compressional component. The angle changes with the variation in the internal stress field. A pure strike-slip framework forms internal fractures with an angle of 45° to the shear zone. If a compressional component is added to a strike-slip corridor (transpression), this internal angle increases, until pure compression occurs. On the other hand, when an extensional component is present (transtension), this angle decreases, until a pure extensional setting occurs. According to the sign of the measured angle, it is possible to know the sense of movement of the strike-slip corridor. When negative, the strike-slip sense is left-lateral. When positive, it is right-lateral. The angle found within Uruk Sulcus of 77° indicates a right-lateral transpression with a compressional component of 58%.

7. Discussion

Grooves and furrows represent the brittle deformation that characterizes Ganymede's surface. Their mapping and analysis allowed the identification of three groove systems in Uruk Sulcus, called GUS1, GUS2 and GUS3 and one furrow system, FUS in the dark lineated terrain involved in the sulcus tectonics (Fig. 4). The geometry of the systems compared with that of the lineament domains shows that the Uruk Sulcus is a strike-slip corridor that localizes the identified systems, which are produced by kinematic and internal stress conditions. The sulcus developed from a NW-SE, right-lateral transpression with a significant internal compressional component of 58% (Fig. 10) and a maximum horizontal (compressional) direction around NNE-SSW (Fig. 9b). The principal system, GUS1, delineates the sulcus (Fig. 4) and occurs in the internal sinuous bands that identify sigmoidal structures (Fig. 6; Ramsay, 1980; Van der Pluijm and Marshak, 1997). These are arranged in an *en-echelon* geometry, with right-step horizontal duplexing generated by the transpressional component (Fig. 4). The GUS1 bands rotate parallel to the corridor edges as they approach them to form the sigmoidal geometry described. This indicates that these bands have the same right-lateral sense of movement as the corridor. The development of these transpressional structures could be compared with the pressure-solution seams in S/C rock fabric (e.g., Fossen, 2010), where possible melting/sublimation could have occurred during the compression related to the strike-slip kinematics. GUS1 represents the morphological expression of the NW-SE kinematics along the sulcus and its tectonic origin is highlighted by the corresponding main lineament domain. The kinematic arrangement described is produced by the right-lateral sense of shear along the sulcus by the transpressional component. This arrangement is further supported by the presence of GUS2, which represents the morphotectonic effect of the internal stress condition and is delineated by the NNE-SSW stress-related lineament domain. GUS2 grooves represent extensional structures parallel to the maximum horizontal stress with extension occurring in a WNW-ESE direction. The angle between GUS1 and GUS2, which corresponds to the angular relationship between the lineament domains,

further demonstrates the transpressional right-lateral sense of movement. Internal to the sigmoidal structures, GUS3 has a similar angle as GUS1 and GUS2, which indicates it has a similar transpressional component. GUS3 represents the extensional morphotectonic expression of local surface stress conditions and indicates WNW-ESE extension and NNE-SSW main horizontal compression within the sigmoidal structures.

It is possible to associate a variation in the lithospheric behavior, either related to thickness, stress intensity, or duration, with the L/S values of the systems as reported in Tab. 1. The mean L/S value of 62.5 for GUS3 is significantly higher than those of the other systems. This value indicates that the lithosphere where GUS3 is localized, internal to the sigmoidal structures, might have been subjected to a thinning process related to the extension produced by significant stretching of the sigmoids. Alternatively, this value might indicate a higher deformation rate within the sigmoidal structures that would have induced a more brittle response, resulting in higher L/S values. The relative decrease in the mean L/S values among GUS1, GUS2 and FUS, respectively, might reflect a minor stress/deformation accumulation in their corresponding sectors. The combination of these two effects may well explain the values found. We assume that the duration of the tectonic event is the same within the sulcus region.

The present-day spatial distribution of the groove systems recognized frames the proposed interpretation well. The GUS2 and GUS3 grooves are extensional features that developed normal to the maximum extensional horizontal stress component, also locally described by Pappalardo et al. (1998). In comparison with the results described by other authors, the GUS2 could be associated with the structures induced by extensional necking instability of the lithosphere (Fink and Fletcher, 1981; Collins et al. 1998; Dombard and McKinnon 2001; Bland and Showman, 2007), and GUS3 might represent the more brittle regions (as also demonstrated by the L/S analysis) where second generations of normal faults occur. On the other hand, the GUS1 grooves are mostly compressional features that are not involved in the extensional regime of the necking instability model (Collins et al., 1998). The

NE sector of the corridor (Fig. 4) shows the effects of the NNE compression and WSW extension, produced by the right-lateral transpression along the corridor (GUS2). These effects are obliterated in the central and SE sectors by the development of the sigmoidal structures that are characterized by a self-similar transpressional right-lateral geometry and the development of internal structures (GUS3) produced by the NE compression and NW extension. The relative movement among the sigmoidal structures relates to the right-lateral shear along the corridor and is responsible for their horizontal duplexing in the SE sector. For this reason, the FUS furrows, present in the NE-central sector of the corridor, might have an analogous interpretation to the GUS2 and GUS3 extensional grooves and prove the transpressional character of the NE edge of the corridor. On the other hand, a transtensional scenario would have produced different groove/furrow orientations with respect to the corridor. Fig. 11 summarizes the expected scenarios within a corridor in the various strike-slip environments and was prepared by combining the kinematic and dynamic deformations that are expected to develop. Fig. 11a describes the scenario for a right-lateral transpression and fits the present geometry of the Uruk Sulcus well. Fig. 11b shows the framework that develops within a right-lateral transtensional corridor, which exhibits the development of internal block rotation and the formation of extensional features within the blocks, which form a small angle with the corridor. Fig. 11c illustrates the case for a pure right-lateral shear zone, which exhibits the internal development of extensional features with an angle of 45° to the corridor. Fig. 11d-f represent the symmetrical configurations for left-lateral environments.

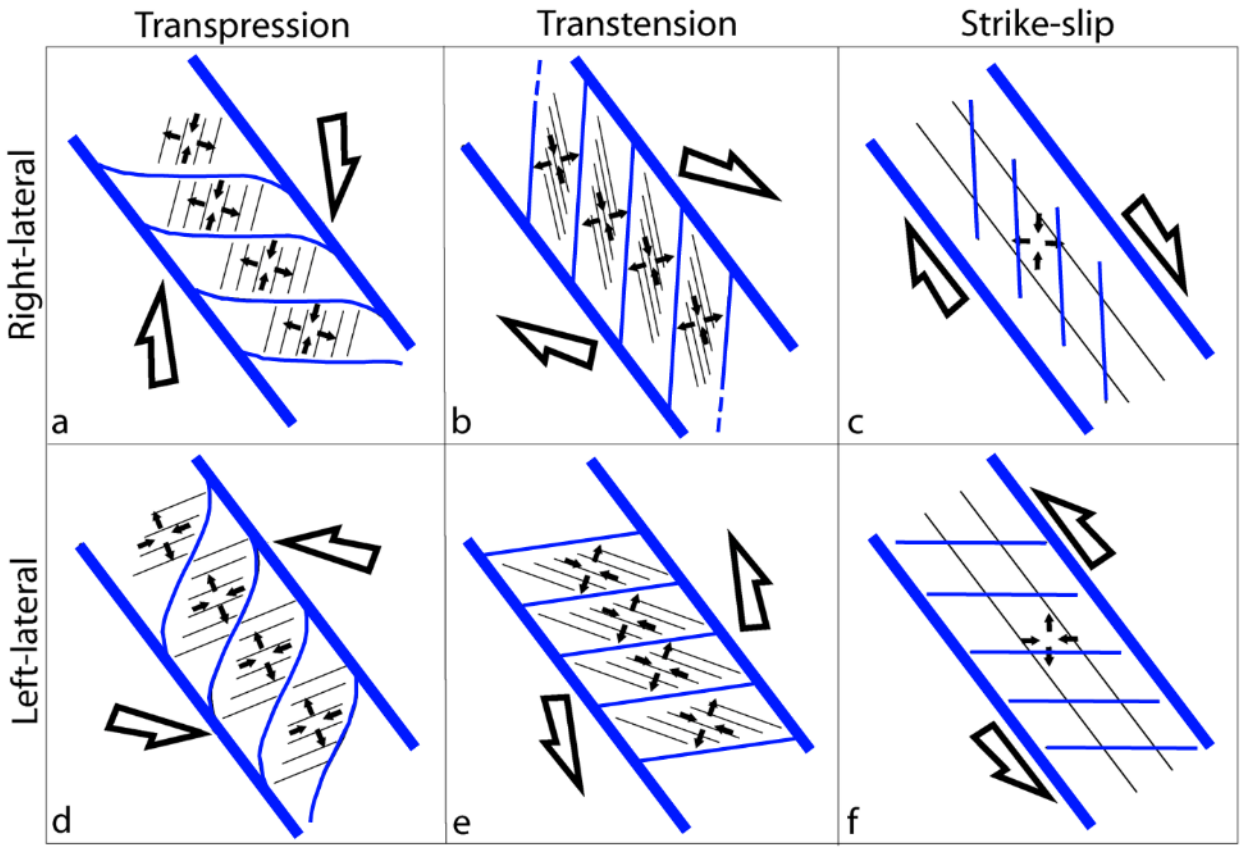

Fig. 11: Possible scenarios for different strike-slip environments that develop in a NW-SE corridor and its related internal structures. The black lines represent the dynamic conditions and the blue lines represent the kinematic conditions. The first row shows a right-lateral setting (a, b, c), and the second row shows a left-lateral setting (d, e, f). The arrows represent the stress fields associated with the strike-slip movement: a) Right-lateral transpression develops circa E-W sigmoidal structures with dextral movement and the internal extension develops NE-SW structures; b) Right-lateral transtension develops approximately NNE-SSW directed principal structures with sinistral movement and the internal extension develops NW-SE secondary structures; c) Pure right-lateral strike-slip with the associated internal stress field; d) Left-lateral transpression develops circa N-S sigmoidal structures with sinistral movement and the internal NW-SE extension develops NE-SW structures; e) Left-lateral transtension develops WSW-ENE principal structures with dextral movement and the internal stress field develops NW-SE structures; f) Pure left-lateral strike-slip with the associated internal stress field. Model a, right-lateral transpression, well represents the Uruk Sulcus internal setting inferred (derived from Harding, 1974).

The different geometries of the sigmoidal structures from NW to SE possibly replicates their spatial-temporal development (Fig. 12). Following the initial emplacement of the corridor with the development of GUS1 along its edges (Fig. 12b) and the corresponding development of GUS2 related to the induced stress condition (NW sector, Fig. 12c), the persistence of the right-lateral shear caused the sulcus structure to evolve by creating internal shear bands (GUS1). These isolated sigmoidal structures move relative to one another and duplex within the corridor (central sector, Fig. 12d). These

movements further increase the internal stress conditions and lead to the development of GUS3, similar to the early stage development of GUS2, and possibly obliterate the preexisting GUS2 grooves (central-SE sector, Fig. 12e). The persistence of these relative movements brings about the complete duplexing of the sigmoidal structures (SE sector, Fig. 12e-f).

The presence of the FUS furrows in the central-NE sector of the corridor may represent an incipient widening of the shear zone, involving nearby sectors of portions of dark terrain. These sectors seem lighter than dark terrain regions in Galileo Regio (Fig. 2d) and are characterized by FUS orientation and L/S values (L/S= 6.2, Tab. 1) comparable with those of GUS1 and GUS2. In these dark terrain areas, FUS furrows occur at a density higher than those of Galileo Regio (Fig. 3). This may represent the effect of the transpressional stress condition that developed or reactivated FUS following the involvement of the dark terrain within the corridor. In this way, the higher density of furrows in FUS indicates a possible reactivation, more recent than that which created the other furrows of Galileo Regio. Since the dark terrain portions were included in the corridor, the transpressional kinematics induced conditions of internal stress similar to those developed within the sigmoidal structures (GUS3) and FUS develops or reactivates normal to the NW-SE extension. This might represent a rejuvenation of these older dark terrain areas towards their possible future transformation into light terrain as proposed by Patterson et al. (2010).

This evolutionary model suggests an early development of the GUS1 system compared to the GUS2 and GUS3 systems. This is demonstrated by the higher values of NorH/sd calculated for the GUS2 and GUS3 systems (12.4 and 12.3 respectively, Tab. 1) relative to the GUS1 system (8.7, Tab. 1). The observed progressive decrease in the mean L/S value from GUS1 to GUS2 and FUS reflects the different exposure time of their corresponding sectors to the tectonic evolution of the corridor and fit the temporal sequence of the model well.

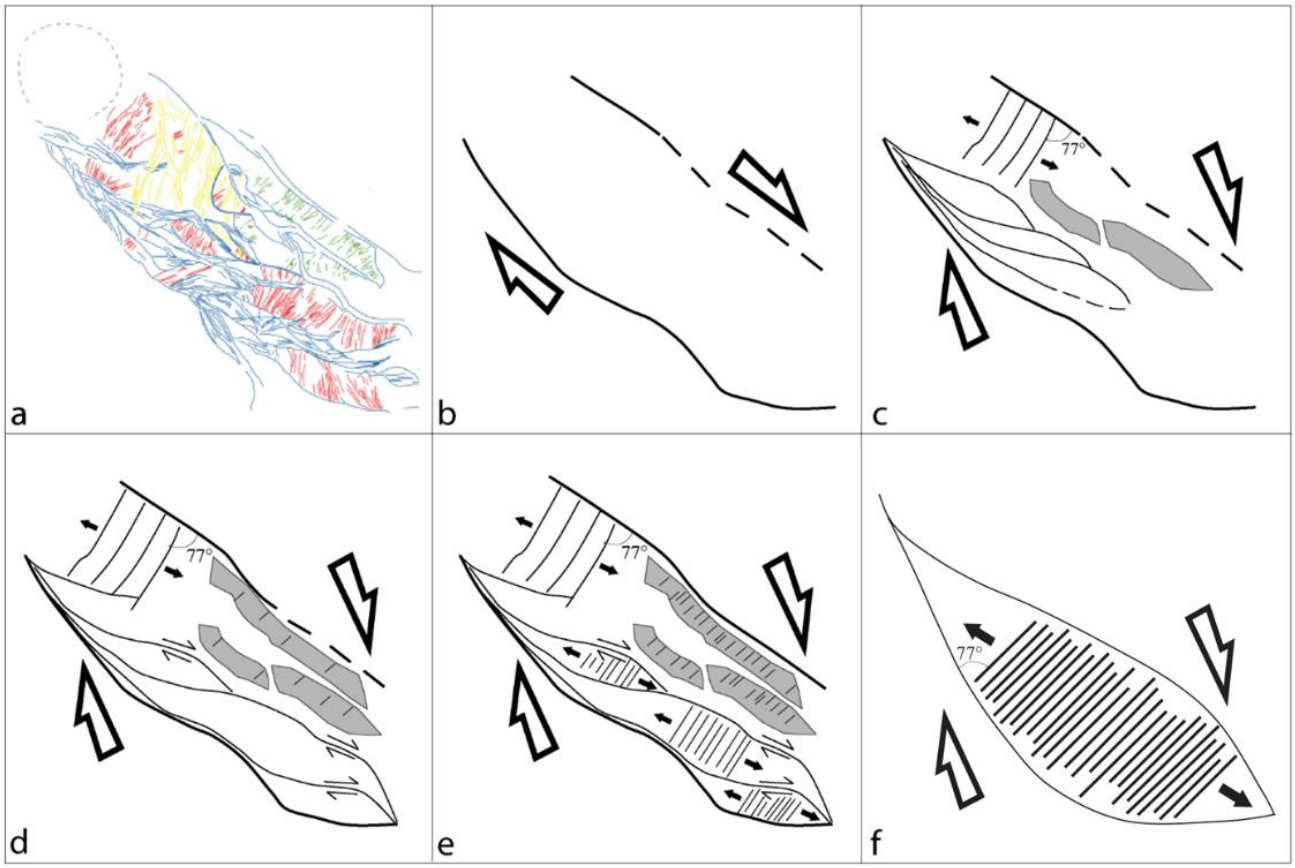

Fig. 12: Evolutionary tectonic model of Uruk Sulcus region. a) Present day configuration; b) Initial right-lateral strike-slip originating at the corridor edges (GUS1); c) Right-lateral transpression development associated with NE-SW extensional structures (GUS2) at high angles with the corridor edges (77°) testifying to the presence of a compressional component; development of the internal sigmoidal structures (GUS1) with dextral *en-echelon* geometry and inclusion of dark terrain portions within the corridor; d) Shifting and duplexing of the sigmoidal structures (GUS1) with dextral movement and continuous inclusion of dark terrain and formation/reactivation of furrows (FUS); e) Development of the NE-SW system (GUS3) self-similar to GUS2 and related to an extensional stress field within the compressed/stretched sigmoidal structures; density increase in furrows (FUS) within the dark terrain involved in the sulcus; f) Detail of the extensional-related grooves (GUS3) generated by the dynamics within a sigmoid.

8. Conclusions

Ganymede grooves/furrows represent important evidence of tectonic processes that shape the surface of the satellite. The combination of their analysis with the study of the lineament domains allows us to propose an evolutionary tectonic model of the Uruk Sulcus, and reveals its right-lateral transpressional framework that is derived from both kinematic compression and internal dynamic extension. This tectonic activity generates the main groove system GUS1 that forms the boundary of the shear zone and produces duplexed sigmoidal structures. Within the corridor, ~ E-W extension produces two groove systems, GUS2, in a localized area of the corridor, and GUS3 in the sigmoidal structures confined by GUS1. Their high angular relationship (77°) with GUS1 implies a compressional component of 58% within the strike-slip corridor.

Our results suggest that the transpressional kinematics involves portions of dark terrain where the FUS furrow system contains a higher density of furrows than that of Galileo Regio. This system results from the reactivation of older furrows and indicates a possible rejuvenation of the dark terrain portions associated with the corridor tectonics.

The L/S analysis proved to be an effective tool to study brittle behavior, including thickness variations, of planetary lithospheres even when characterized by underlying liquid ocean. The variation in lithospheric behavior, shown by the L/S values of the systems in the Uruk Sulcus region (Tab. 1), may suggest that the GUS3 area lithosphere is thinner, when similar tectonic conditions occur, and/or more deformed than that of the other systems.

The Uruk Sulcus represents the proper site to explore the time/spatial relationships between dark and light terrains. A systematic analysis of the sulci of Ganymede might validate this hypothesis and will be improved by imaging from future missions, such as the Jupiter Icy Moons Explorer (ESA) mission and the Europa Clipper (NASA). These missions, with their high resolution and radar images, will provide surface and 3D subsurface data pertaining to the grooves and furrows of Ganymede, as well as to features on other icy satellites.

Ganymede's surface shows several shear zones identified by corridors both at the regional and global scale. The strike-slip tectonics seem to play a key role in the satellite's structural evolution, in the possible transition from dark to light terrain and in the understanding of the stress that generates the grooves and furrows (e.g., Seifert et al., 2015). Ongoing work on global structural mapping, based on both Voyager and Galileo images, combined with geodynamic investigations, is in progress to further improve the understanding of the tectonics of Ganymede.

Acknowledgements

We thank E. Hauber and an anonymous reviewer for insightful comments that improved the manuscript. Funding for this project came from Roma Tre University (fellowship) and the Roma Tre GeoQuTe lab, project RP-03. This work has been completed as part of the PhD project of the first author. We thank the Laboratory of Geodynamics and Planetary Sciences of the University of Nantes for their kind hospitality and the CNRS for the fellowship in France. The mosaics, the complete tables, and data are available from the corresponding author (costanza.rossi@uniroma3.it).

2.2 Structural geology of Ganymede regional groove systems (60°N – 60°S)

The material of this section has been published in Journal of Maps: Rossi, C., Cianfarra, P., Salvini, F. (2019). Structural geology of Ganymede regional groove systems (60°N-60°S). Journal of Maps. https://doi.org/10.1080/17445647.2019.1685605. The 'Structural geology of Ganymede regional groove system (60°N – 60°S)' map is attached at the end of the thesis.

Abstract

Brittle deformation on Ganymede surface is represented by tectonic linear landforms, the grooves. These are regional scale, elongated structures that show well-defined morphology from straight to curvilinear. High density of grooves occupies most of the younger light terrain of the satellite, i.e. the grooved terrain. We map these structures on the USGS Voyager and Galileo Mosaic of Ganymede in order to unravel their spatial distribution and tectonic setting. A total of 14707 grooves were identified, digitized and statistically analysed. A quantitative structural geology approach was used to classify these structures, taking into account their azimuth and including regional rotation. This procedure allowed to recognize a total of four groove families, named according to their main orientation, the NE, WNW, NW, and N-S super-systems. The presented structural map represents a tool to study the stress conditions associated to the groove formation and evolution. This map also aims to contribute to the scientific preparation of the upcoming mission programs and future exploration of Ganymede.

1. Introduction

Planetary missions successfully have been exploring the Outer Solar System for the last decades (e.g. Pioneer, Voyager, Galileo and Cassini-Huygens programs, Smith et al., 1979a; Fimmel et al., 1980; Young, 1998; Matson et al., 2003). Their discoveries provided information on the gas giant planets and their moons. Ganymede is one of the icy satellites of the Jovian System and represents a primary target for planetary exploration. It is a candidate for habitability as a potential world that hosts life (Prieto-Ballesteros et al., 2012; Grasset et al., 2013; Vance et al., 2018). It is the largest satellite in the Solar System with a radius of 2631.2 ± 1.7 km (Anderson et al., 2001) and presents the lowest moment of inertia (0.3115±0.0028, Anderson et al., 1996; Schubert et al., 2004; Hussmann et al., 2007) as provided by gravity data and confirmed by geophysical models (e.g. Kirk and Stevenson, 1987). This implies a highly differentiated internal structure constituted by a metal rich core and a silicate mantle surrounded by a water-ice crust (Anderson et al., 1996; Deschamps and Sotin, 2001; Schubert et al., 2001; Sohl et al., 2002). The icy crust is composed by ice-Ih, ice-

III, ice-V, and ice-VI. A liquid water layer is inferred to be located between ice-Ih and the high-pressure ice layers (i.e. ice-III; Hussmann et al., 2007). This water layer constitutes a subsurface ocean (Fanale et al. 1977; Kirk and Stevenson 1987; Ojakangas and Stevenson 1989; Moore and Schubert 1996; Khurana et al. 1998; Carr et al. 1998; Pappalardo et al. 1999; Kivelson et al. 2000), that is supposed to contribute to the formation of the intrinsic magnetic field of Ganymede, induced by the presence of conducting fluid and salty layer (Sarson et al., 1997; Sohl et al., 2002; Kivelson et al., 2002; Schubert et al., 2004). The magnetic field of this satellite may also relate to a dynamo mechanism in the metallic core (Schubert et al., 1996).

The surface of Ganymede is subdivided into two main terrains (Fig. 1). These are the dark and the light terrains (Smith et al., 1979b; Shoemaker et al., 1982; Patterson et al., 2010; Collins et al., 2013) and show distinct surface characteristics including different albedo, crater density and morphotectonic structures (Lucchitta, 1980; Parmentier et al., 1982; Bianchi et al., 1986; Murchie et al., 1990; Prockter et al., 1998, 2000; Patterson et al., 2010; Collins et al., 2013). The dark terrain covers 35% of the surface and it is characterized by relatively low albedo material (0.26±0.05 according to Helfenstein et al., 1997) and high crater density, whose measurement suggests an age of around 4 Gyr (Zahnle et al., 1998, 2003; Nimmo and Pappalardo, 2004). They are characterized by large-scale, arcuate fracture systems termed furrows, that have been hypothesized to be impact-related as the remnants of a system of concentric rings and radial fractures produced by large impacts occurred in the early history of Ganymede, when its icy crust was thinner (McKinnon and Melosh, 1980; Casacchia and Strom, 1984; Schenk and McKinnon 1987, Murchie et al., 1990; Prockter et al., 1998). Furrows are mainly cut by younger landforms, craters, and by the light terrain regions. The dark terrain shows local areas, the lineated units according to Patterson et al. (2010) and Collins et al. (2013), where linear fractures lie in between the dark and the light terrains. These units represent possible key area to understand the relation and transition between the two terrains (Prockter et al., 2000; Rossi et al., 2018).

The other 65% of the satellite surface is covered by the light terrain and is characterised by higher albedo (0.42±0.04, Helfenstein et al., 1997). It shows lower crater density that provides a younger age of around 2 Gyr (Zahnle et al., 2003; Nimmo and Pappalardo, 2004). Craters within the light terrain are almost completely obliterated by the presence of numerous morphotectonic lineated landforms, termed grooves (Fig. 2). The light grooved terrain of Ganymede (Lucchitta, 1980; Patterson et al., 2010) represents one of the most tectonically disrupted surfaces of the Solar System. The high density of morphotectonic structures within the light terrain, together with the lower crater counting, confirms the more recent activity of this terrain. A map of the Ganymede grooves has been proposed by Collins et al. (2000).

In this work we investigate and map the pattern of Ganymede regional grooves with the preparation of a structural map for a better comprehension of their characteristics and relationships. Results show that groove structures behave as regional swarms/systems with their own characteristics and structural meaning. In this way, the proposed map considers the sets of regional grooves and shows their regional, organized clustering into systems.

The map represents a base that can be used to investigate the tectonic mechanisms affecting the satellite light terrain as well as to clarify the operating geodynamic processes. We unravel the most recently active regions of Ganymede, that are the light terrain deformed by grooves. The main differences between grooves and furrows are age, spacing, morphology, and supposedly origin (Patterson et al., 2010; Rossi et al., 2018). The furrow impact origin took place before the period of grooved terrain formation, as evidenced by the abrupt transection relationships of the two terrains (McKinnon and Melosh, 1980). Due to their external cause, furrows were ignored in the preparation of the final map and their investigation is beyond the goals of the presented structural map, that focuses on the more recent tectonic processes and on the internal geodynamic factors ruling the present-day groove characteristics and geometries.

Grooves play a key role for the possible connection between surface and the subsurface ocean and represent the evidence of tectonic activity that deformed the satellite surface during its geologic evolution.

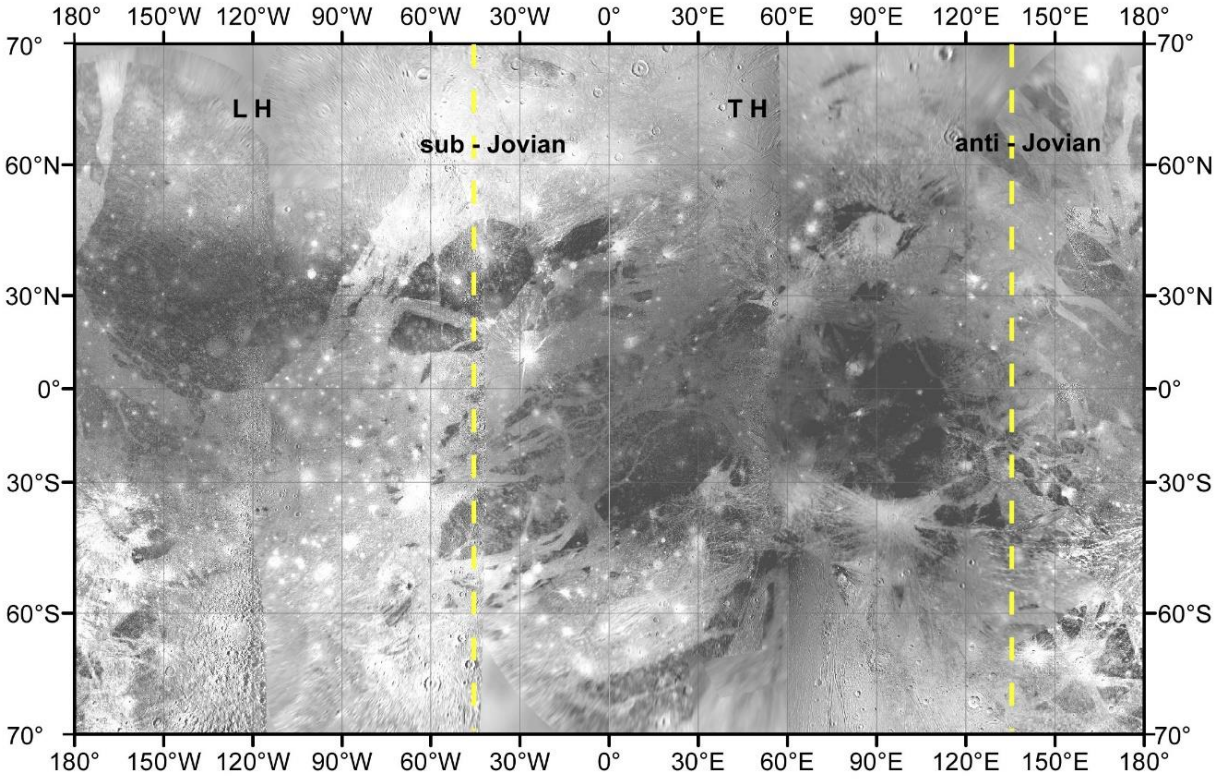

Fig. 1: Ganymede Voyager and Galileo Global Mosaic, Mercator projection. The dashed yellow lines define the boundaries of the leading (LH in figure) and the trailing (TH) hemispheres at the W and E, respectively.

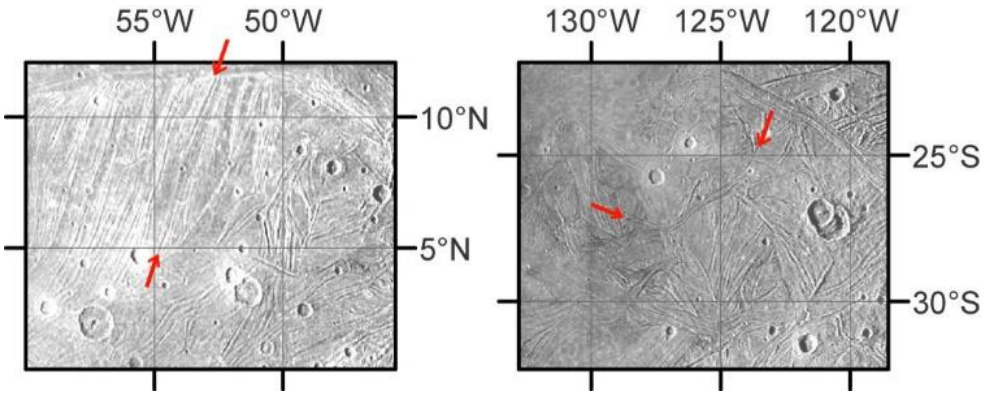

Fig. 2: Grooved terrain. The red arrows show groove examples.

1.1 Grooves of Ganymede

Grooves are common, rather linear, structural elongated landforms occurring on the surface of several small bodies of the Solar System as Phobos, Phoebe, Gaspra, Ida, Eros (Morrison et al., 2009; Watters and Schultz, 2010). Their morphology varies from linear surface depressions to curvilinear and/or rows of coalesced pits, with lengths spanning from 5 km to over 50 km. Typically they are 100-200 km long and nearly less than 100 m deep (Watters and Schultz, 2010). It is assumed that grooves of the mentioned bodies are subsurface fractures likely produced from extensional tectonic processes (Thomas, 1989; Prockter et al., 2002; Watters and Schultz, 2010). It is generally assumed that grooves are associated with internally-driven tectonics on larger satellites such as Europa, Ganymede, Enceladus, Tethys, and Mimas (Pappalardo, 2006; Morrison et al., 2009; Watters and Schultz, 2010).

Planetary-wide grooved terrains have been firstly observed on the Ganymede surface (Lucchitta, 1980; Parmentier, 1982; Shoemaker et al., 1982). Grooves of Ganymede (Fig. 2) represent the brittle deformation of the light terrain of the satellite. They occur, as observed at the regional scale, clustered into sets of grooves with length > 100 km and average spacing of about 10 km (Lucchitta, 1980; Casacchia and Strom, 1984; Bianchi et al., 1984; Pappalardo and Greeley, 1995; Pappalardo et al., 1998; Collins et al., 2000; Pappalardo et al., 2004; Patterson et al., 2010; Collins et al., 2013). They often cluster in nearly parallel ordered patterns.

The stress fields and the tectonic processes that generate grooves remain still unclear. Authors (e.g. Lucchitta, 1980; Parmentier, 1982; Shoemaker et al., 1982; Squyres and Croft, 1986; Philpott, 1988; Pappalardo et al., 1998; Collins et al., 1998; Bland and Showman, 2007; Pizzi et al., 2017) interpret the global assemblage of Ganymede grooves as extensional zones similar to the Earth continental rifts, resulting from the global expansion that affected the satellite crust in the past. In addition to normal faulting, strike-slip motion was observed within small regions of grooved terrain (Lucchitta, 1980; Murchie and Head, 1988; Pappalardo et al., 1998; Collins et al., 1998; Pappalardo and Collins,

2005; Cameron et al., 2018). More recently, a regional scale shear component is suggested to play a key role for the evolution of large grooved terrain regions (Seifert et al., 2015; Cameron et al., 2018; Rossi et al., 2018). Several regions imaged by the Galileo spacecraft were investigated applying structural geological methodologies. Dardanus Sulcus is centered at 17.5° S, 342.5° E and both extension and right-lateral strike-slip tectonics originated its grooves (Cameron et al., 2013; Seifert et al., 2015; Cameron et al., 2016; 2018). Arbela Sulcus (21.1° S, 10.2° E) was formed, similarly to Dardanus Sulcus, by an extension event dissecting the upper crust (Giese et al., 2001; Head et al., 2002; Berquin et al., 2013) with a left-lateral shear component (Head et al., 2002; Cameron et al., 2018). Events of tectonic deformation suggesting extensional and strike-slip regimes were proposed also for Nun Sulci grooves (49.5° N, 43.6° E; Murchie and Head, 1988; Seifert et al., 2015; Cameron et al., 2018), Nippur/Philus Sulcus (36.9° N, 175° E), Byblus Sulcus (37.9° N, 160.1° E) and Anshar Sulcus (18°N, 162.1° E) (Cameron et al., 2018 and references therein). Tiamat Sulcus (3.4° N, 151.5° E) and Kishar Sulcus (6.4° S, 216.6° W) represent a labyrinth of intersecting grooves suggesting strike-slip shear (Murchie and Head, 1988; Bedle and Jurdy, 2005; Cameron et al., 2016; 2018) as well as in Harpagia Sulcus (11.8° S, 313.5° W; Head et al., 2002; Berquin et al., 2013). Uruk Sulcus is a broadly studied light terrain of Ganymede. Studies on a target site of this sulcus (0.8° N; 199.7° E) imaged within the sulcus at high-resolution by Galileo probe infer extension with normal faulting, graben and domino style mechanisms (Pappalardo et al., 1998). These Authors recognized also local transtensional shear within it. More recent investigations based on the Voyager imagery of Uruk Sulcus at regional scale allowed to recognize the consistent role of transpressional strike-slip kinematics along the region with significant compressional component (Rossi et al., 2018).

Despite these numerous studies, the regional geological setting of most grooved terrain is still poorly known. In this way, a map of classified Ganymede grooves represents a tool to improve the knowledge on the tectonic evolution of the satellite. The map highlights the spatial organisation of these features, i.e. their spatial distribution, crosscutting relationship, and azimuthal clustering. This

mapping represents a tool to recognize the spatial distribution of these properties. Manually detected grooves of Ganymede were quantitatively classified into regional systems by a structural geology approach. This map represents the tool to further investigate the stress conditions associated to the groove formation and evolution. This information is relevant to the preparation of future space missions.

2. Data

Ganymede imagery derives from planetary missions across the Outer Solar System. The high-resolution images used in this work belong to the Wide Angle Camera (WAC) and Narrow Angle Camera (NAC) onboard the twin Voyager 1 and 2, and the Galileo Solid State Imaging (SSI) camera that largely covered the satellite (a full set of these image data is available on http://pds.jpl.gov).

The mapping was based on the remote sensing investigation of a monochrome base map of the satellite released by the United States Geological Survey (USGS) Astrogeology Science Centre (available on http://astrogeology.usgs.gov). This is the Ganymede Voyager and Galileo Global Mosaic, a Mercator projected map derived from the mosaicking of the best image quality and resolution coverage (from 20 km/pixel for gap fill to approximately 400 meters/pixel) supplied by NAC and SSI cameras (Fig. 1; Becker et al., 2001). Most of the best data of Voyager and Galileo were obtained within the leading hemisphere of Ganymede (Fig. 1).

3. Structural mapping

Regional grooves of Ganymede were mapped between 60°N and 60°S and digitized in a geographic information system (GIS) geodatabase.

Image with low-resolution and high geometric distortion in some areas of the satellite prevented their use for mapping purposes. For this reason, grooves were mapped on approximately 36% of the light terrain (as mentioned, about 50% of the light terrain images were not acceptable for manual mapping).

The polar regions were excluded in this work due to the distortion limits of most of the available images for these.

A total of 14707 groove structures have been recognized and digitized between 60°N and 60°S (Fig. 3). A lack of data occurs in the region included within 60°E and 80°E due to the low-resolution of the available images (resolution lower than 2000 m/pixel). This zone partly falls of the anti-Jovian hemisphere of Ganymede.

Mapped grooves are considered as the topographic expression of trough structures. Their bottom is recognized thanks to the luminosity contrast resulting by the solar lighting conditions. Grooves with higher tonal intensity were digitized as polylines. These were quantitatively analysed according to the azimuth of their segments. Statistical analyses of the identified grooves allow to classify the majority of these structures into clusters of azimuthal families.

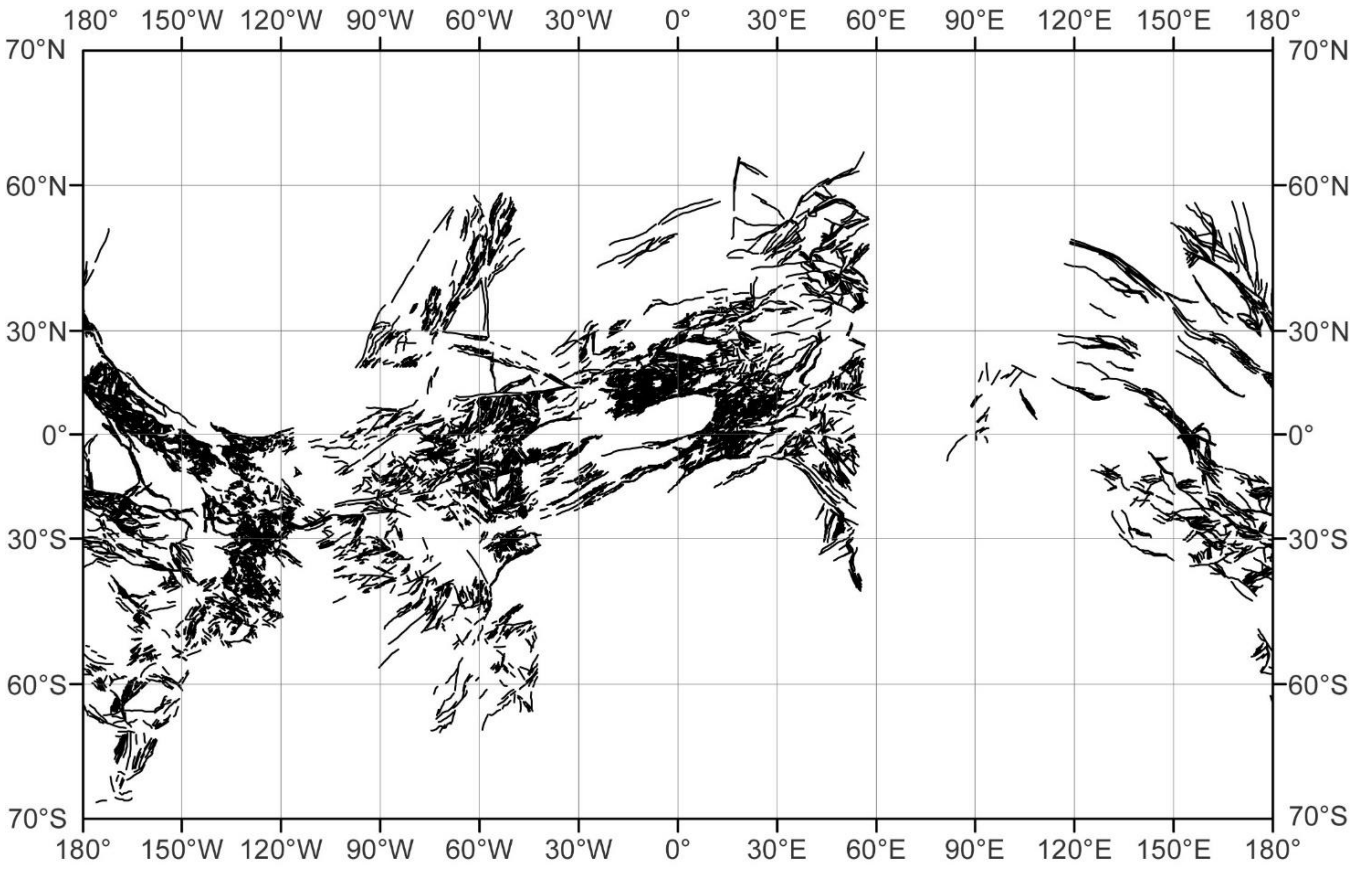

Fig. 3: Grooves global mapping, Mercator projection. A total of 14707 groove structures are shown.

3.1 Azimuthal analysis

The grouping of the families of grooves into regional systems is based on their azimuths and spatial distribution. Each groove is represented as a georeferenced series of contiguous segments (a total of 50717 segments forming 14707 polylines) characterized by their azimuths and lengths. The preliminary azimuthal frequency analysis of the total segments is presented in Fig. 4. This process includes the polymodal analysis by best fit of the frequency histogram with a function sums of Gaussian curves (Daisy version 5.36.71; Salvini, 2019). This allows to recognize the presence of multiple preferred orientations (i.e. relative maxima in the histograms) and to characterize each azimuthal cluster with its statistical parameters: mean azimuth, standard deviation, and relative height (Wise et al., 1985; Cianfarra and Salvini, 2016a). Results show that groove segments cluster into 4 preferred orientations, namely: N61°E, N68°W, N37°W, and N10°E (Fig. 4). Considering the rotation produced by the almost spherical geometry of Ganymede surface and to follow possible regional rotations within each group, the grooves classification was performed by the comparison of their azimuths within a spatial grid of circular areas. The grid resolution pace was 20° of latitude and longitude in a hexagonal shape. A diameter of 6000 km was chosen for each circular area to guarantee the partial overlap between adjacent circular analyses and to ease the detection of continuity among the analyses (Fig. 5). The specific approach we used in searching for groove swarms accomplishes for swarm rotations due to both the spherical shape of the surface and possible swarm rotation across the regions. This has been obtained by comparing the found Gaussian peak among the results of adjacent analyses. This procedure automatically takes care of both distortion/rotation.

A total of 148 circles form the grid. For each circle the azimuthal frequency analysis of the segments of the internally falling grooves was performed to identify the preferred orientations within the considered circle. Azimuthal groups are presented in Fig. 5 in the form of oriented lines (i.e. Gaussian peaks) proportional to the relative importance in wind-rose diagrams centered at the grid nodes. These Gaussian peaks were then grouped by comparing their mean azimuth with the Gaussians of the

surrounding analyses. Among the unclassified Gaussians (obviously all of them in the first cycle) the largest Gaussian is identified by their relative height and corresponding number of segments and it becomes the seed of the system to be identified. Then its azimuth is compared with the azimuths of the Gaussians in the 6 surrounding analyses. In each of them, the Gaussian with the closest mean azimuth and having an angle to the seed smaller than a given reference value (5° for this analysis) is classified as belonging to the searched system. Then each newly classified Gaussian becomes a seed for the search of the system and the process is repeated in a recursive way (forest-fire process, Turcotte, 1997) until no contiguous analyses have Gaussians associable to the system (i.e. all the remaining unclassified Gaussians forming angles larger than the reference one) or all the analyses have been inspected. This process is repeated by identifying a new seed Gaussian to search for other systems until all Gaussians have been classified (Fig. 5). Spatial rotation of grooves systems is guaranteed by the tolerance of rotations between adjacent peaks to pertain to the same system (5°/6000 km in this study). The result of this analysis brought to the identification of 23 systems, formed within the 361 found Gaussians and is presented in Fig. 6 where the systems are colour coded. The further azimuthal analyses of found Gaussians allow to group the found systems to form 4 super-systems, with azimuthal intervals: the NE super-system N61°E ± 17°, the WNW super-system N68°W ± 11°, the NW super-system N37°W ± 11°, and the N-S super-system N10°E ± 13°. Segments are then associated to the found systems in a similar procedure. Their azimuths are compared to the Gaussians from the analysis of the circular areas where the groove falls, and it is associated to the system having the smallest angle to the corresponding Gaussian mean azimuth and lower than a reference minimum (20° in this study). When the last requirement is not satisfied, the segment is associated to the null (0) system and remains unclassified. As a result, Grooves are associated to super-systems by associating to each groove the system that is best represented within its segments.

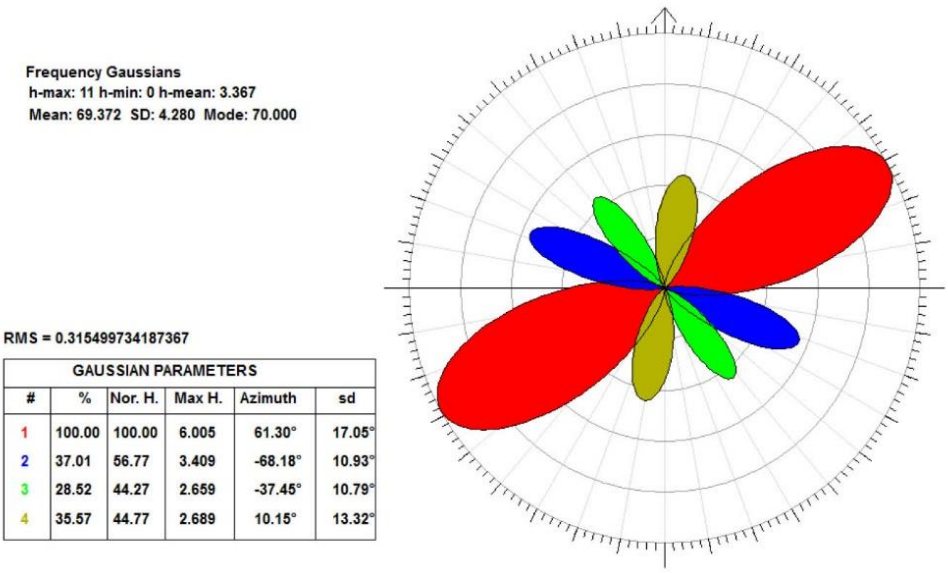

RMS = 0.315499734187367

GAUSSIAN PARAMETERS					
#	%	Nor. H.	Max H.	Azimuth	sd
1	100.00	100.00	6.005	61.30°	17.05°
2	37.01	56.77	3.409	-68.18°	10.93°
3	28.52	44.27	2.659	-37.45°	10.79°
4	35.57	44.77	2.689	10.15°	13.32°

Fig. 4: Azimuthal analysis of all the mapped grooves. The Gaussian Parameters are reported: the number of Gaussian peaks (#), the percentage of occurrence (%), the Normalized Height (NorH), the Maximum height (MaxH), the azimuth, and the standard deviation (sd). The preferential Gaussian peaks represent the azimuthal interval for the classification into super-systems.

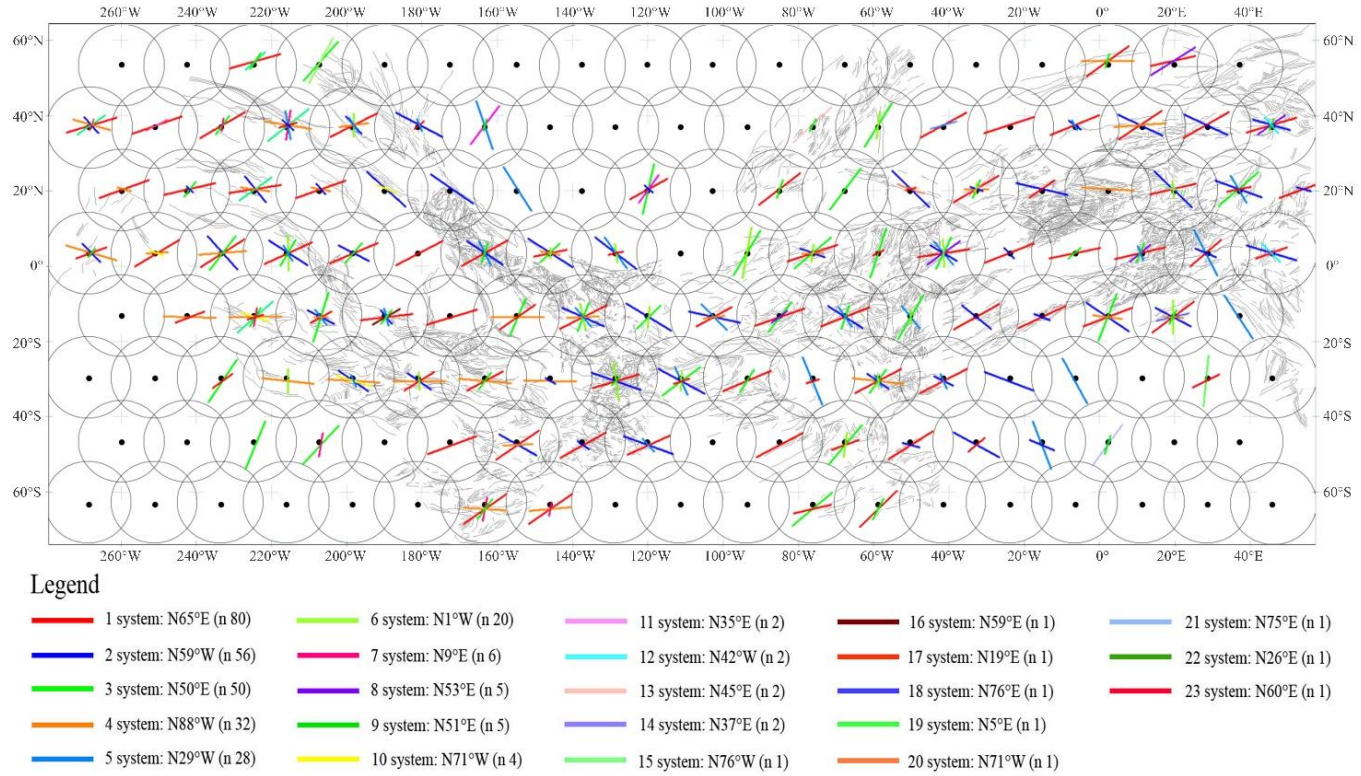

Fig. 5: Azimuthal grid analysis, Equidistant Cylindrical projection. Circles of the grid are represented as their mean dimension at the equator. In the circle centers are shown the classified Gaussians; in background the mapped grooves are represented. The legend explains the mean azimuth and the peak number (n) of each system of the grid analysis.

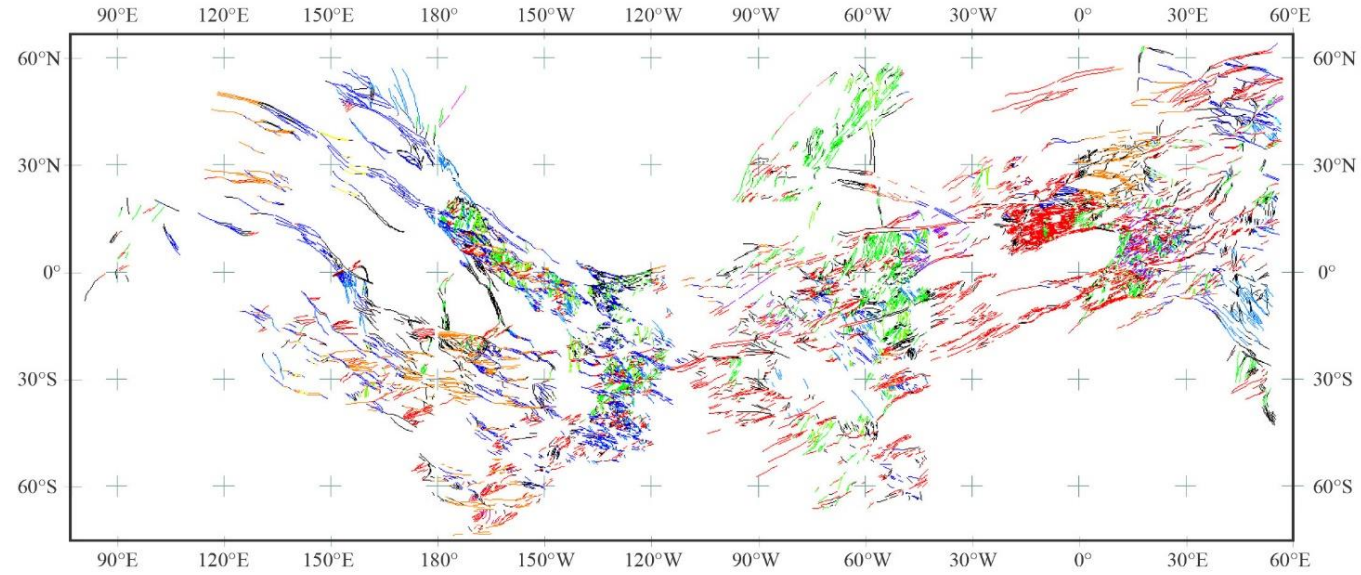

Fig. 6: Identification of the 23 main systems associated to super-systems shown in Fig. 4. Color-coded legend is reported in Fig. 5; black lines represent unclassified groove elements.

4. Groove super - systems

A total of 14707 grooves (i.e. polylines) were analysed and are shown in the map. The classified structures represent super-systems, groups of grooves that locally crosscut and intersect each other, and are globally arranged according to azimuthal/spatial clustering. At the regional scale they cluster to form 4 super-systems, distributed all over the investigated surface. Strong evidence of clear crosscutting relationships is difficult to identify among the found super-systems. Conversely, several local areas show a recognizable chronological sequence. The classification allows to identify a total of 4 super-systems, composed by 11402 grooves, and left unclassified 3305 ones.

The largest super-system is the NE super-system (3992 grooves). It is represented in red colour in the map and shows a mean direction of N61°E. Its spatial density is higher between approximately 120°W and 50°E, where it presents the longer grooves. This region corresponds to Babylon Sulci and Phrygia Sulcus, where grooves of this super-system mainly cut the other ones.

The second super-system is the WNW super-system (2898 grooves). It is represented in blue colour in the map and shows a mean direction of N68°W. It mainly occurs between 120°E and 120°W, corresponding to Tiamat Sulcus, Kishar Sulcus, Lagash Sulcus, Anshar Sulcus, Mashu Sulcus, Byblus Sulcus, Uruk Sulcus, and Nippur Sulcus. In these regions it presents the longer groove elements that mostly cut the other. Between 130°W and 120°W this super-system coexists with the NE one, and it is characterized by the similar crosscutting relationships of the NE super-system.

The third super-system is the NW one (1182 grooves). It is represented with light blue colour in the map and shows a mean direction of N37°W. It is mainly spatially distributed where the WNW super-system occurs. In this way, it is mostly present between 150°E and 120°W, groove clusters from this super-system are also present between 70°W and 50°W, and 45°E – 60°E, where they are cut by the grooves of the NE super-system.

The fourth super-system is the N-S (3330 grooves). It is represented with yellow colours in the map and shows a mean direction of N10°E. It mostly clusters between 90°W and 40°W, where it is mainly cut by the first super-system. Conversely, within 180° and 120°W it is mainly cut by the WNW super-system. Grooves from this super-system as well as from the NW one are notably shorter than the grooves of the other super-systems (groove mean length is about 90 km).

The unclassified grooves (3305 grooves, in black colour in the map) present an un-clustered organisation and are evenly distributed on Ganymede light terrain.

5. Discussion

Grooves of Ganymede group into organised azimuthal families with small internal rotation through the Ganymede surface. The performed classification allows to recognize groove azimuthal super-systems developed at the global scale. Specific main orientations were identified and reflect the tectonic setting of the regions where they develop across the satellite surface. The chronological succession is difficult to be unravelled at the regional scale, and it was not possible to recognize a definitive relative chronological sequence of the found super-systems.

The global geologic map of Ganymede (Collins et al., 2013) determined the relative age relationships among the recognized units based on cross-cutting relationships and divided the light material units into three relative age categories.

The comparison of the found super-systems with these units and their proposed relative age (Collins, 2009; Patterson et al., 2010; Collins et al., 2013) allows to roughly recognize a relative time sequence of the found super-systems. By taking into account that this comparison is between groove structures and terrains, we can assume that the NE and the WNW super-systems mostly occur in the youngest light material units; the NW and the N-S super-systems mostly occur within the intermediate units. The oldest units mainly correspond to the location of the N-S super-system.

On the other hand, the super-system spatial organisation provides information about the tectonics that caused them. The super-system framework distinguishes provinces that are characterized by different stress regimes. Grooves of super-systems are often distributed following recognizable geometries. The presence of longer and parallel grooves that bound areas with shorter grooves is common. These longer elements seem likely to act as main shear boundaries that confine elongated region of deformation characterized by the presence of shorter and closer elements. This resembles regional corridors on the Earth surface (Storti et al., 2003, Cianfarra and Salvini, 2014; Cianfarra and Salvini, 2015; Cianfarra and Salvini, 2016b; Maggi et al., 2016; Cianfarra and Maggi, 2017; Pinheiro et al., 2019). Several areas of Ganymede light terrain follow a similar corridor geometry associated to strike-slip kinematics. At the regional scale, Authors (e.g. Rossi et al., 2018) recognized this setting within Uruk Sulcus area, that is suggested to be a strike-slip corridor. Babylon Sulci also may represent a similar example of this strike-slip setting (from 70°W to 30°W). There the NE super-system delineates longer and sub-parallel grooves that enclose shorter grooves with different directions. Other examples produced by the NE super-system are found within Phrygia Sulcus. This confirms the key role that the strike-slip tectonic regime plays at the regional scale, as already observed at the local one (Murchie and Head, 1988; Pappalardo et al., 1998; Giese et al., 2001; Head et al., 2022; Bedle and Jurdy, 2005; Berquin et al., 2013; Seifert et al., 2015; Cameron et al., 2018). Often the transition between the dark and the light terrains is characterized by the presence of isolated grooves of the super-systems (mainly the NE and the WNW one). Their length and well-defined evidence suggest a kinematic origin. This strengthens the importance of horizontal displacement between the terrains.

The map reports two distinct regions where the NE and the WNW super-systems prevail. The NE super-system mainly occupies the so-called trailing hemisphere of the satellite, and the WNW one mostly develops in the leading hemisphere (Fig. 1). The NE and the WNW super-systems systematically cut the other super-systems. Their activity may partially relate to tidal process that

influence the spatial arrangement of the NE and WNW super-systems. The sub- and anti-Jovian hemispheres show a similar distinction (Fig. 1). It is observed a prevalence of the NE super-system within the sub-Jovian hemisphere, and a prevalence of the WNW super-system within the anti-Jovian one.

Part of the anti-Jovian hemisphere of Ganymede lack significative information due to the low resolution of the available imagery. This precludes interpretation regarding the effects of tidal process in the anti-Jovian hemisphere.

It is possible that tidal heating coexisted together with other geodynamic processes as convection (e.g. Hammond and Barr, 2014), near surface partial melt (e.g. Bland et al., 2009), and/or polar wandering (e.g. Murchie and Head, 1986; Mohit et al., 2004; Matsuyama et al., 2014).

This map represents the base for future structural researches and exploration of the satellite. The distribution and characteristics of mapped grooves are strictly related to anisotropy of the terrain (both crustal thickness and rheology/composition) that will be significant for the programmed radar instrumentation (e.g. Radar for Europa Assessment and Sounding: Ocean to Near-surface, REASON, Pettinelli et al., 2015; Radar for Icy Moon Exploration, RIME, Bruzzone et al., 2013). The identified groove azimuths will be useful to identify regions where to acquire the optimal data and to avoid intense clutter returns (Ilyushin et al., 2017).

6. Conclusions

The presented structural map of Ganymede regional groove systems shows the spatial arrangement of the regional grooves into super-systems. They represent the effect of the tectonics on the satellite and their mapping identifies distinct geometries that provide information on the tectonic setting. The map derives from a systematic investigation and represents an important tool to study groove pattern and clustering.

A total of 14707 grooves were identified and reported on the map. Azimuthal analysis allowed to classify a total of 11402 (77.5%) grooves into 4 super-system regionally distributed, that show an arrangement similar to the strike-slip corridors of the Earth. This classification leaves unclassified 3305 (22.5%) scattered grooves.

The two main super-systems, namely the NE and WNW ones, preferentially occupy the leading and the trailing hemispheres, respectively. Tidal deformation may be responsible for the symmetrical pattern of these super-systems.

This map is a useful tool for future more detailed structural analyses to investigate the groove spatial distribution, the processes that led to their formation, and their possible fractal distribution (Lucchetti et al., 2017).

The used statistical approach represents an effective method to classify stress-related structures. It may contribute and provide potential support to study the geodynamic processes of the satellite.

Future missions that will provide a better quality of image coverage, allow to complete the mapping also of the polar regions and the low-resolution quadrant of the anti-Jovian hemisphere. This map improves the knowledge of the surface environment for the future exploration of Ganymede.

SOFTWARE

The structural map of Ganymede regional groove systems was prepared by using the QGIS software. Azimuthal analyses were performed by using the DAISY3 software developed by F. Salvini and freely distributed at: http://host.uniroma3.it/progetti/fralab.

Acknowledgements

We kindly acknowledge Makram Murad-al-shaikh, Yaroslaw A. Ilyushin and Geoffrey Collins for the insightful comments that allowed to improve the manuscript and the map. Thanks to Federico Galetto for the assistance and useful comments. Funding for this project came from Roma Tre University (fellowship) and the Roma Tre GeoQuTe lab, project RP-03. This work has been completed within the PhD project of the first author.

2.3 Terrestrial analog of Ganymede

Antarctica presents several structures formed by glacier flows. Their kinematics and their connection with the underlying topography create brittle deformation represented by crevasses. These are caused by the stress on the ice due to their moving over the underneath rocky terrain. Glaciers fracture with typical patterns that depict the glacier dynamics. The analysis of crevasse patterns can tell us about the ice-dynamical processes within the glacier. These frequently occur at the lateral margins of a glacier, where lateral stresses against the valleys walls resists flow, at steep sections, at the ice front, or at the head of the glacier (Colgan et al., 2016). Crevasses are used to make inferences on shear and deviatoric stresses in a glacier, and their patterns and types indicate the mode of flow of a glacier (Freers, 1968; Colgan et al., 2016). According to the dynamics, the crevasses form: longitudinal crevasses that are generally originated by shear stress and transversal crevasses that are generally originated by deviatoric stress.

The Rennick Glacier in Antarctica (70°-72°S, 160°-162°E; Fig. 1) displays large amount of crevasse patterns that represent very good analog of Ganymede grooves. Fig. 2 shows a series of longitudinal crevasses formed by kinematic shear in the middle of the glacier. Two sets are recognized in figure. The main one is represented by curvilinear, equally spaced (approximately 15 m), and longer structures (more than 100 m long) that form corridor boundaries where the second set develops. This latter presents shorter structures (less than 30 m) with a typical “S” shape. The strike-slip regime in the middle of the glacier forms structure sets with similar tectonic setting of Uruk Sulcus region in Ganymede. The first structure set is analogous to the corridor boundaries that is formed by longer grooves, and the second one is analogous to the sigmoidal structures that formed within the sulcus.

Fig. 3 shows a large amount of longitudinal crevasses (approximately over 200 m long) present in the middle of the Rennick Glacier. Their setting similarly reproduces what shown in the structural map of the regional groove system of Ganymede.

In Fig. 4 longitudinal crevasses depict a corridor pattern as the Uruk Sulcus corridor in Ganymede. The figure shows longer crevasses (more than 200 m long) that delimit the boundary of the corridor where shorter structures (less than 30 m long) form.

Fig. 5 also shows longitudinal crevasses that constitute a corridor where internal and shorter crevasses form, as the GUS3 groove system recognized in Uruk Sulcus.

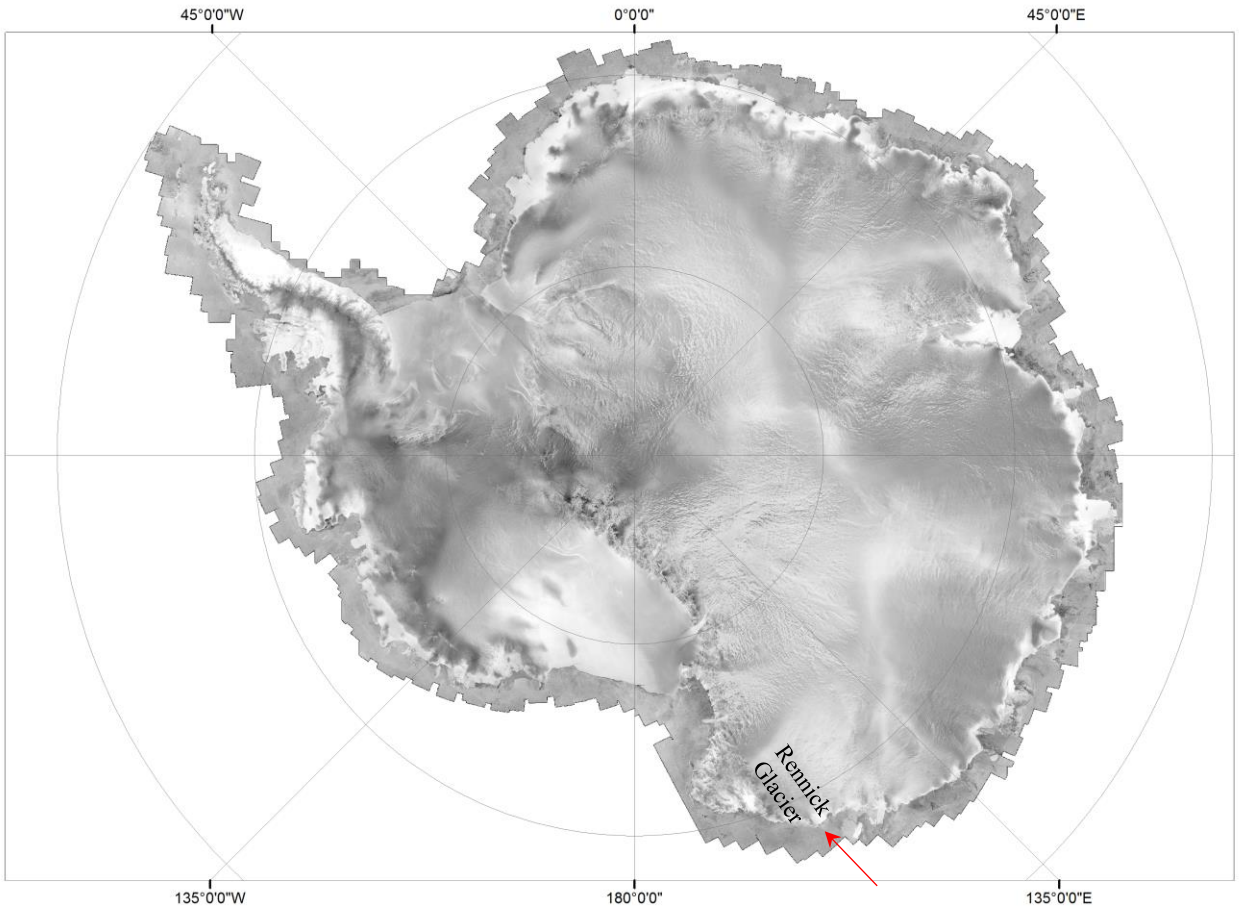

Fig. 1: Antarctica, RADARSAT mosaic. The red arrow shows the location of the Rennick Glacier (70°-72°S, 160°-162°E).

Fig. 2: Aerial view of longitudinal crevasses in the Rennick glacier, Antarctica. The black arrow shows the flow direction. PNRA XXXIV expedition.

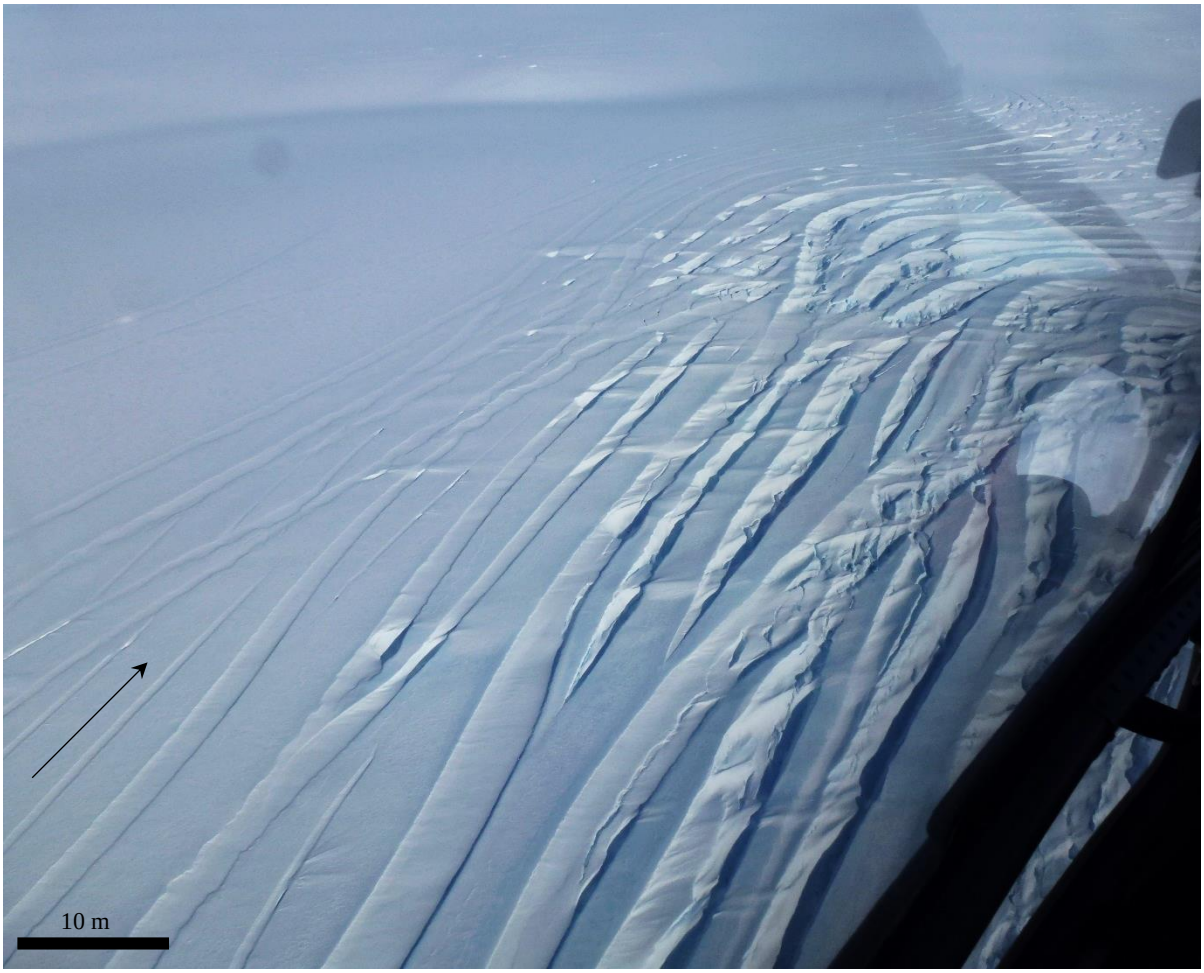

Fig. 3: Aerial view of longitudinal crevasses in the Rennick glacier, Antarctica. The black arrow shows the flow direction. PNRA XXXIV expedition.

Fig. 4: Aerial view of longitudinal crevasses in the Rennick glacier, Antarctica. The black arrow shows the flow direction. PNRA XXXIV expedition.

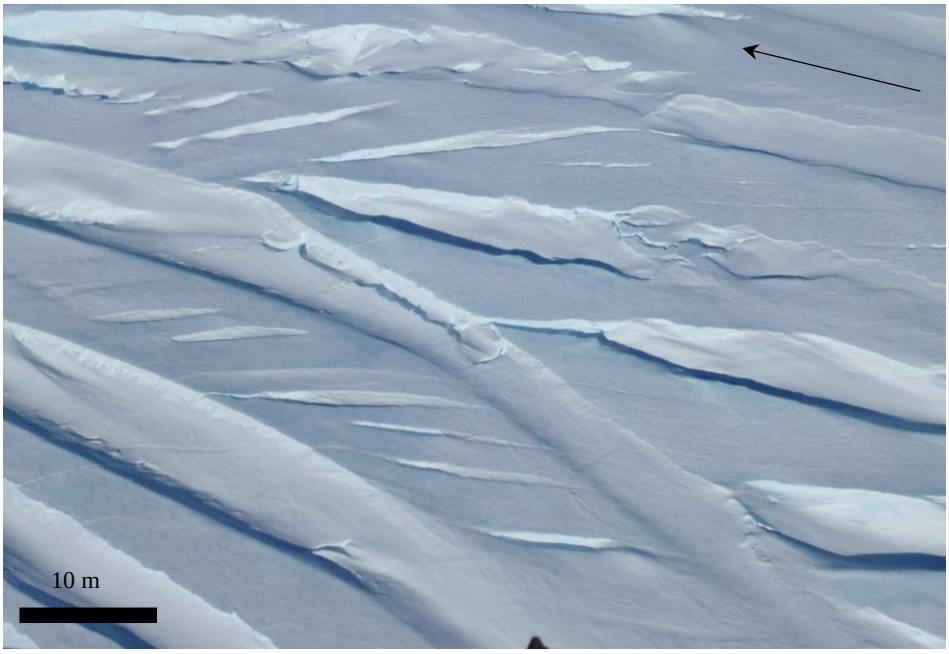

Fig. 5: Aerial view of longitudinal crevasses in the Rennick glacier, Antarctica. The black arrow shows the flow direction. PNRA XXXIV expedition.

CHAPTER 3

ENCELADUS

3.1 Tectonics of Enceladus South Pole: Block rotation of the Tiger Stripes

The material presented in this paragraph has been submitted to Journal of Geophysical Research: Planets and is subject to further revisions.

Abstract

The South Polar Terrain (SPT) of Enceladus is place of eruptions of gas and water ice particle plumes that testify to internal activity. These are located along series of tectonic structures, i.e. the Tiger Stripes fractures (TSF) that are comprised of regularly spaced and linear depressions. The SPT is surrounded by sinuous chains of ridges and troughs (the marginal zone). To unravel the tectonics that affect the region and its evolution, we performed comprehensive structural mapping and quantitative analyses of these brittle deformation features from remotely-sensed images. The results are consistent with a block rotation model, whereby several tectonic regimes coexist. The TSF are left-lateral strike-slip faults that bound rigid blocks. The blocks rotate clockwise and are enclosed in a regional scale right-lateral kinematics expressed in the marginal zone. These two opposite and complementary kinematic regimes induce transtensional and transpressional deformations within the SPT. An evolutionary tectonic model is proposed for the past and future evolution of the SPT. This model confirms the role of tectonic-related kinematics in icy satellites and contributes to the preparation of future missions.

1. Introduction

Observations of massive water vapor and ice-crystal plumes emanating from the South Pole region of Enceladus are amongst the most striking discoveries of the Cassini mission (Hansen et al., 2006; Porco et al., 2006; Spencer et al., 2006). The plumes reveal internal activity that occurs in the liquid layer under the icy crust of this satellite of Saturn. They are evidence of the underneath ocean activity and their composition is a clue for understanding the interior of this body (Matson et al., 2007). The buried ocean of Enceladus represents an environment potentially suitable for the growing of life (Parkinson et al., 2008), similar to those of the extreme environments of the black smokers along terrestrial ocean rifts (Tobie, 2015). The internal activity produces surface deformation including

brittle tectonics. Several fractures and faults that regionally deform the icy crust play a key role in understanding the active tectonic and geodynamic processes of the satellite (Crow-Willard & Pappalardo, 2015; Lucchetti et al., 2017; Porco et al., 2006; Yin & Pappalardo, 2015). The main fractures of Enceladus are the Tiger Stripe Fractures (TSF), located in the South Polar Terrain (SPT) and sites of plume eruptions (Fig. 1; Crow-Willard & Pappalardo, 2015; Porco et al., 2006). The TSF and other fractures that characterize the SPT represent weakness zones and potential connections between the surface and the underlying ocean (Lucchetti et al., 2017; Souček et al., 2019). We explore here the tectonic setting of the SPT. By means of structural geology mapping based on remotely sensed data, coupled with statistical and quantitative analyses, we investigate the effects of the tectonics to unravel and reconstruct the kinematic process that deforms the SPT region. We propose a kinematic model that frames the spatial distribution of the observed evidence of brittle deformation and provides new constraints on the geodynamic processes responsible for Enceladus internal activity.

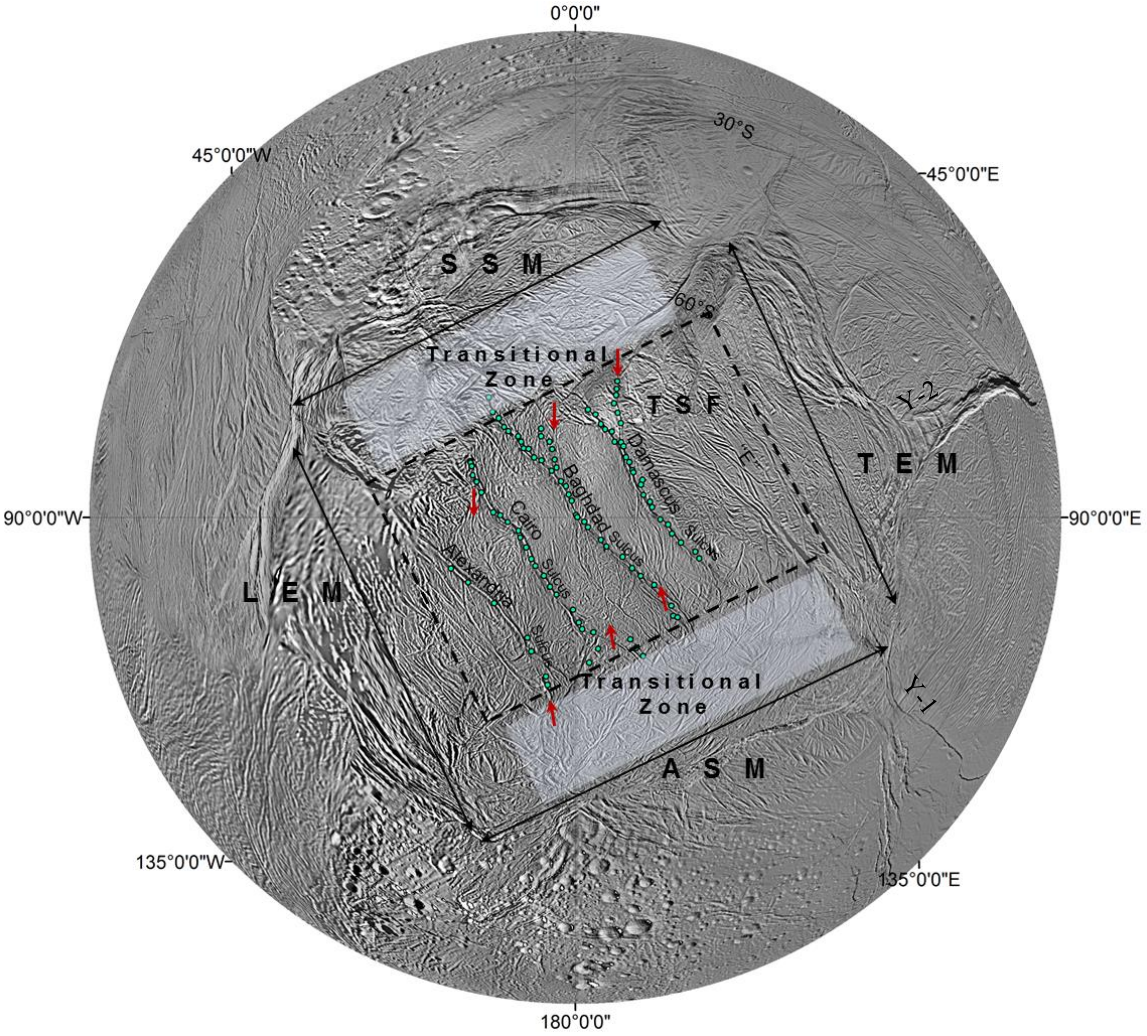

Figure 1. Enceladus South Polar Terrain (SPT), USGS Enceladus global mosaic orthographic projection. The Tiger Stripes Fractures (TSF) occur in the center of the region and are Alexandria Sulcus, Cairo Sulcus, Baghdad Sulcus, Damascus Sulcus, and the fracture zone "E". The light-green dots represent the plume source locations (Porco et al., 2014). The red arrows indicate the location and the orientation of the ancient Tiger Stripes (Patthoff & McKinnon, 2011). The structural units are illustrated. The marginal zone edges: Leading-edge Margin (LEM), Trailing-edge Margin (TEM), Sub-Saturnian Margin (SSM), and Anti-Saturnian Margin (ASM) (Yin & Pappalardo, 2015); the light squares show the transitional zone; the dashed square shows the TSF structural unit.

2. Geological and structural setting

Enceladus is a satellite of Saturn with a radius of 252.1 ± 0.2 km (Porco et al., 2006). It is located in the external E ring of Saturn and contributes to replenish it with the eruptive material of the plumes emanating from its south polar region (Helfenstein & Porco, 2015; Porco et al., 2006, 2014). The plumes are composed of water vapour, ice particles, and organic compounds (Filacchione et al., 2016; Gioia et al., 2007; Helfenstein & Porco, 2015; Hendrix et al., 2010; Johnston & Montési, 2017; Matson et al., 2007; Porco et al., 2006; Potsberg et al., 2018; Roberts, 2016; Scipioni et al., 2017; Thomas et al., 2016). They are possibly produced by sublimation above or below ground (Porco et al., 2006), and indicate internal activity of the satellite affected by tidal heating (Beuthe, 2016; Čadek et al., 2016; Choblet et al., 2017; Schenk & McKinnon, 2009; Thomas et al., 2016; Tobie et al., 2008). The surface is mostly composed by water, organic compounds and CO2 (Porco et al., 2006).

The satellite internal layering is subdivided into (1) a water ice shell characterized by 20-25 km average thickness that reduces to 5 km beneath the south pole (Čadek et al., 2016; LeGall et al., 2017), and exceeds 30 km in some equatorial regions (Lucchetti et al., 2017; Patthoff & Kattenhorn, 2011; Schenk & McKinnon, 2009); (2) a regional (Choblet et al., 2018; Collins and Goodman, 2007; Iess et al., 2014; McKinnon, 2015; Spencer & Nimmo, 2013) or global (Choblet et al., 2017; McKinnon, 2015; Patthoff & Kattenhorn, 2011; Thomas et al., 2016) water ocean with ammonia (Porco et al., 2006) 20-70 km thick (Johnston & Montési, 2017; Patthoff & Kattenhorn, 2011) and (3) a rocky core approximately 150-190 km thick (in radius; Čadek et al., 2016; Johnston & Montési, 2017; Roberts, 2016; Tobie et al., 2008).

Brittle deformation occurred during Enceladus history and formed regional-scale tectonic structures. A total of three main regions of deformation, each containing multiple structural units have been recognized. These are the South Polar Terrain (SPT), the Leading Hemisphere Terrain (LHT) and the Trailing Hemisphere Terrain (THT) (Crow-Willard & Pappalardo, 2015). They are arranged with similar morphological and structural setting where a belt of ridges and troughs circumscribe deformed

units. The region investigated in this work is the SPT region, where the cryovolcanic activity has been observed and with an age of 0.5 Ma (Crow-Willard & Pappalardo, 2015; Porco et al., 2006; Yin & Pappalardo, 2015) represents the youngest terrain of Enceladus surface. The SPT crust is 5 km thick, thinner than all other terrains (Čadek et al., 2016; Choblet et al., 2018; Helfenstein & Porco, 2015; Johnston & Montési, 2017; LeGall et al., 2017; Olgin et al., 2011). The origin of the activity occurring in this terrain is still an open question. Tidal heating (Beuthe, 2016; Choblet et al., 2017; Crow-Willard & Pappalardo, 2015; Patthoff & Kattenhorn, 2011; Schenk & McKinnon, 2009; Scipioni et al., 2017; Thomas et al., 2016; Tobie et al., 2008) may coexist with other processes such as convection (Barr, 2008; Crow-Willard & Pappalardo, 2015), crystallization of the internal ocean (Johnston & Montési, 2017), hydrothermal activity (Čadek et al., 2019; Choblet et al., 2017, 2018; Hsu et al., 2015), and polar wandering (Matsuyama & Nimmo, 2008; Nimmo & Pappalardo, 2006; Tajeddine et al., 2017).

The SPT can be subdivided into three structural units (Fig. 1). These are (1) the marginal zone, a circumferential belt represented by chain of ridges that surrounds the region (Yin & Pappalardo, 2015); (2) the Tiger Stripes; and (3) the zone that occurs between two edges of the marginal zone and the Tiger Stripes. This latter structural unit is called transitional zone in this study.

2.1 The Marginal Zone

The SPT, an area of about 70 000 km2 that extends from 50°S to the south pole, is circumscribed by the marginal zone, a complex pattern of sinuous subparallel ridges and troughs (Fig. 1). This chain is nearly rectangular in shape. It is formed by four different edge margins that are the Leading-edge Margin (LEM, between 60°W-160°W), the Trailing-edge Margin (TEM, between 40°E-120°E), the Anti-Saturnian Margin (ASM, between 120°E-160°W), and the Sub-Saturnian Margin (SSM, between 60°W-20°E) (Fig. 1; Yin and Pappalardo, 2015). Two arcuate arcs of morphotectonic features (Y-shaped cracks; Yin & Pappalardo, 2015) represent continuations along the TEM (Y-1 and

Y-2 in Fig. 1). The marginal zone is generally interpreted as a compressional zone (Crow-Willard & Pappalardo, 2015; Gioia et al., 2007; Johnston & Montési, 2017; Porco et al., 2006; Thomas et al., 2007). Yin and Pappalardo (2015) proposed the coexistence of several tectonic regimes for this structural unit. They suggest flow-like tectonics where a basal detachment connects extension with compression from the LEM to the TEM, accommodated by strike-slip kinematics at the SSM (left-lateral) and the ASM (right-lateral). Fig. 2 shows a schematic representation of the cross-section view of their model.

2.3 The Tiger Stripe Fractures

The Tiger Stripes represent one of the most interesting and puzzling features of Enceladus. These are four linear depressions, 130 km long, 500 m deep, 2 km wide, and about 35 km distant from each other (Gioia et al., 2007; Porco et al., 2006) with terminal tips in horsetail geometry. The TSF include Alexandria Sulcus (AX), Cairo Sulcus (CR), Baghdad Sulcus (BD), Damascus Sulcus (DM) (Helfenstein & Porco, 2015; Porco et al., 2006; Yin & Pappalardo, 2015). These fractures possibly play a key role in connecting the surface with the liquid ocean that is estimated to exist at a depth of 5 km below this area (Čadek et al., 2016; Choblet et al., 2018; Helfenstein & Porco, 2015; Johnston & Montési, 2017; LeGall et al., 2017; Olgin et al., 2011). They are also locations of the plume punctual sources (Fig. 1, light-green dots; Helfenstein & Porco, 2015; Porco et al., 2006, 2014;). A possible fifth Tiger Stripe, referred as zone "E" (Yin & Pappalardo, 2015), is located between Damascus sulcus and the TEM, and is supposed to be currently inactive due to the lack of observed erupting plumes (Porco et al., 2006, 2014). The TSF offset fractures morphologically similar to the present-day tiger stripes. These are supposed to be ancient TSF that behaved analogously before becoming inactive, and suggest a long geological history of tiger-stripe-like activity in the SPT (Fig. 1, red arrows; Patthoff & Kattenhorn, 2011). The areas delimited by the TSF present intensely folded terrain called the funiscular plains, reminiscent of pahoehoe lava flows (Fig. 2; Barr & Preuss, 2010;

Nahm & Kattenohrn, 2015; Spencer & Nimmo, 2013). The TSF have been interpreted either as extensional (Crow-Willard & Pappalardo, 2015; Gioia et al., 2007; Johnston & Montési, 2017; Thomas et al., 2007), or left-lateral strike-slip faults (Martin, 2016; Yin & Pappalardo, 2015).

2.3 The Transitional Zone

Southward of the marginal zone, the structural pattern changes. The transitional zone is spatially distributed within two areas located between the SSM and ASM edges and the tips of the TSF (Fig. 1). The tectonic structures of this unit are shorter than those of the marginal zone. These structures have been interpreted as continuations of the TSF that intersect the marginal zone (Yin & Pappalardo, 2015).

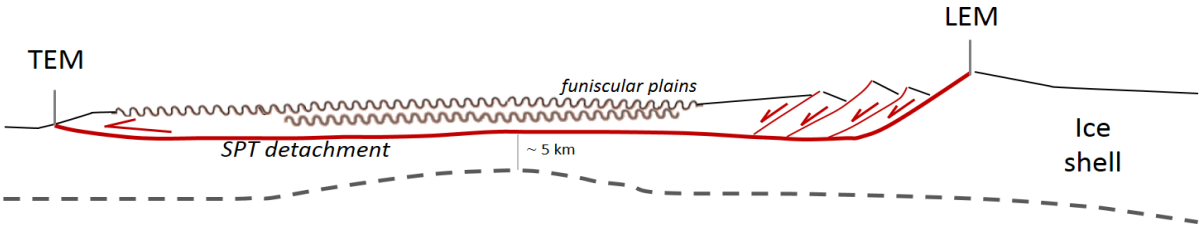

Figure 2. Scheme of the cross-section view of Yin and Pappalardo (2015) model. A basal detachment lies under the SPT region and produces flow-like tectonics from the extensional LEM to the compressional TEM. Folding (funiscular plains; Barr & Preuss, 2010) is produced within the TSF structural unit. (Modified from Yin and Pappalardo, 2015).

3. Structural analyses and results

The tectonic structures of Enceladus SPT were mapped using a geographic information system (GIS) geodatabase, and statistically analysed by mean of DAISY3 (Salvini, 2019) and SID software for automatic identification (Salvini et al., 1999). The analyses include the spatial distribution and azimuthal analysis (e.g. Pinheiro et al., 2019), the measurement of the Length-Spacing ratio (L/S; Cianfarra & Salvini, 2016a; Rossi et al., 2018; Salvini, 2013), the lineament domain analysis (Cianfarra & Salvini, 2014, 2015; Lucianetti et al., 2017; Rossi et al., 2018; Wise et al., 1985), and an ad-hoc image filtering strategy to infer the relationships between the pixel Digital Numbers (DNs)

response to the morphological periodicity. From these analyses, we classified the tectonic structures into different systems (Rossi et al., 2018).

3.1 Mapping

A total of 354 linear-to-curvilinear structures related to high tonal variation were identified on the Enceladus Cassini global greyscale mosaic containing the Cassini Imaging Science Subsystem (ISS) images of the USGS astrogeology program (Bland et al., 2018). This base mosaic has a spatial resolution that ranges between 50 and 500 m/pixel. Regional-scale structures with high tonal intensity were digitized as polylines, that represent the main structures at the observed resolution, and were classified according to their spatial distribution into the structural units that characterise the SPT, i.e. the marginal zone, the transitional zone and the TSF unit. The structures were classified into azimuthal systems, by means of quantitative statistical analyses (Fig. 3).

The marginal zone presents two systems. The first system occurs in the LEM-TEM edges (blue in Fig. 3) and it is characterised by sinuous structures; while the second system is present in the SSM-ASM edges (green in Fig. 3) with more straight structures. The transitional zone presents two systems characterized by short and straight structures (purple and red color in Fig. 3). Their similar crosscutting relationship suggests that they formed by the same dynamics. The TSF system is characterized by long structures (orange color in Fig. 3). The TSF cut and offset with sinistral displacement the other structures and their termination with horsetail geometry describe a S-shape along the SSM and the ASM edges.

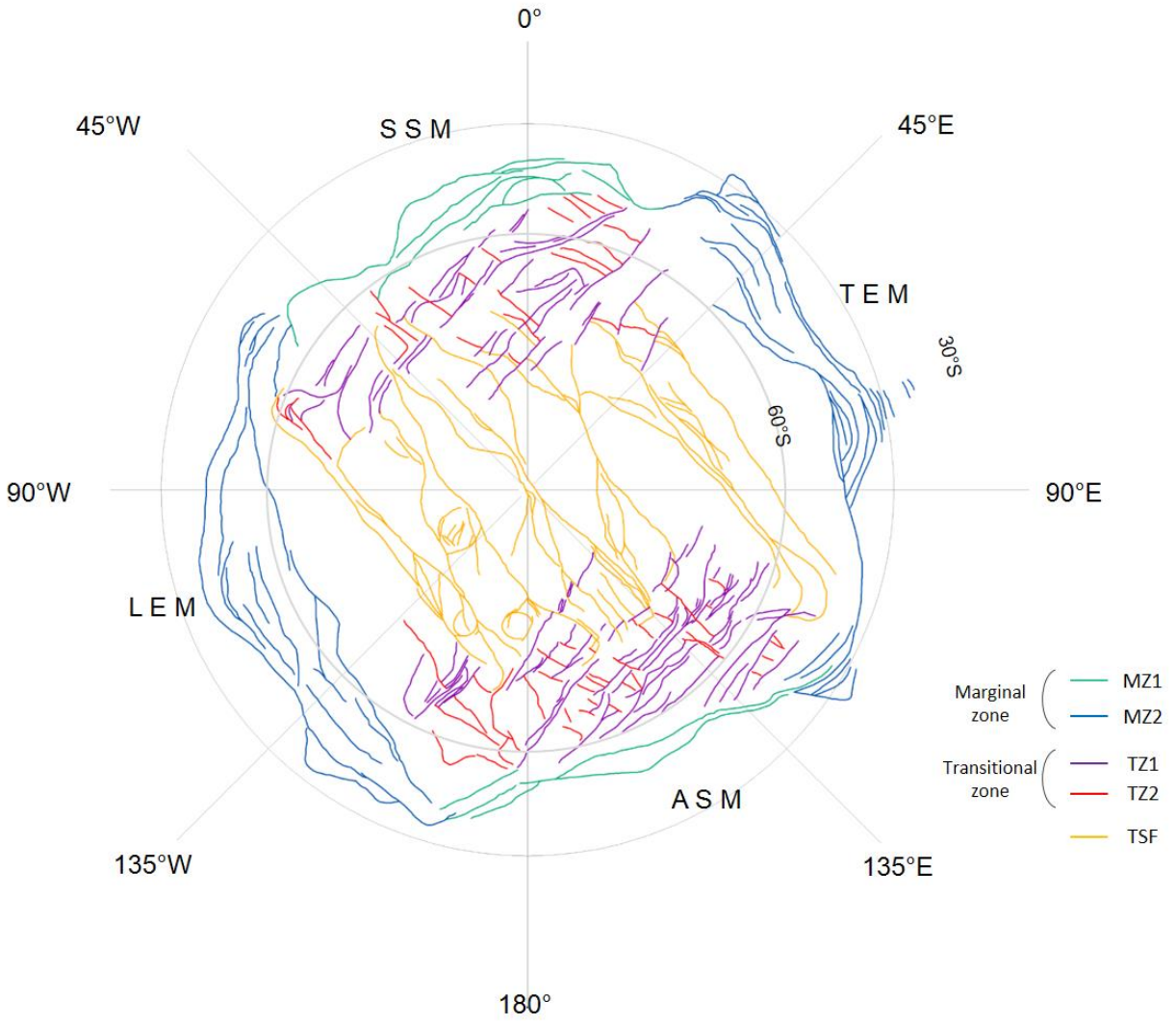

Figure 3. Enceladus SPT systems. The Marginal Zone systems are MZ1 represented in green color, and MZ2 in blue color. The Transitional Zone systems are TZ1 in purple color, and the TZ2 in red color. The TSF system is illustrated in orange color.

3.2 Azimuthal analysis

A spatial polymodal procedure of Gaussian best fit was performed for the azimuthal analysis of the identified linear structures. Independent azimuthal groups are represented by a family of Gaussian curves (e.g. Cianfarra & Salvini, 2016a; Maggi et al., 2015; Rossi et al., 2018; Wise et al., 1985).

We computed the azimuth of each structure, digitized as polyline, with respect to a reference "false North", defined as a line parallel to the SSM edge. Their azimuth was defined as the orientation of the element that connects the two polyline vertices with the minimum length (according to the

procedure used in Rossi et al., 2018). To characterize the orientations of these elements, the azimuthal analysis was performed by means of frequency and cumulative length. This allowed to recognize a total of five azimuthal systems in the SPT (Fig. 4).

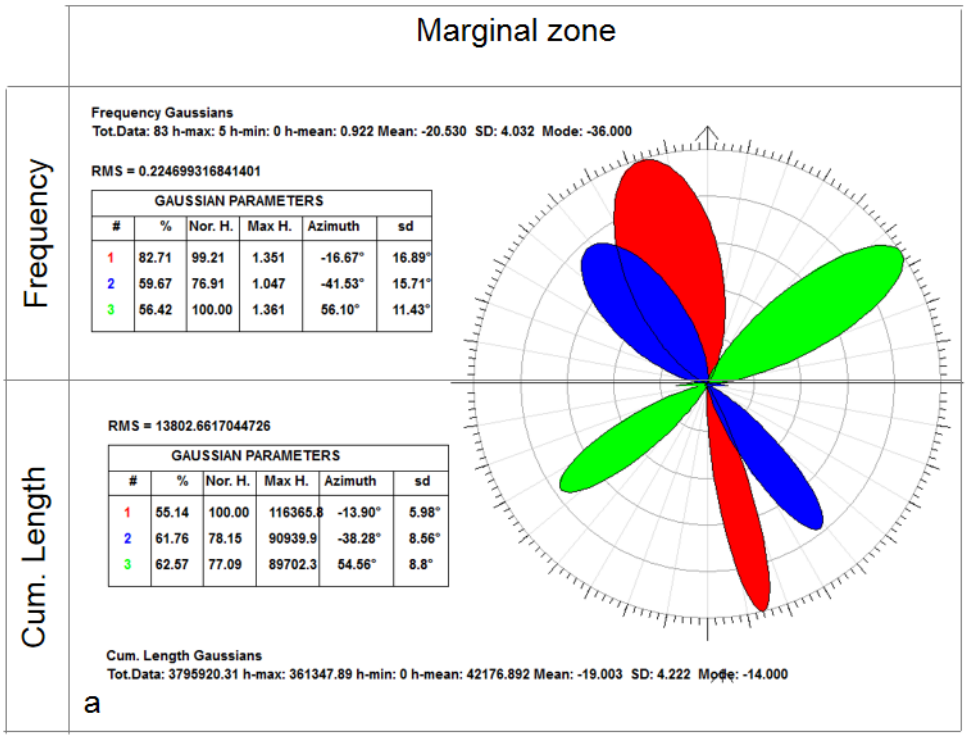

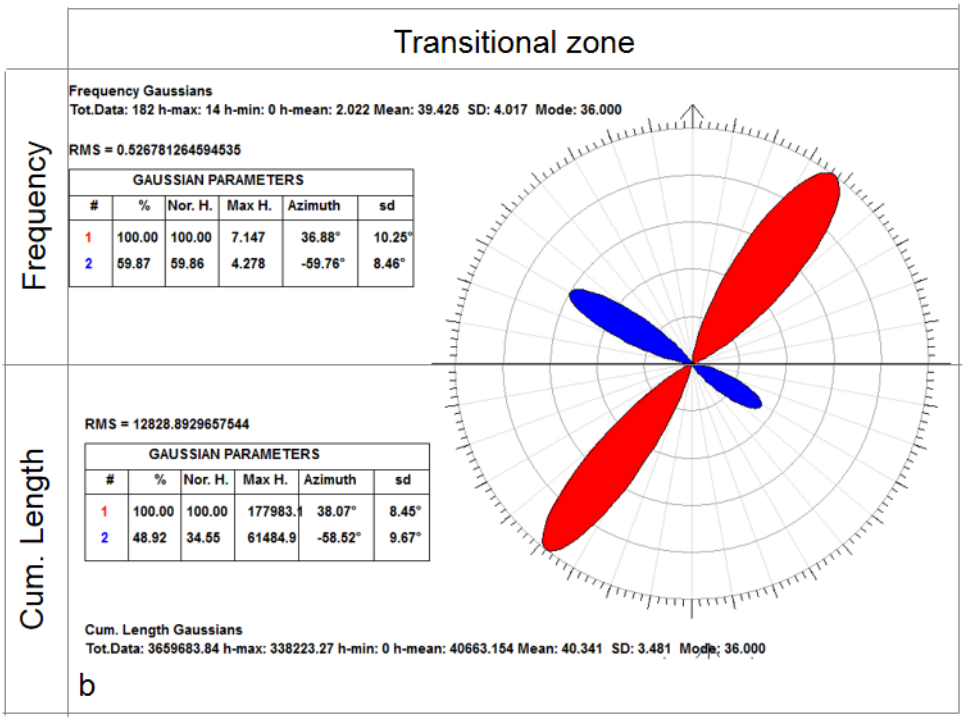

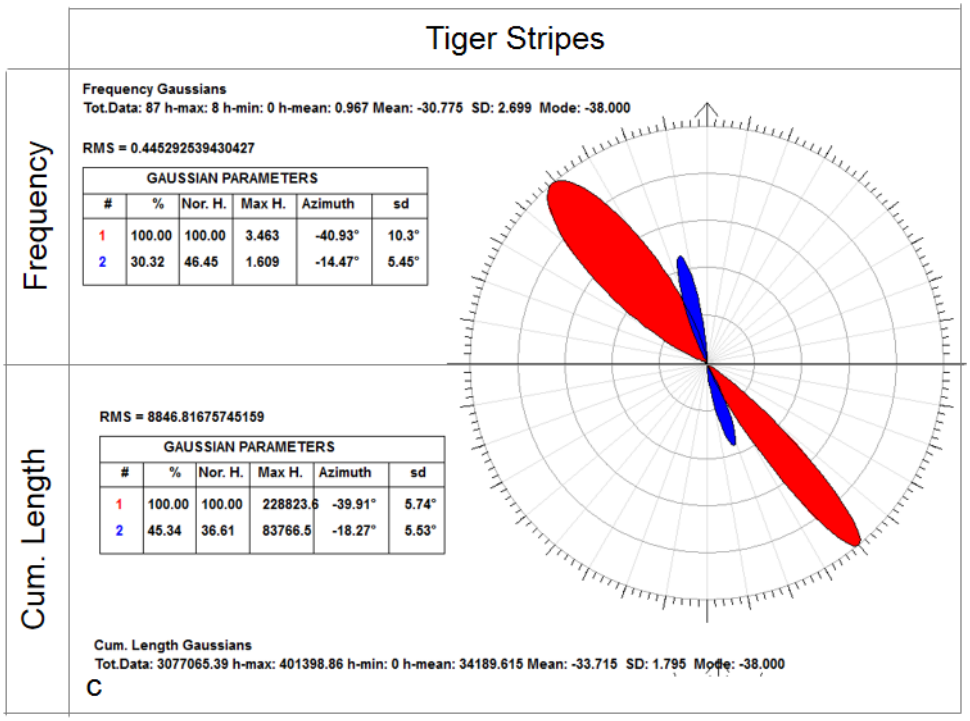

Figure 4. Azimuthal analysis of the recognized SPT systems. The wind-rose diagrams are subdivided into two semicircles, which show the analysis by frequency (the uppermost diagram) and the analysis by cumulative length (the lowermost diagram). Azimuthal analysis of a) the Marginal zone, b) the transitional zone, and c) the TSF structural unit. The Gaussian Parameters are reported: the number of Gaussian peaks (#), the percentage of occurrence (%), the Normalized Height (NorH), the Maximum height (MaxH), the azimuth, and the standard deviation (sd).

The results of the azimuthal analyses by frequency (upper part of the rose diagram) and by cumulative length (lower part of the rose diagram) are presented in Fig. 4. These results show that the marginal and transitional zones are characterized by two azimuthal systems each, while the TSF unit presents a single system.

The marginal zone is composed of a total of 83 elements. The azimuthal analysis (Fig. 4a) shows three main Gaussian peaks in this unit. These show well-defined preferential orientations: NW-SE, characterized by two peaks at N14°/17°W and N38°/41°W, and NE-SW, characterized by a peak at N55°/56°E. These main trends identify two main systems of the marginal zone with a symmetrical spatial distribution. The NE-SW system occurs within the ASM and SSM and is called Marginal Zone 1 (MZ1, green in Fig. 3), and the NW-SE system occurs within the LEM and TEM and is called Marginal Zone 2 (MZ2, blue in Fig. 3). The two peaks of the NW-SE system identified a single

system with large standard deviation, rather than two conjugate systems since the 24° angle between the peaks is small to consider this hypothesis.

The analyses of the transitional zone include a total of 183 elements. Two preferential Gaussian peaks characterize this unit (Figs. 3, 4b). They are nearly orthogonal and trend N37°/38°E and N58°/60°W. These systems are called Transitional Zone 1 (TZ1, purple in Fig. 3) and Transitional Zone 2 (TZ2, red in Fig. 3), respectively. These have similar spatial distribution and are more densely populated near the NE and SW internal angles of the marginal zone (the angles between the TEM and the SSM, and the LEM and the ASM, respectively). The analysis by cumulative length shows that TZ1 presents longer structures than TZ2.

A total of 88 elements were identified and analysed within the TSF zone. They define a fifth system that trend N39°/40°W (orange in Figs. 3, 4c). A secondary, minor Gaussian peak trending N15°/18°W may be attributed to the spatial variability of this system.

3.3 Length/Spacing analysis

The Length/Spacing ratio (L/S) is a non-dimensional parameter that characterizes the fracture intensity independent from any scale of observation (Cianfarra & Salvini 2016a; Rossi et al., 2018; Salvini, 2013). The measured value of this parameter refers to the length of the structures (L), and the Spacing (S) between two lines that approximate two adjacent and nearly parallel structures from the same system. This ratio quantitatively follows the fracture infilling induced by tectonic stresses (Bai & Pollard, 2000a, 2000b; Lachenbruch, 1961; Salvini, 2013) and in turn related to the applied stresses (Rossi et al., 2018; Salvini, 2013). Infilling mechanism relates to the enucleation of new fracture in between a pair of existing fractures. The formation of the new fracture halves the distance/spacing between the adjacent fractures and doubles the total fracture number. In this study it was measured to infer the morphological pattern observed in various tectonic regimes (Fossen, 2010). Indeed, by taking into account slightly variation of the thickness of the brittle ice layer, the morphological

geometries of the extensional tectonics differ from the compressional ones (Fossen, 2010; Woodward et al., 1989). The latter are supposed to provide a closer periodicity of the morphotectonic structures for the derived shortening as opposed to the activity of normal faults resulted from extension (Fossen, 2010). In this way, at the same stress regime, closely spaced structures (relatively high L/S) are often observed in compressional regimes and vice-versa (Woodward et al., 1989).

The data were collected within a length range, and the values were normalized with the adimensional ratio Length/Spacing (Rossi et al., 2018). We computed the L/S frequency histograms of L/S values of the SPT structures, and we identify the mean values for each system.

The TZ1 and TZ2 systems provided the best results, since their mean values provided a significative difference within the same structural unit. They are equally spatially distributed, and their analyses show two relatively different contexts. In this way, the systems of the transitional zone provided comparable values (Fig. 5a, b). The TZ1 system shows L/S mean value of 9.9 (Fig. 5a), higher than the TZ2 L/S mean value of 3.5 (Fig. 5b).

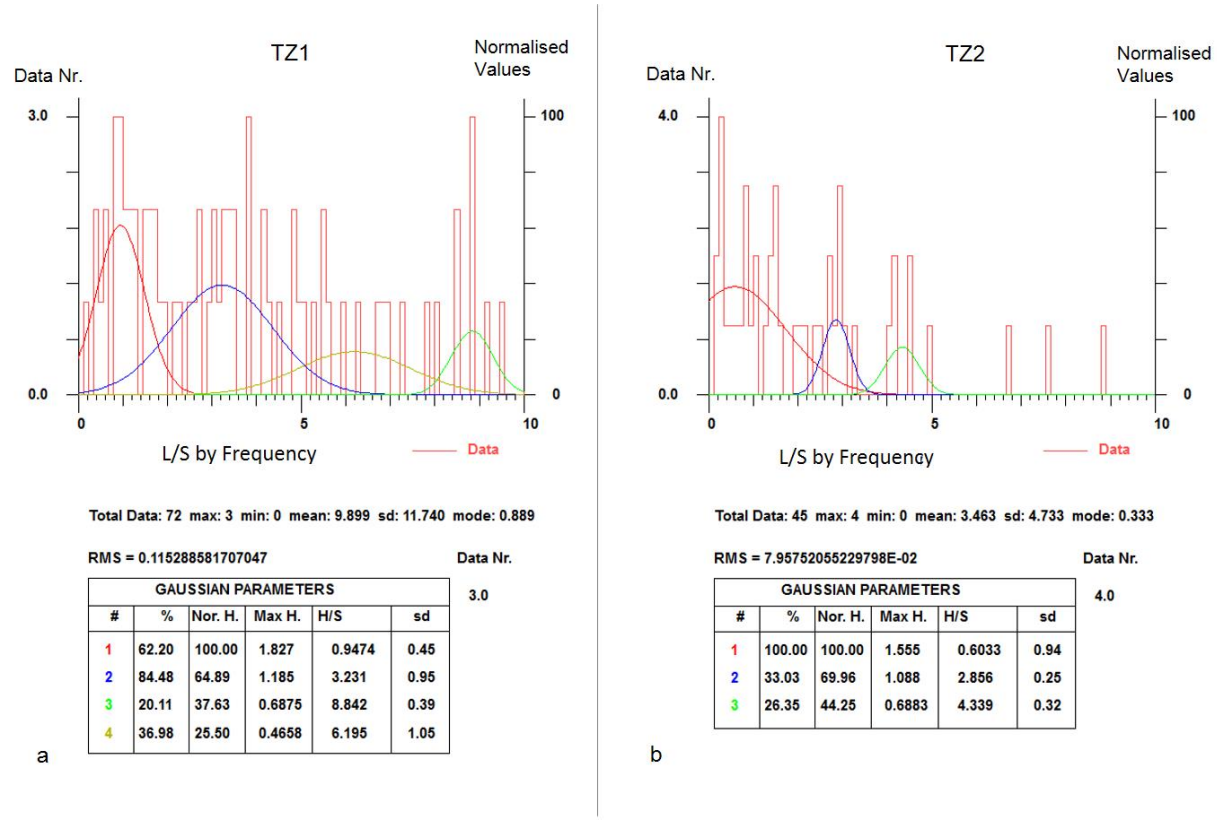

Figure 5. Transitional Zone Length/Spacing analysis. a) TZ1 L/S analysis; b) TZ2 L/S analysis.

3.4 Lineament domain analysis

The identification of SPT structure systems was integrated with the lineament domain analysis (Wise et al., 1985) to elucidate the tectonic and geodynamic setting of the SPT region. Lineaments result from alignments of tonal and morphological features in the topography (e.g. series of valleys and reliefs), enhanced by the low angle lighting. They are influenced by preferential erosion directions related to deformations induced by upper crustal stresses/kinematic conditions (Cianfarra & Salvini, 2014, 2015; Rossi et al., 2018; Wise, 1982; Wise et al., 1985). They are spatially distributed within a well-defined area, and cluster around preferential orientations to form lineament domains that are parallel to the maximum horizontal stress (Shmax) and perpendicular to the minimum horizontal stress (Shmin) (Pinheiro et al.,2019; Wise et al., 1985). Lineament domains can be used to infer the crustal stresses and kinematics of the planetary upper crust at the regional scale (Cianfarra & Salvini, 2014, 2016b; Lucianetti et al., 2017; Pinheiro et al., 2019; Wise, 1982; Wise et al., 1985).

We performed an automatic detection of the SPT lineaments on the base mosaic using the SID software (Salvini, 1999) that performs a systematic search for all possible straight segments in a discrete image of pixel alignments according to a set of parameters that describes the shape of the lineaments to be detected. They are the min/max length of the detectable lineaments, the density of pixels above a given threshold value, the pixel size and separation, that is the max distance between lineament segments (Rossi et al., 2018). A total of 2993 lineaments were identified within the SPT region (Fig. 6a). These were cumulated for the total data analysis to determine the regional tectonic setting. We performed a polymodal Gaussian fit by frequency and cumulative length to infer the azimuthal trends that define lineament domains in the SPT region. The two main peaks of each analysis (the red and blue peaks in Fig. 6) identified lineament domains, while the others are negligible for the analysis. The azimuthal analyses by frequency and by cumulative length share the main 3 Gaussian peaks: NW-SE (N39°/41°W), NE-SW (N44°/45°E), and E-W (N86°/90°E). The analysis by frequency recognizes a fourth, minor peak trending N-S (N2°W) (Fig. 6a).

Lineament azimuthal analyses were also performed within each separate structural unit. Both analyses for the marginal zone identify a total of two lineament domains trending NW-SE (N22°-25°W), and WNW-ESE (N80°-82°W) (Fig. 6b). the first domain provides a spatial distribution relatively higher than the second one (i.e. the peak is thinner), and is characterized by longer lineaments. The analyses of the lineaments recognized within the transitional zone provide a total of two lineament domains. These trend NE-SW (N30°-31°E) and NW-SE (N39°-45°W; Fig. 6c).

The NE-SW and NW-SE lineament domains of the transitional zone are similar to the azimuthal trends of the TZ1 and TZ2 analyses (Fig. 4b), and provide higher standard deviation (sd). Within the TSF, a lineament domain with peak at N10°/8°W (Fig. 6d).

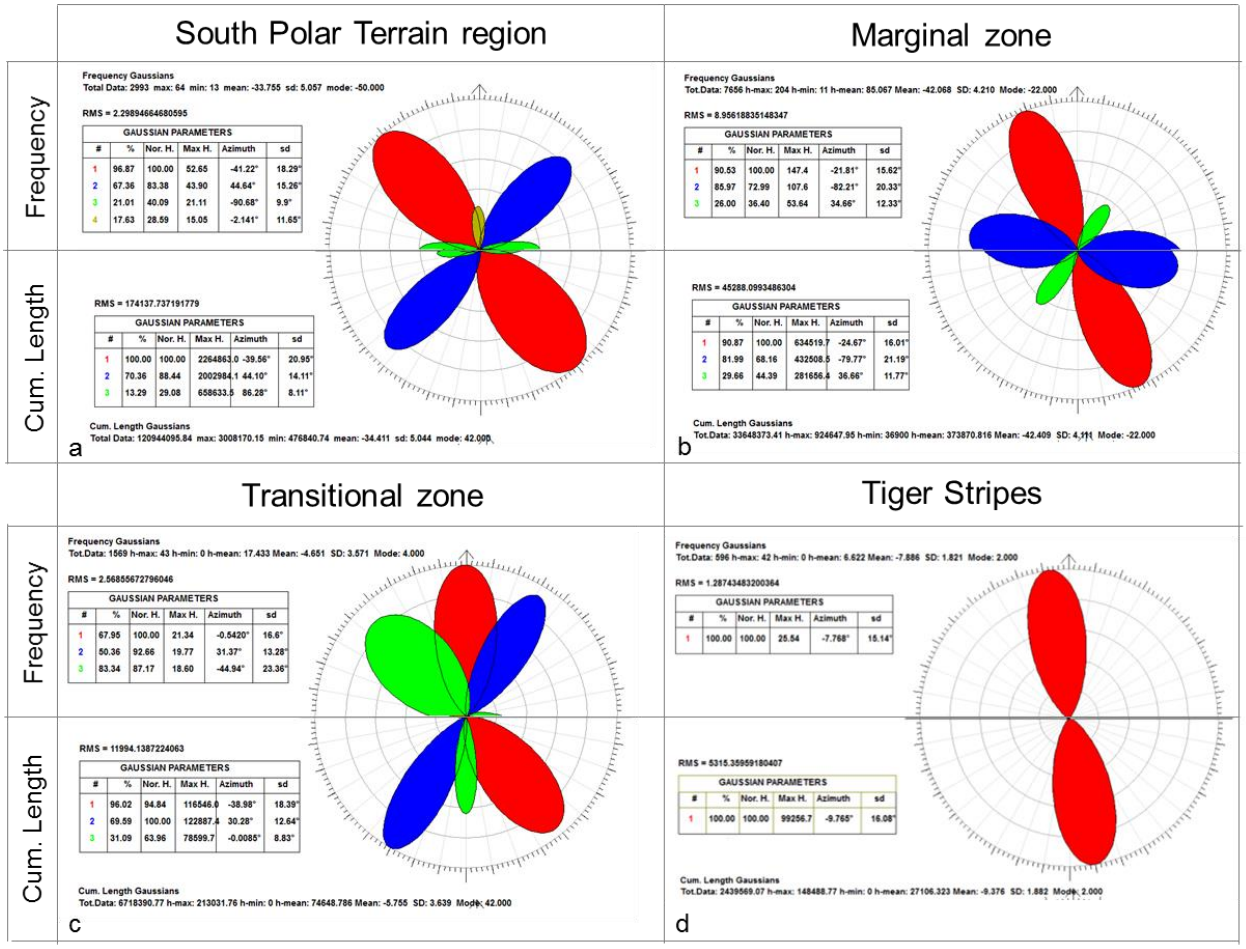

Figure 6. Azimuthal analysis of the lineament identified in the SPT systems. The wind-rose diagrams are subdivided into two semicircles, which show the analysis by frequency (the uppermost diagram) and the analysis by cumulative length (the lowermost diagram). Analysis of the a) SPT region, b) Marginal Zone, c) transitional Zone, d) TSF. The Gaussian Parameters are reported in Fig. 4.

3.5 Image processing

The base mosaic includes ISS (Wide and Narrow Angle Cameras) single band images (greyscale) whose pixel DNs relate to the energy reflected by the surface towards the sensor in the 0.35-1.10 □m interval (Knowles, 2016). The texture (i.e. the spatial variation of tones in an image; Fern & Warner, 2002) of the mosaic image is characterized by regions with characteristic and nearly homogeneous periodicity of grey tones (Fig. 7). This periodicity relates to the different tectonic/morphologic/compositional history of each region. Namely, extensional tectonics tends to generate sets of brittle deformation structures (e.g., faults, extensional fractures, lineaments) that, with the persisting of the extension tectonics through time, tends to step away from each other,

resulting in the increasing of the wavelength of the texture. On the other hand, in compressional regimes, the same elements tend to get closer to each other as the effect of the general shortening associated to the persistence of the deformation. In this way, a relatively shorter texture wavelengths (i.e. higher periodicity) may indicate the presence of sectors affected by compressional regimes, and longer texture wavelengths may relate to sectors that have been subjected to extension.

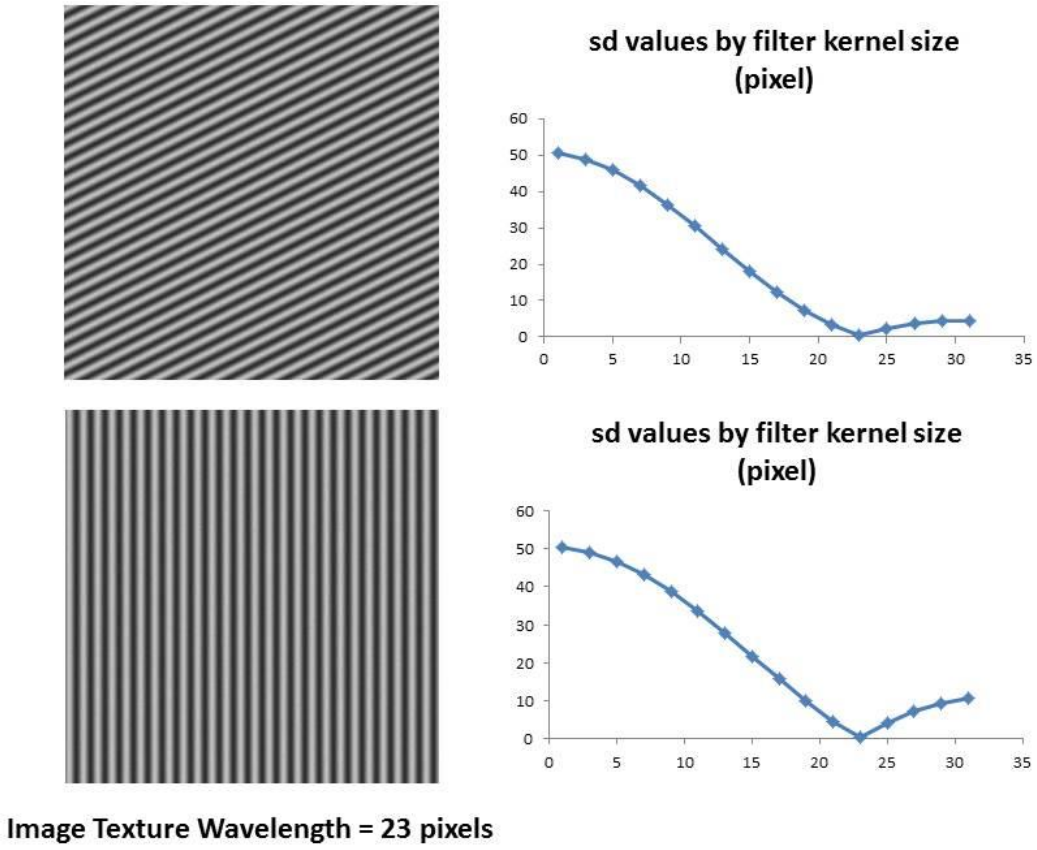

Figure 7. Example of standard deviation analysis for various kernel on a periodic textured image.

We prepared subsets for key areas of the SPT to find the optimal filtering kernels to characterize the regions with extensional or compressional tectonics. According to this procedure, the image texture was analysed by comparing a series of convolution low-pass filtering, to identify the characteristic texture wavelength in the SPT. The presence of a characteristic wavelength was identified by the comparison of the standard deviation of the images filtered with increasing kernel dimensions. The

drop in the sd value reveals the presence of a texture wavelength corresponding to the size of the kernel used in that filter. An example is reported in Fig. 7, where the results of this processing applied to synthetic images with a 23-pixel texture wavelength added to a (sub-ordered) random scattering (10%) are presented. The presence of the texture wavelength corresponds to the first minimum value in the sd at the corresponding filter kernel having the same dimension of the texture wavelength. This process was applied to key subsets of the SPT, where extensional or compressional regimes are expected. A series of in-house prepared routines to identify the optimal filter kernels and the characteristic texture wavelengths for these areas were performed. They repeated the filtering until the maximum kernel 59 by 59. Results show that the key subset corresponding to extensional regimes is characterized by a minimum of the sd value at a low-pass 51 by 51 kernel filtered image, and a similar lowering is observed on the 23 by 23 kernel filtered image in the key area corresponding to compressional regime.

The three filtered images of the SPT region were combined into RGB bands to obtain a synthetic image. The 51 by 51 kernel filtered image was set in the R band, the 23x23 in the G band, and the 51 by 51 sd in the B band. The produced classified image was then converted to HSL to add the reference morphology (i.e. the original image) in the L band. The final output image was obtained by re-conversion to RGB. This is shown in Fig. 8 where the SPT region is characterized by high- (blue color) and low- (yellow color) frequency zones, and intermediate zones (cyan and magenta colors). The NE (SSM-TEM angle) and SW (ASM-LEM angle) internal angles are characterized by a high frequency pixel-texture, and the NW (SSM-LEM angle) and SE (ASM-TEM angle) internal angles present low frequency pixel-texture. These results are indicative of different morphological periodicity (structural trend) within the SPT region.

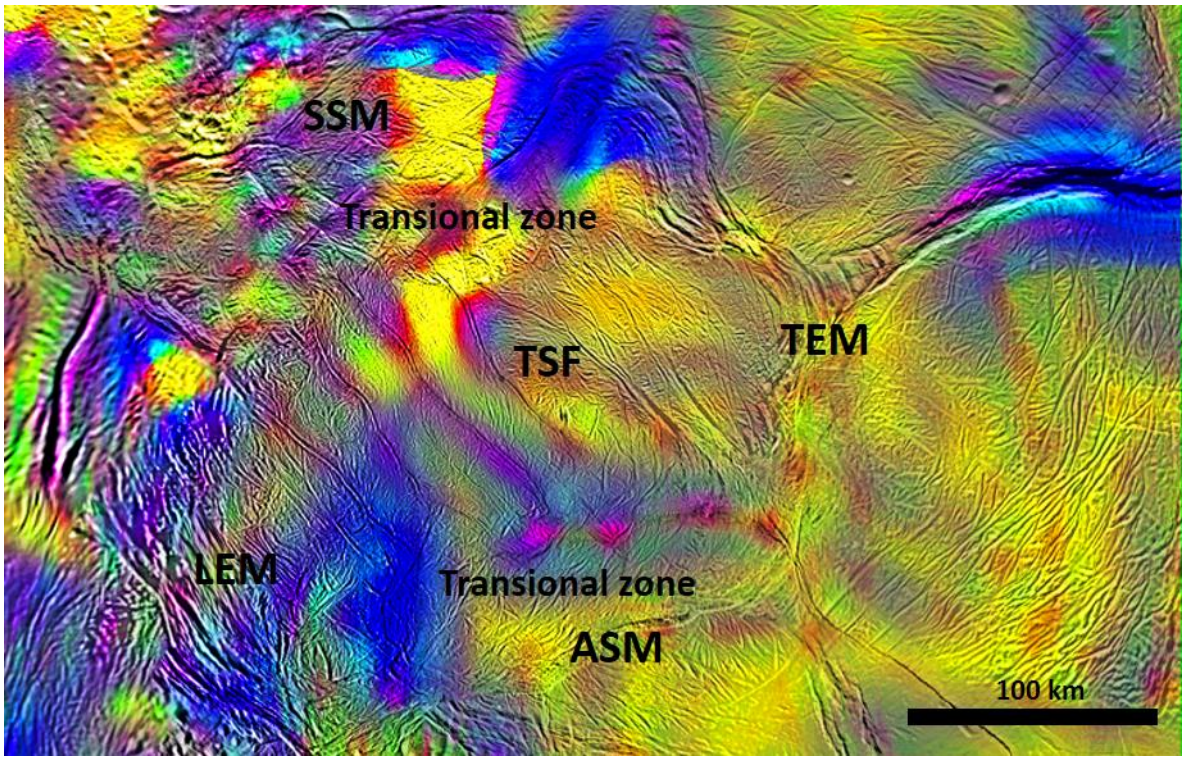

Figure 8. Final converted Red Green Blue color (RGB) synthetic image with reference morphology. The blue color refers to high-frequency, compressional structures; the yellow color refers to low-frequency, extensional structures; cyan and magenta colors relate to intermediate regimes (transpression/transtension).

4. Discussion

The SPT region of Enceladus is comprised of three main geo-structural units, i.e. the marginal zone, the transitional zone and the tiger-stripe zone, all characterized by the presence of brittle deformation. Structural mapping followed by quantitative analyses of the azimuthal and spatial distribution of the recognized structures allowed the identification of five systems in the structural units. These are MZ1 and MZ2 within the marginal zone, TZ1 and TZ2 within the transitional zone, and TSF (Fig. 3). The lineament domain analysis allowed to infer the stress field responsible of the system formation to propose tectonic model of the studied area. The result (Fig. 6a) shows two main peaks approximately at 90°. These are the NW-SE peak and the NE-SW peak that are both parallel to the maximum horizontal ($\sigma1$) and minimum horizontal ($\sigma3$ or $\sigma2$) crustal stress and represent two defined stress regimes induced by right- (the NW-SE) and left-lateral (the NE-SW) kinematics.

Obtained results show that the TSF cut and offset with sinistral displacement the other structures and the ancient tiger stripes (Patthoff & Kattenhorn, 2011) by left-lateral strike-slip. Their horsetail geometry termination provides a S-shape that follows regional right-lateral kinematics along the SSM and the ASM (as also observed by Yin & Pappalardo, 2015). The N10°/8°W trend of the lineament domain within the TSF area is compatible with the regional right-lateral shear (Fig. 6d). On the other hand, the left-lateral TSF kinematics is responsible of the NE-SW lineament domain recognized in the analysis of the SPT region (Fig. 6a).

The lineament domains within the transitional zone characterize well-defined tectonic regimes with similar significance. The nearly orthogonal NE-SW and NW-SE lineament domains (N30°/32°E and N39°/45°W, respectively, Fig. 6c) provide similar trend to the TZ1 and the TZ2 systems (Fig. 4b). These are associated to dynamic related to stress fields, and result from relative movement directions (Rossi et al., 2018). The difference in lineament domains sd shows that the NW-SE lineaments are more scattered than the NE-SW ones (Fig. 6c). This difference in spatial distribution is confirmed by the TZ1 and TZ2 L/S values (Fig. 5). As mentioned, closely spaced structures are often observed in compressional regimes (thrust faults, imbricate geometries, folds) where horizontal shortening occurs and in turn the spacing among structures decreases (Bai & Pollard, 2000a, 2000b; Fossen, 2010; Lachenbruch, 1961; Lianchong et al., 2014; Woodward et al., 1989). In this way the TZ1 and TZ2 systems characterize stress-related structures associable with dip-slip tectonics. The higher TZ1 L/S value is consistent with compressional tectonics, while the smaller TZ2 L/S value is consistent with extensional tectonics. The lineament domain setting of the transitional zone thus possibly represents the subsidiary tectonic regimes associated to the regional right-lateral strike-slip motion of the SSM and the ASM. The regional right-lateral kinematics produces within the SPT compressional structures with trend NE-SW, i.e. the TZ1, and NW-SE extensional structures, i.e. the TZ2.

In this way, the regional maximum and minimum horizontal (Shmax and Shmin) stresses are oriented NW-SE and NE-SW, respectively.

The marginal zone shows specular similarities. The systems of the LEM and the TEM are more sinuous than those of the SSM and the ASM and suggest a variability of tectonic regimes within the marginal zone. The lineament domains within the marginal zone (Fig. 6b) are consistent with the regional right-lateral strike-slip along the SSM and the ASM.

The image processing results show that various morphological periodicities/trends occur within the SPT. Fig. 8 allows to recognize clusters of relatively higher- and lower-frequency pixel-texture that in turn identify long and short periodicity of the morphology, respectively. These texture clusters are enhanced in the internal angles of the marginal zone (Fig. 8). The NE (between the SSM and the TEM) and SW (between the ASM and the LEM) angles show shorter periodicity than the NW (between the SSM and the LEM) and SE (between the SSM and the LEM) ones. The compressional shortening is characterized by closely spaced structures (Fossen, 2010). Conversely, extensional regimes are characterized by a long periodicity of the structures (i.e. high spacing between the structures). This means that the internal angles of the marginal zone show symmetrical contraposition of the style of deformation. Compression occurs within the NE and SW angles, and extension within the NW and SE angles.

The TSF form a mean angle of 75° with the SSM and the ASM edges that represent the boundaries of the right-lateral strike-slip corridor. In particular, it is assumed that at the beginning the internal structure, i.e. the TSF, developed at about 45° with respect to the SSM and the ASM. According to Cianfarra & Salvini (2015) the setting of pure strike-slip regime is supposed to form internal structures at 45° with the shear zone boundaries. This angle is supposed to increase in transpressional regimes and decrease in extensional ones. In this way, the current value of 75° indicates an angle increasing that will lead to the maximum angle of 90° (Cianfarra & Salvini, 2015). This suggests that the TSF performed a CW rotation of about 30° (from 45° to 75°). The structures interpreted as ancient Tiger Stripes (Patthoff & Kattenhorn, 2011) form an angle of approximately 40° between the TSF and provide an internal angle with the SSM and the ASM of approximately 115°. These ancient Tiger

Stripes could be originally formed as the present-day TSF. They could be formed at 45° and when they reached the maximum internal angle (90°) became relict Tiger Stripes and followed passively the CW rotation with the development of the present-day TSF. This might explain the angle exceeding 90° of the ancient TSF. The 30° rotation of the TSF induced a sinistral displacement of the ancient TSF of approximately 23 km. In a predictive way and by assuming a constant TSF rotation, we can infer that the offset of the ancient TSF would be about 70 km, when the present-day TSF rotation should stop, by reaching the internal angle of 90°.

An alternative hypothesis may explain the origin of the SPT structures. According to Cianfarra and Salvini (2015), the increasing of the internal angle results from a transpressional regime within the SPT. The relation between the variation of the internal angle and the percentage of the extensional/compressional component shows the suggested amount of the stress field (Rossi et al., 2018). In this way, the measured angle of 75° would indicate 55% of compressional component. The presence of the folded funiscular plains (Barr & Preuss, 2010; Nahm & Kattenohrn, 2015; Spencer & Nimmo, 2013) may confirm the prevalence of compressional component in the blocks delimited by the TSF. The texture clusters in Fig. 8 within these blocks show compressional and extensional zones. This condition might represent the transition of strike-slip motion from transpression to transtension.

We assume that both processes coexist, i.e. rotation and transpression, and in the following we suggest a tectonic model that is consistent with the derived kinematics.

4.1 Block rotation model for the South Polar Terrain

The obtained results allow to interpret the tectonics of the SPT in the framework of a block rotation model (McKenzie & Jackson, 1986). Fig. 9 shows the proposed model where a total of four blocks delimited by the TSF characterize the SPT region. The left-lateral kinematics, with transpressional component (55%), between the TSF induces CW rotation of the blocks. The rotation of the blocks

generates symmetrical tectonic regimes at opposite vertices of the marginal zone: compression occur within the NE (TEM-SSM angle) and SW (LEM-ASM angle) internal angles, while extension occurs within the NW (LEM-SSM angle) and SE (TEM-ASM angle) internal angles. The regional kinematics coupled with the block rotation is responsible for the formation of the TZ1 and TZ2 systems. At the regional scale right-lateral strike-slip characterizes the SSM and the ASM.

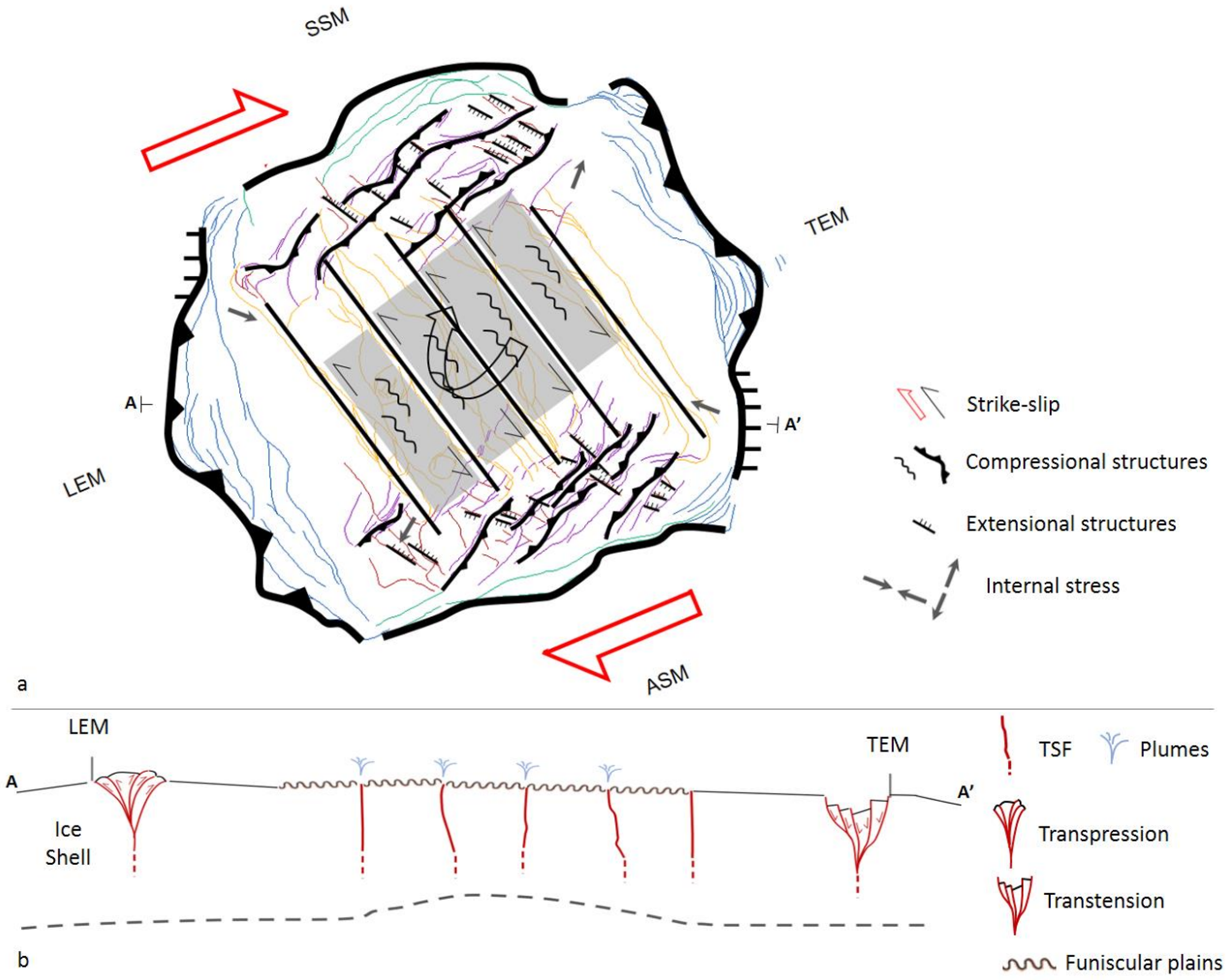

Figure 9. Block rotation tectonic model. a) Map view. The TSF are left-lateral strike-slip faults that delimit four blocks and rotate CW. The transitional zone systems TZ1 and TZ2 represent compression and extension, respectively. The marginal zone MZ1 represent right-lateral strike-slip, and the MZ2 present symmetrical and opposite transpressional and transtensional regime. A and A' represent the location of the b) cross-section view. The TSF are nearly vertical strike-slip structures, where plumes depart. The LEM and TEM marginal zone edges are under transpression and transtension. The ice shell thins under the TSF to reach about 5 km of thickness (dashed gray line).

We propose the evolutionary kinematic model, shown in Fig. 10. The SPT region is characterized by rigid blocks (Fig. 10a) delimited at the SSM and at the ASM by right-lateral strike-slip structures (Fig. 10b). The kinematics produces internal deformation manifested by the formation of the TSF at about 45° that delimit four blocks (Fig. 10c). The SSM and ASM regional right-lateral strike-slip begin the rotation of the blocks of 45°+ ϕ (Fig. 10d). The rotation continues until reach the maximum angle of 90° (Fig. 10e). Through time, the protraction of the regional right-lateral strike-slip will form second-generation TSF at 45° (i.e. the current TSF; Fig. 10f). The rotation of the newly formed TSF cause the offset of the ancient TSF of 23 km at the present-day configuration (Fig. 10g). By taking into account a constant block rotation process, the future setting of the TSF will offset the ancient one of 70 km, when they end the rotation by reaching the maximum angle of 90° (Fig. 10h). This model can be repeated until the rotation ceases.

The proposed model is comparable with the model of Yin and Pappalardo (2015). Strong strike-slip kinematics affects the SPT region, where CW rotation occurs by the TSF left-lateral displacement. Conversely to the flow-like tectonics, our model relates to the SSM and ASM regional right-lateral strike-slip and the rotation of internal blocks.

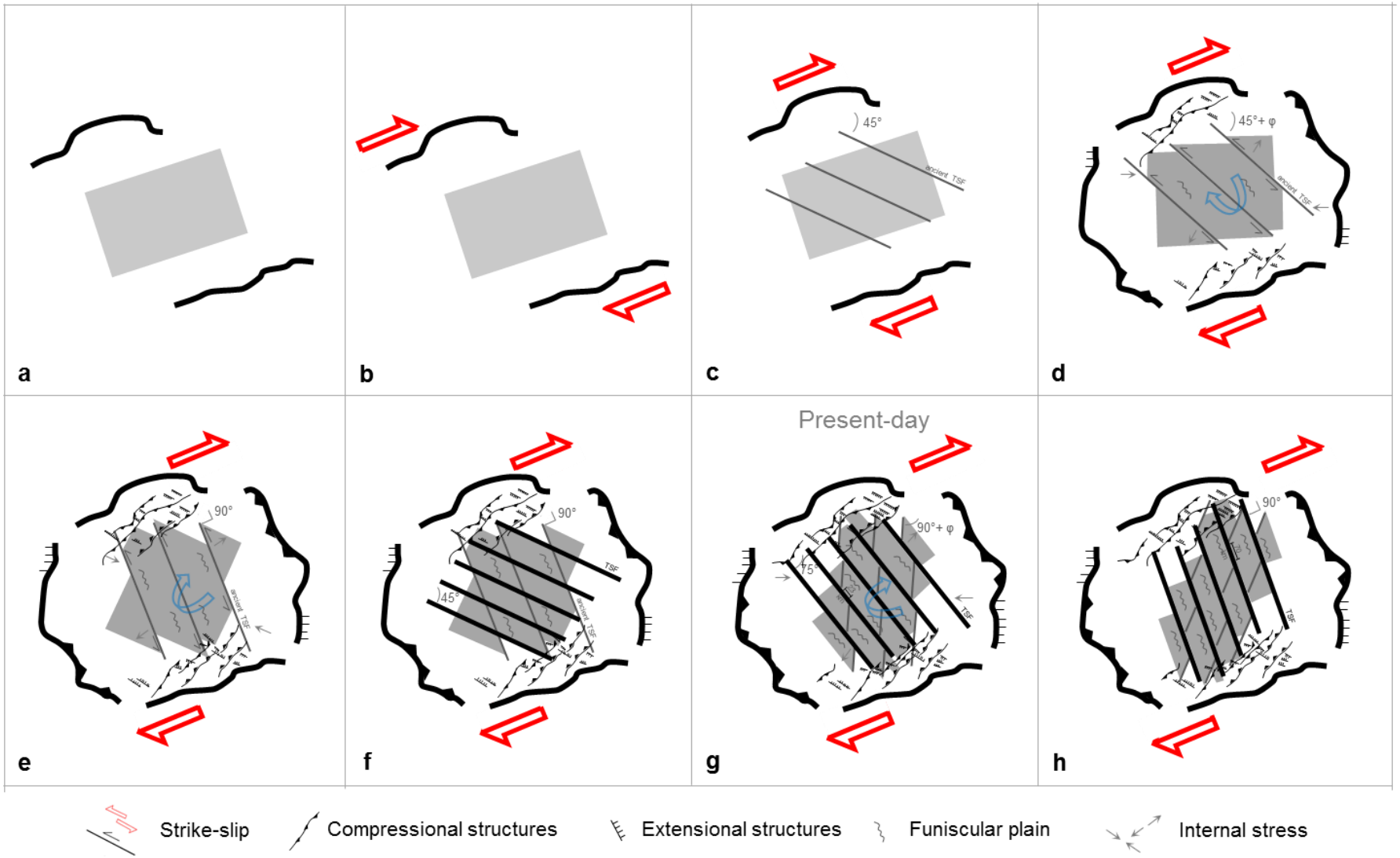

Figure 10. Evolutionary tectonic model of the SPT: a) the SPT is characterized by rigid blocks; b) development of the regional right-lateral kinematics along the SSM and ASM edges; c) development of the TSF at 45° with the SSM and ASM; d) the left-lateral kinematics of the TSF divides four blocks with a CW rotation of 45°+ ϕ, the TSF and the SSM and ASM strike-slip determine the development of the transitional zone structures (TZ1 and TZ2 systems), transpressional component within the blocks (development of the funiscular plains), and transpression and transtension develop along the Mz1 and MZ2 edges; e) end of the TSF CW rotation until 90°; f) new generation TSF form at 45°; g) the new generation TSF reach the present-day configuration of 75° by offsetting of 23 km the ancient TSF that exceed the 90°; h) through time the block rotation will lead the TSF until 90°, with the future offset of the ancient TSF of 70 km.

5. Conclusions

Enceladus South Polar Terrain presents complex pattern of fractures and faults in structural units. The performed analyses allow to identify and classify these structures into systems.

The results suggest that the SPT is mainly affected by dual strike-slip tectonic regime that in turn form subordinate and symmetric compressional and extensional zones. The activity of the SPT of Enceladus reveals block rotation tectonics. Regional right-lateral strike-slip structures enclose the left-lateral kinematics along the Tiger Stripes. These delimit rigid blocks that rotate CW and might ease plume eruptions. This tectonic setting defines a "kinematically balanced" region where the driving forces are enclosed within the SPT. The described kinematics could represent the effect of local plume sources as the hydrothermal activity produces in the subsurface ocean.

The block rotation tectonic model represents a key tool to understand the evolution from the past to the future setting of the SPT. At present the TSF leaded a block rotation of 30°, and through time this persistent kinematics will lead a future offset of the internal relict tiger stripes of about 47 km.

These results are significative for the future exploration of the satellite to identify preferential zones to better reach the subsurface ocean.

Acknowledgments

Funding for this project came from Roma Tre University (fellowship). This work has been completed as part of the PhD project of the first author. We thank the Laboratory of Geodynamics and Planetary Sciences of the University of Nantes for their kind hospitality.

3.2 Terrestrial analog of Enceladus

Antarctic glaciers present analogies also with the structures on the Enceladus icy surface.

Enceladus SPT shows a crustal thickness variation from approximately 10 km in the marginal zone to approximately 5 km in the tiger stripe unit (Le Gall et al., 2017). The curvilinear geometry of the MZ2 structures of the SPT marginal zone (Fig. 3 in section 3.1) relates to the compressional/extensional regimes and also to the SPT thickness variation.

Fig. 1 and 2 show the transverse crevasses formed at the steep slope of the bedrock beneath the glacier. These crevasses show analogy with the Enceladus MZ2 structures. They present similar curvilinear geometry formed by dip-slip regime. This type of crevasses often occurs at the head of the glacier where extending flow originates the glacier kinematics.

Fig. 3 shows V-shape marginal crevasses. These are formed by lateral compression that causes their opening and arcing up-flow. Their geometry is analogous to the Y-shaped structures of Enceladus SPT in the TEM area (Fig. 1, section 1). Fig. 8 in section 3.5, and supports a similar formation mechanism. In this figure, two texture frequency are reported in the main Y-shape structure. At the tip of the structure texture high-frequency (blue color) indicates compressional regime, and the low-frequency (yellow color) characterizes the opening of the structure.

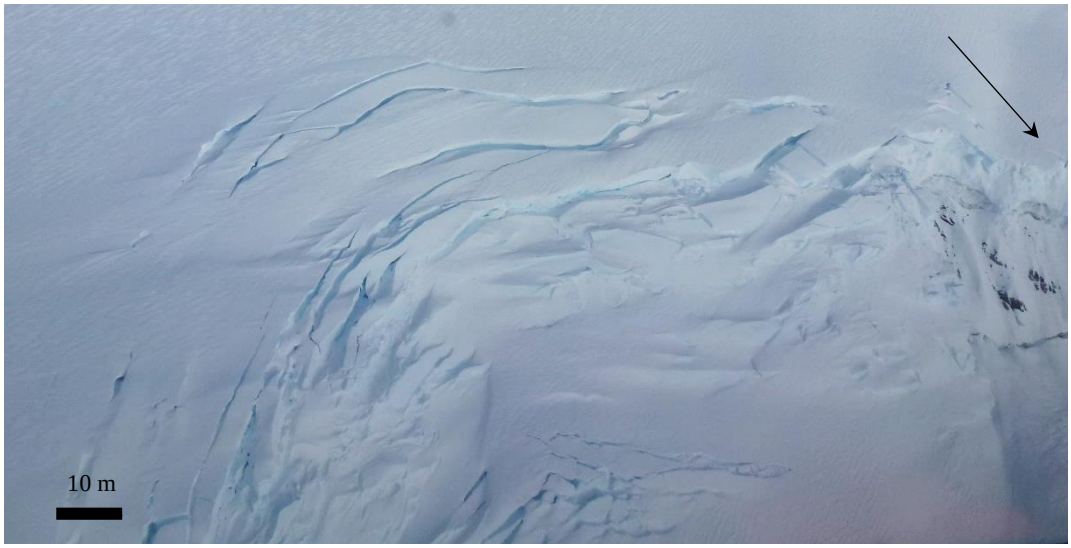

Fig. 1: Aerial view of transverse crevasses in the Rennick glacier, Antarctica. The black arrow shows the flow direction. PNRA XXXIV expedition.

Fig. 2: Aerial view of crevasses in the Rennick glacier, Antarctica. The black arrow shows the flow direction. PNRA XXXIV expedition.

Fig. 3: Aerial view of crevasses in the Rennick glacier, Antarctica. The black arrow shows the flow direction. PNRA XXXIV expedition.

CHAPTER 4

MARS NORTHERN ICE CAP

4.1 The Tectonic origin of Planum Boreum spiral troughs, Mars

Abstract

The spiral troughs of the North Polar Layered deposits on Mars are deep depressions that dissect the Planum Boreum ice cap. These are enigmatic structures whose puzzling origin is still under debate. Advanced hypotheses on their genesis and evolution range between erosional to structural/tectonic scenario. In this work, a double approach was followed to explore the structural/tectonic origin of the spiral troughs by means of Hybrid Cellular Automata (HCA) numerical modelling and of lineament domain analysis. The SHARAD profile data were used for the numerical modeling to replicate the ice internal layering architecture associated to the buried troughs in Gemina Lingula. Analysis of the lineament domains automatically detected on the ice surface from satellite images strengthened structural/tectonic interpretation on the origin and evolution of the spiral troughs. Similar, twofold approach was used for the study of a terrestrial analog identified in the Antarctic ice sheet. Obtained results and their comparison show that the troughs of Gemina Lingula result from the activity of low-angle normal faults with listric geometry. The proposed tectonic model refers to an extensional regime characterized by the presence of a deep detachment possibly connecting the troughs at depth. This represents an internal ductile layer placed at depth greater than 1000 m whose kinematics induces the troughs/faults deformation. The extensional tectonics developed in Planum Boreum is possibly related to the ice cap collapse that induces internal dynamics. Katabatic winds play a secondary role in the surface maintenance of troughs nearly orthogonal to their directions.

1. Introduction

Mariner 9 and Viking imagery revealed the peculiar geometries and features of Mars polar caps (Cutts, 1973; Soderblom et al., 1973; Smith and Holt, 2010). These are articulated into regional-scale structures spirally arranged, the spiral troughs that are object of open debate. The instrumentations of the Mars Express and Mars Reconnaissance Orbiter (MRO) missions provided subsurface observations of the ice cap interiors (Picardi et al., 2005; Seu et al., 2007; Plaut et al., 2007). The ground penetrating radars MARSIS (Mars Express) and SHARAD (MRO) acquired profiles that revealed the internal ice layering and the depth of the structures, including the spiral troughs that reach more than 1000 m of depth. These troughs are traditionally considered strictly related to

migration by wind transport, that shapes the surface by forming deposition/accumulation and erosion/ablation slopes (Cutts, 1973; Howard, 2000; Fisher, 2000; Tanaka et al., 2008; Smith and Holt, 2010, 2015; Massé et al., 2012; Herny et al., 2014; Smith et al., 2016; Bramson et al., 2019). Other hypotheses attribute the trough formation to structural factors caused by internal dynamics of the ice caps (Squyres, 1979; Weijermars, 1986; Budd et al., 1986; Clifford et al., 1987; Pellettier, 2004; Ng and Zuber, 2006; Zeng et al., 2007; Grima et al., 2011), similarly to the internal sliding and deformation that occur in the terrestrial glaciers (e.g. Chamberlin, 1936; Engeln, 1934; Hambrey and Muller, 1978; Weijermars, 1986; Jezek and Bentley, 1983; Clarke and Bentley, 1994; Lawson et al., 1994; Rott et al., 1998; Bennett et al., 2000; Das et al., 2008; Rignot et al., 2011; Phillips et al., 2013; Colgan et al., 2016; Maggi et al., 2016). Independently from their origin, the spiral troughs play a key role in the understanding of the martian ice cap evolution. They represent evidence of exogenous and/or endogenous processes that affect the polar cap.

In this paper, we investigate the troughs of Mars north pole that show similarities with extensional terrestrial structures. The trough setting revealed by the SHARAD profiles are compared with the Low-Angle Normal Faults (Wernicke, 1981; Scott and Lister, 1992; Fossen, 2010) with compatible listric shape (Walsh and Watterson, 1991; Fossen, 2010). These faults present curved surface, concave upwards as depicted by the spiral trough section in the depth profiles. Our study infers the presence of dynamic process within the northern ice cap that leads internal large-scale brittle deformation with the consequent trough formation. This is enabled by the presence of possible deep ductile/fluid detachment at depth (Clifford et al, 1987; Grima et al., 2011; Souček et al., 2015).

We investigated and modelled the trough tectonic scenario in comparison with similar structural setting found in the Cook Ice Shelf glaciers in Antarctica. The obtained results allow to propose a model for the structural origin and evolution of the spiral troughs of Mars north pole. In this way, the katabatic winds are considered as secondary factors that shape the troughs, initially formed by structural factors.

2. Mars North Pole

Planum Boreum is the ice plateau that forms the martian terrain of the north pole, together with the surrounding plains of Vastitas Borealis (Kreslavsky and Head, 2000; Tanaka et al., 2008; Fig. 1). It is composed of H_2O ice-Ih, with smaller percentage of dust and seasonal CO_2 frost (Tanaka and Kolb, 2001; Tanaka et al., 2008; Smith and Holt, 2010; Grima et al., 2011). It is incised by the Chasma Boreale valley (Howard, 2000; Tanaka et al., 2008) that represents a 450-km-long canyon and separates part of the plateau into Gemina Lingula, a lobate extension of the plateau from 310° to 10°E (Tanaka et al., 2008). The mean surface temperature of about 150 K (Lewis et al., 1999; Grima et al., 2011) experiences regional, diurnal and seasonal variations that give rise to katabatic winds (Howard, 2000; Spiga et al., 2011, 2018, Massé et al., 2012). These are drainage atmospheric winds that originate by higher-density air accelerated downsloping by gravity (Mahrt, 1982; Spiga, 2011). On Mars surface these are two to three times stronger than terrestrial katabatics (Blumsack et al.,1973; Howard, 2000; Spiga, 2011).

The ice cap surface shows complex physiography characterized by the spiral troughs, that represent regional scale, curvilinear features with arcuate undulations disposed in spiral pattern (Cutts et al., 1979; Budd et al., 1986; Tanaka et al., 2008; Fig. 1a). These are approximately 10 – 300 km long and encircle the north pole until they reach the margin of Planum Boreum (Tanaka et al., 2008; Smith and Holt, 2010). The troughs provide exposed layers on their equator-facing slopes, and no layering is observed in the pole-facing slopes (Soderblom et al., 1973; Howard, 1978; Squyres, 1979; Howard et al., 1982; Smith and Holt, 2010). Smaller linear topographic waves, also called shallow undulations, are superimposed on the upwind sides of the large spiral-shaped topographic waves of the Planum Boreum (Cutts et al., 1979; Herny et al., 2014; Smith and Holt, 2015). The structural setting of the polar cap is revealed by radar data.

Radar depth profiles reveal continuous ice reflectors that constitute the internal deposition of layers in about 2 km of thickness of the plateau (Soderblom et al. 1973; Squyres, 1979; Plaut et al., 2007; Seu et al., 2007; Phillips et al., 2008; Smith and Holt, 2010). These profiles record over 3 billion years of deposition and erosion of Planum Boreum, that covers an area of approximately 800,000 km^2 (Phillips et al., 2008). The North Polar Layered Deposits (NPLD; Blasius et al., 1982; Milkovich and Head, 2006; Tanaka et al., 2008) represent the result of periodical orbital variation of the planet. Radar data reveal a Basal Unit (BU) beneath the NPLD, with lower albedo and thicker layers than the overlying deposits (Edgett et al., 2003; Phillips et al., 2008). The radargrams show a series of deep features as buried craters (Putzig et al., 2018) and the subsurface profiles of the spiral troughs. These cut and offset the NPLD from the surface until more than 1000 m of depth with a gentle slope lower than 5° towards the margins (Dzurisin and Blasius, 1975; Cutts et al., 1979; Squyres, 1979). Buried troughs were found in radar profiles, and, in particular, in Gemina Lingula profiles (Smith et al., 2016). Spiral troughs are thought to be erosional features produced by eolian processes (Cutts, 1973; Howard, 2000; Fisher, 2000; Tanaka et al., 2008; Smith and Holt, 2010, 2015; Massé et al., 2012; Herny et al., 2014; Smith et al., 2016; Bramson et al., 2019). This hypothesis suggests that the trough development is influenced by the action of the katabatic winds that lead preferential erosion/ablation in the layered equator-facing slopes, accompanied by deposition/accumulation on the pole-facing slope due to solar ablation (Fisher, 2000; Smith and Holt, 2010). The spiral pattern is related to the katabatic wind deflection produced by the Coriolis effect (Cutts, 1973; Howard et al., 1982; Howard, 2000; Fisher, 2000; Fisher, 2002; Pelletier, 2004; Tanaka et al., 2008; Smith and Holt, 2010; Spiga et al., 2011; Massé et al., 2012; Herny et al., 2014; Spiga and Smith, 2018). According to this model, the buried troughs in Gemina Lingula formed by past eolian activity. On the other hand, these troughs could represent features formed in a different way, and possible present activity. Alternative formation hypotheses support the structural origin of the troughs (Squyres, 1979; Blasius et al., 1982; Budd et al., 1986; Pellettier, 2004; Ng and Zuber, 2006; Zeng et al., 2007, 2008) that are

dynamically induced by internal/basal melting flow (Weijermars, 1986; Clifford, 1987; Souček et al., 2015).

2.1 Antarctica analog

Planum Boreum represents the main example of extraterrestrial ice-sheet comparable to the Earth ones (Howard, 2000; Fisher, 2002; Grima et al., 2011). It shows similarities and differences in surface properties, morphology, katabatic wind regime with Antarctica, that represents very good terrestrial analog (Fig. 1b).

The Antarctic ice cap is composed by H_2O ice-Ih layers and reaches a maximum thickness of more than 4 km and covers an area of approximately 14 000 000 km^2 (Fretwell et al., 2013). The Antarctic plateau experiences temperature that reaches the minimum at 180 K (Fortuin et al., 1990) and is covered by a dense atmosphere that induces katabatic winds (Parish 1984, 1988; Parish and Bromwich, 1986). These contribute to shape the plateau surface by the production of landforms as dunes fields (Bromwich et al., 1990). Ablation and accumulation control and maintain the Antarctic surface mass balance (Fortuin et al., 1990; Frezzotti et al., 2004; Fisher, 2002).

Antarctica lacks spiral surficial features such as the troughs that characterize the surface of Planum Boreum. The snow megadunes (Frezzotti et al., 2002) present in the Antarctic surface are partially comparable with the polar troughs of Mars (Herny et al., 2014).

The Antarctic ice sheet with its outlet glaciers and ice streams present internal dynamics that induces ice flow, with local melting and brittle deformation (i.e. crevasses). Ice shelves and glaciers are deformed by fractures that reach up to 1000 m of depth and are visible from satellite imagery (Emetc et al., 2018).

The proposed analog is located in the glacier feeding the Cook ice shelf (152°59’E 68°59’S, Alberts, 1995; Fig. 1b). In this region the ice covers the bedrock with approximately 1200 m of thickness, and radar data show ice layering and buried structures with geometries comparable to those found in

Gemina Lingula. Their formation is interpreted as the effect of internal brittle deformation resulting from the internal dynamics and gravitational sliding typical of Earth glaciers.

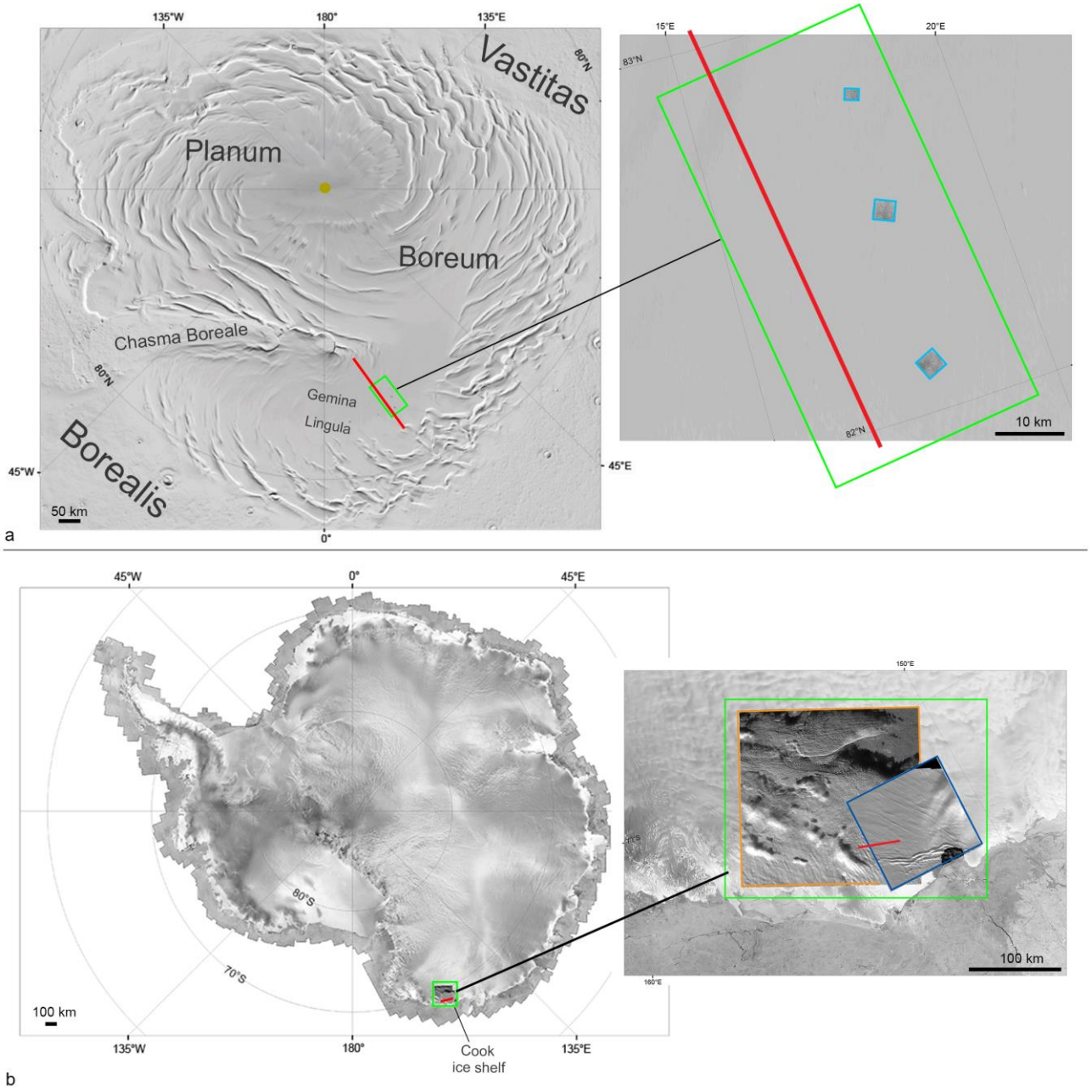

Fig. 1: Investigated areas. a) Mars north pole region, shaded relief surface from MOLA. The yellow circle shows the north pole location. The red line in Gemina Lingula trace the used SHARAD profile, the green square frames the location of the used MOC images (light blue squares). b) Antarctica analog. The red line in the Cook ice shelf glaciers represents the used HiCARS profile, the green square the location of the Landsat (orange square) and Sentinel (blue square) images.

3. Data

The depth data used for the Mars north pole investigation derive from the mission Mars Reconnaissance Orbiter (MRO) available in the dataset of the open-source JMARS software (Christensen et al, 2009). We investigated radargrams of the SHAllow RADar sounder (SHARAD) that operates at 20 MHz (Plaut et al., 2007; Seu et al., 2007b; Castaldo et al., 2017; Putzig et al., 2018). The SHARAD data were accurately selected to be compared with the terrestrial analogs. In this way, buried troughs were preferred for the modeling since these are easier comparable with Antarctica analog than the surface spiral troughs. The proposed approach in this work is valid for both the buried and the surficial troughs. The analysed profile S_0072540 in Gemina Lingula shows buried troughs at a depth of approximately 250 m (red line in Fig. 1a, Fig. 2a). This work considers dielectric permittivity $\varepsilon = 3.15$ for NPLD reflections as composed by nearly pure water ice and in turn a penetration depth of more than 1 km (Plaut et al., 2007; Seu et al., 2007; Grima et al., 2009; Putzig et al., 2018). Image data were used to investigate the surface lineaments related to the depth features. These data derive from the Mars Orbiter Camera (MOC) of the Mars Global Surveyor probe. We investigate the high-resolution images E01/00948, M01/2295, M01/05987, E02/00430 (1.6 m/pixel) acquired along the track of the used SHARAD profile (green square in Fig. 1b).

Antarctic analog data are the radar echo-strength profiles from the IceBridge High-Capability Radar Sounder (HiCARS, 60 MHz) dataset (ID: IR1HI1B, available in the IceBridge portal; Blankenship et al., 2017; red line in Fig. 1b, Fig. 3a). The satellite image data of the glacier that feeds the Cook ice shelf were selected from the Landsat-8 (ID: LC08_L1GT_075109_20190410_20190422_01; 30 m/pixel;) and Sentinel-2 (ID: T56DMJ_20190405T225339; 60 m/pixel) database (green square in Fig. 1b). The satellite imagery was freely downloaded from the USGS data archive (https://earthexplorer.usgs.gov/).

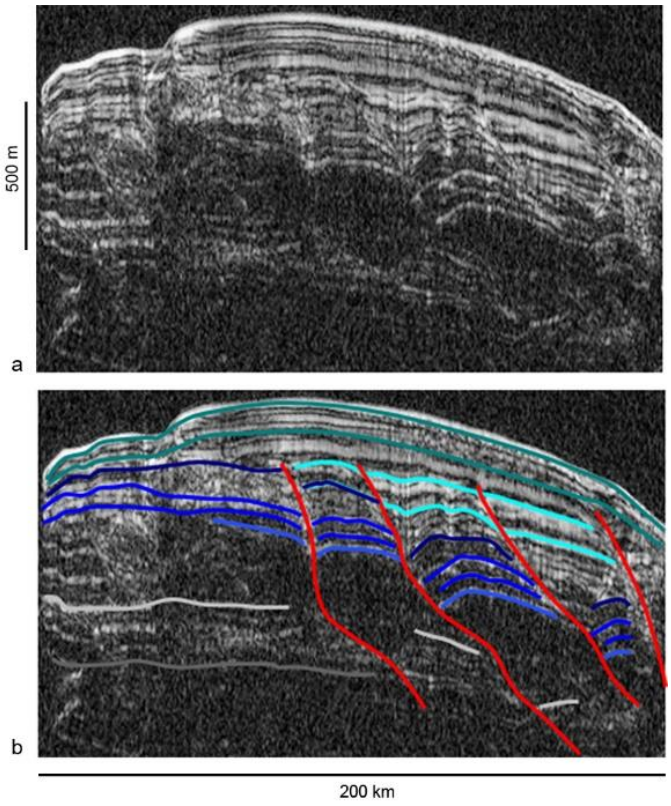

Fig. 2: a) SHARAD observation S_00725402 in Gemina Lingula (vertical exaggeration 90:1). b) SHARAD layer picking. The blue, light blue and green lines represent the top and bottom of the main ice reflectors, and the red lines the troughs/faults.

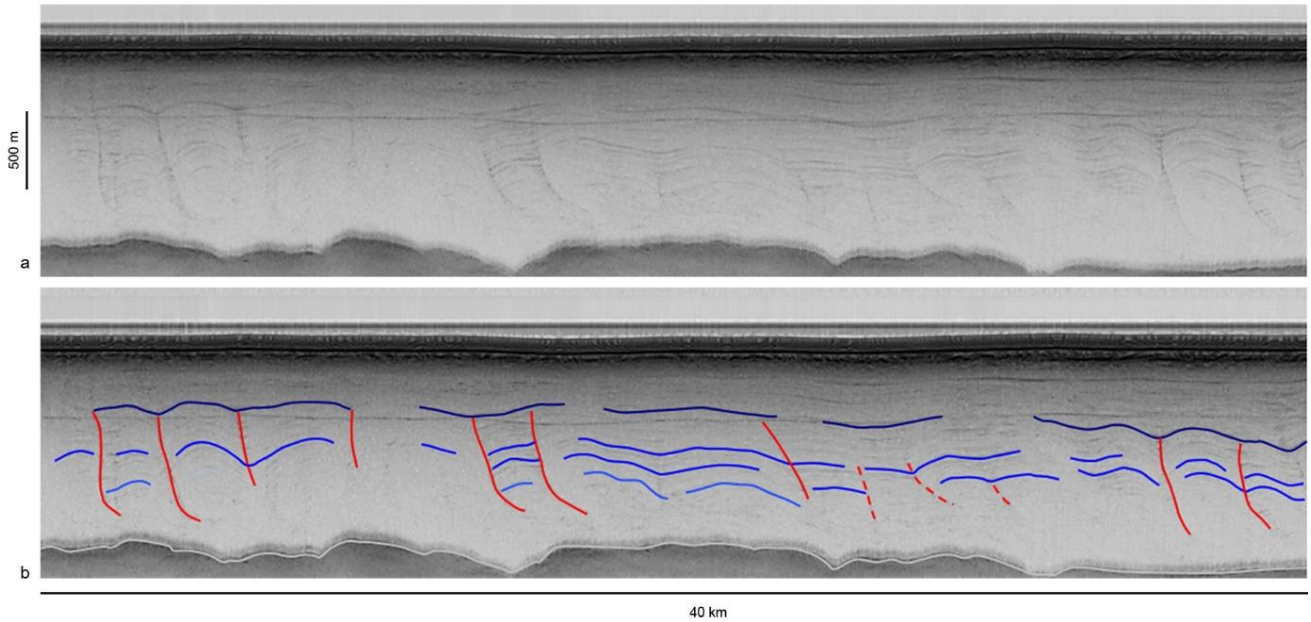

Fig. 3: a) HiCARS observation in the glacier of the Cook ice shelf (vertical exaggeration 5:1). b) HiCARS layer picking. The blue lines represent the top and bottom of the ice layers and the red lines the faults. The dashed red lines represent the picking of secondary faults that are faint structures in the background radargram. The arrows represent the top (grey arrow) and the bedrock (black arrow).

4. Methods

The main radargram reflectors were highlighted by digital selection (manual picking) of the layers and the troughs (Plewes and Hubbard, 2001; Bingham et al., 2007; Utsi, 2017). Fig. 2b and Fig. 3b show the radar interpretation that depicts the internal layering and the main visible structures.

The traced lines appear to be consistent with the structural setting related to the low-angle normal faults with listric shape that create hanging-wall rollover anticlines (Davison, 1986; Williams and Vann, 1987; Fossen, 2010; Grima et al., 2011; Cianfarra and Maggi, 2017; Cianfarra and Salvini, 2016a). Balanced cross sections by means of numerical modeling were used to model and to reproduce the found geometry of the SHARAD and HiCARS selected profiles. Surface lineament domain analysis was performed along the area of both the radar tracks following the methodology presented in Cianfarra and Salvini (2014) to investigate the possible dynamics related to the troughs. The MOC, Landsat-8 and Sentinel-2 images were used to perform the lineament domain analysis.

4.1 Numerical modeling (Hybrid Cellular Automata)

We performed numerical modeling by simulating the kinematic evolution of the troughs. The Hybrid Cellular Automata (HCA)-derived numerical algorithm by means of the FORCtre software allows to replicate the complex evolution of dip-slip geological structures (Salvini et al. 2001; Salvini and Storti 2004).

The simulation was performed on the SHARAD and HiCARS profiles, that both show buried similar structures. A trial-and-error forward modelling approach was followed that consisted in the careful tuning of the fault geometries and displacements in order to achieve the best fit between the model and the interpreted radargram. The initial horizontal dimension of the cells of about 100 m allows to verify the consistency of the requirements for continuous balancing through time, and in turn to obtain a robust model that reconstruct the structural evolution of the studied profile (Tabacco et al., 2006;

Cianfarra et al., 2009; Cianfarra and Salvini, 2016a; Arragoni et al., 2016; Cianfarra and Maggi, 2017). The cell resolution was selected to balance the analysis effectiveness, in order to model the structural elements of the section by preserving the computation time.

4.2 Lineament analysis

The HCA methodology was integrated with automatic lineament domain analysis (Wise et al., 1985; Cianfarra and Salvini, 2014). This analysis was performed in the selected satellite images (Fig. 1) that follow the tracks of the SHARAD and HiCARS data to investigate the connection between the surface and the depth structural setting. Lineaments represent feature alignments in the topography variation enhanced by preferential erosion directions and induced by upper crustal stresses/kinematic conditions (Wise, 1982; Wise et al., 1985; Mazzarini and Salvini, 1994; Pischiutta et al., 2013; Cianfarra and Salvini, 2015; Lucianetti et al., 2017; Rossi et al., 2018). Also in deformed icy surfaces lineaments represent a tool to understand the tectonic scenario of the study area (as resulted in Ganymede surface investigation, Rossi et al., 2018). Their spatial distribution defines lineament clusters that form lineament domains (Wise et al., 1985). Lineament domains are organized around preferential orientations and allow to infer the crustal stresses of the planetary upper crust at the regional scale (Wise, 1982; Wise et al., 1985; Cianfarra and Salvini, 2014, 2015; Lucianetti et al., 2017; Pinheiro et al., 2019).

The automatic detection (SID software; Salvini, 1999) performs a systematic search for straight segments in a discrete image of pixel alignments according to a set of parameters that describe the lineaments to detect (e.g. Rossi et al., 2018). The recognized lineaments are cumulated for the total data analysis to determine the tectonic setting. Following Wise et al. (1985) we performed a polymodal Gaussian fit by frequency to infer the azimuthal trends that characterize lineament domains. This analysis considers negligible the slight map projection distortions for the high latitude (exceeds 80°N) where the investigated images are located.

The recognized lineament domains were compared with the katabatic wind vectors (from both Gemina Lingula and Cook ice shelf glacier) to investigate on their eolian versus ice cap dynamic-related origin.

5. Results

The picking of the main reflector in the analysed radargrams allowed to recognize the top and bottom of the internal layers and the sloping structures (i.e. troughs/faults). This represented a base for the data interpretation and numerical modeling. The HCA models were tuned in order to simulate the geometries highlighted by the radargram interpretation.

5.1 Mars

The SHARAD profile was modelled as a 2D section of layered material 1200 m thick and 200 km long (represented with a vertical exaggeration of 90:1), with a rigidity comparable to that of pure water ice I-h (Poisson's ratio: 0.25; Young's modulus: 70 GPa; Turcotte and Schubert, 2002).

Fig. 4a shows the HCA result of the Gemina Lingula profile. The model replicates the evolution that leads to the formation of the internal layering and the buried trough/fault setting. It is formed by a total of 8 layers and 4 faults recognized by the radargram interpretation (Fig. 2b). Close to the trough/fault planes the NPLD (units 1 to 6) show bended shape. The layers of the unit 7 present a thickness variation, progressively thicker approaching the trough/fault planes. The youngest layers of unit 8 are simulated with a convex shape to replicate the ice cap condensation process. The modelled faults describe the buried troughs of the radar profile. These slightly differ from the structures depicted by the picking (Fig. 2b) and their termination is under the bottom of the section. The NPLD geometries suggest that the troughs/faults may present listric shape and flatten downward, along a deeper horizontal detachment.

Results of the polymodal Gaussian fit of the automatically detected ice surface lineaments is presented in Fig. 4b. A total of 12226 lineaments were identified that cluster into two Gaussian peak (the lineament domains) trending N12°W and N69°E that were compared with the katabatic wind directions (Howard, 2000; Kostich and Smith, 2018). The longest lineaments belong to the main Gaussian peak and form an angle of approximately 15° with the mean trend of N5°E of the wind vectors in the investigated area (green square in Fig. 1a). This domain is parallel to the orientation of the buried troughs in the SHARAD profile. The lineaments of the second domain are relatively shorter and form an angle of approximately 60° with the wind directions.

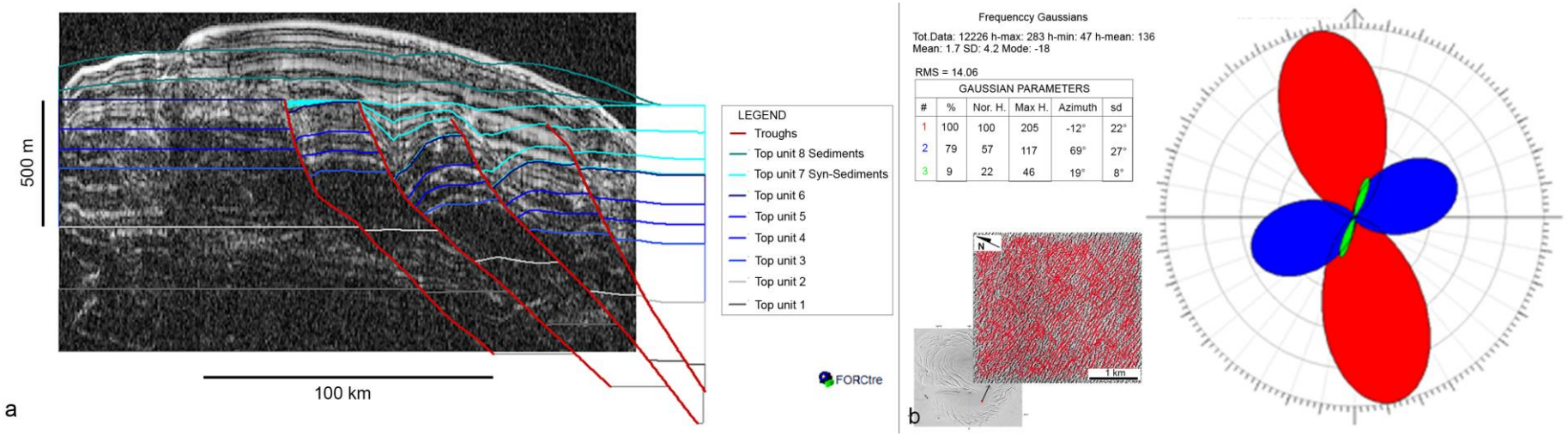

Fig. 4: Mars north pole results. a) HCA model of the SHARAD profile (in background) where the limits of 8 layers/units are reported and 4 buried troughs. b) Lower-left the area located in Gemina Lingula where the lineament analysis was performed, and the arrow indicates the M01/05987 MOC image (82°N 17°E) with the recognized lineaments. The rose diagram represents the lineament domain analysis. The red Gaussian peak represent the main lineament domain, the blue peak is the secondary one. The Gaussian Parameter are reported: the number of Gaussian peaks (#), the percentage of occurrence (%), the Normalized Height (Nor. H.), the Maximum height (Max. H.), the azimuth, and the standard deviation (sd).

5.2 Antarctica

The HCA model of the Antarctic HiCARS profile is shown in Fig. 5a and consists of ice layers 1200 m thick and 40 km long. The obtained result characterizes a total of 6 main units cut by 13 faults. Their displacements are sufficient to reproduce the bending of the layers as resulted in the radar interpretation shown in Fig. 3b.

The lineament domain analysis performed in the Landsat-8 and Sentinel-2 images (Fig. 1b) allowed to recognize a total of 846 lineaments clustered into two lineament domains that were compared with the Antarctic katabatic wind directions (Parish 1984, 1988; Parish and Bromwich 1986; Fig. 5b, green square in Fig. 1b). The main lineament domain trending N36°W presents the longer lineaments and is nearly parallel to the N40°W wind direction (and to the buried structures of the HiCARS profile), and the second, minor lineament domain trending N89°E presents shorter lineaments forming an angle of approximately 50° with the winds.

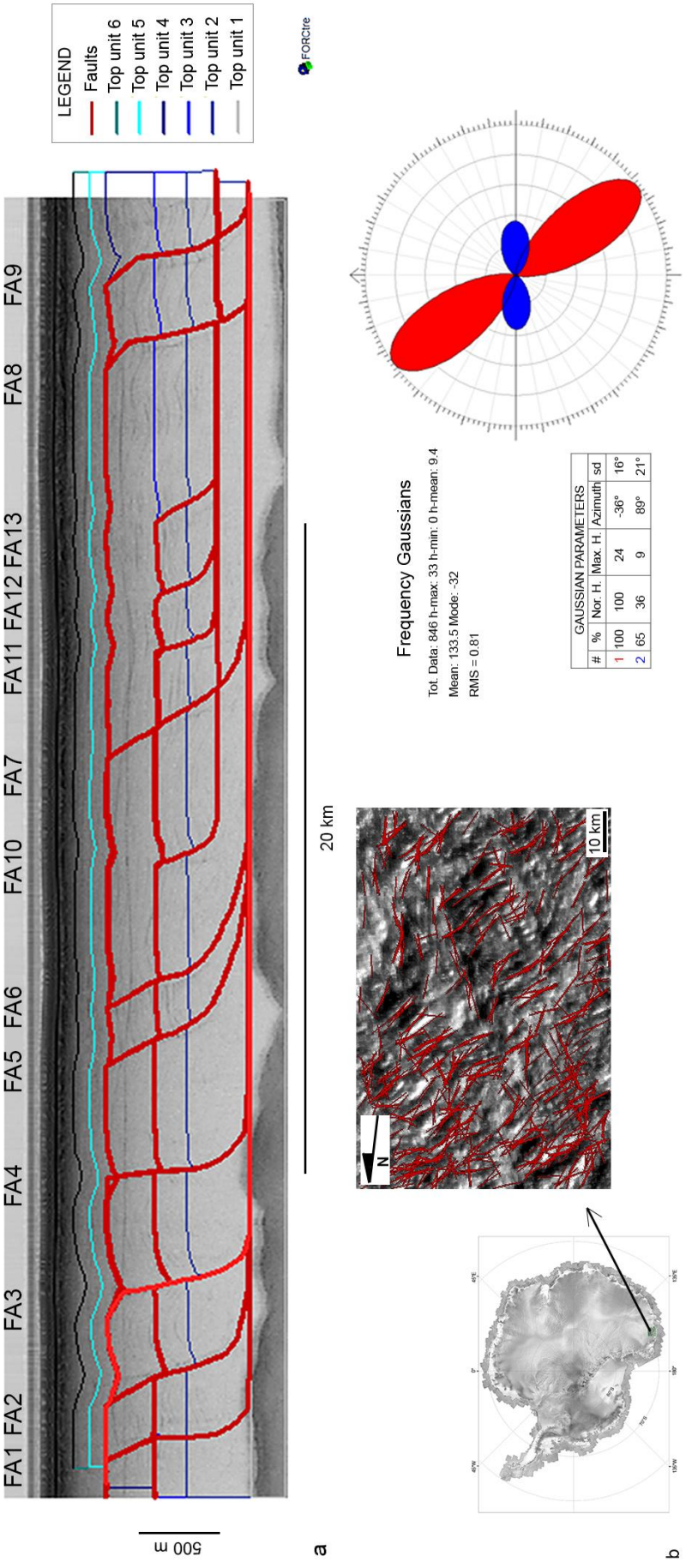

Fig. 5: Antarctic analog results. a) HCA model of the HiCARS profile (in background) where the limits of 6 layers/units are reported and a total of 13 structures. b) On the left the investigated area in the glaciers of the Cook ice shelf. The green square and the arrow indicate the Sentinel image with the recognized lineaments. The rose diagram represents the lineament domain analysis. The red Gaussian peak represent the main lineament domain, the blue peak is the secondary one. The Gaussian Parameter are reported in Fig. 4b.

6. Structural evolution of the North Polar troughs

Fig. 6 shows the HCA evolutionary model of the buried trough section in Gemina Lingula. Gravitational collapse and internal dynamics produce extensional regime that characterizes the activity of listric faults connected at depth with a ductile detachment located at the base of the model. Faults migrate with normal propagation sequence from the oldest fault-1 (F1 in Fig. 6a) to the youngest fault-4 (F4, Fig. 6d).

Fig. 6a shows the activity of F1 modelled characterized by a displacement of 50 m that offset the internal ice layering. F1 changes its dip at 300 m depth within unit 3 to create a step in its trajectory, similar to that observed in listric faults, and maintains its gentle slope until the base of the modelled section. Fault activity bends the hanging-wall ice layers that form a rollover anticline and create a site of preferential deposition where syn-sediments (ice) is accumulated by possible eolian activity.

In Fig. 6b is illustrated the activity of F2. Its normal displacement of 300 m offset the internal ice layers that bend to form a hanging-wall rollover anticline. Ice syn-sedimentation is characterized by higher thickness of 300 m close to the trough/fault surface and lower thickness of 100 m away from the fault. F2 gently rotates within the unit 3 and maintain a constant dip until the base of the section.

F4 is characterized by a displacement of 400 m that offset the ice layers (Fig. 6c). It creates in its hanging-wall a roll-over anticline and the ice syn-sedimentation ranges from 400 m thickness close to the trough/fault surface to more than 200 m away the fault. Its shape is characterized by a gentle change of dip between the units 4 and 3 and maintains a straight trajectory until the base of the section.

In Fig. 6d is shown the F4 characterized by a displacement of 30 m. It cuts the layers of the ice syn-sediments and maintains a constant dip until the base of the section. This nearly flat fault geometry prevents from the formation of rollover anticline and the accumulation of ice syn-sediments.

The modelled troughs/faults are connected with a ductile detachment at more than 1000 m depth in the interior of the ice cap. This is deeper than the base of the section.

Fig. 6e shows the burial of the described faults. The increasing of the ice cap by condensation creates the typical domed form of the cap (ice at the top).

The dynamics described in this model can be extended also to the surface spiral troughs. The troughs trending nearly orthogonally to the wind direction remain at the surface, and the trough with other orientations are buried. A similar structural evolution was modelled for the Antarctica analog (Fig. 5) and depicts what observed in the studied Antarctica radargrams.

Similar tectonic setting characterized by the activity of blind listric faults allowed to replicate the internal layering of the Antarctic analog (Fig. 4a). A total of 13 faults m were modelled with normal displacement ranging between 30 and 50.

Two events characterize the formation of the recognized faults. The main listric faults (FA1-FA9) form at approximately 300 m depth. These develop downwards and curve within unit 2 until the top of unit 1 (i.e. ice-bedrock interface). The best fit between the layering in the HCA model and the geometries derived from the radargram was achieved with a basal detachment placed at the top of unit 1, at depth of more than 1000 m.

Secondary minor listric faults (FA10-FA13) form at the top of unit 3 at approximately 500 m depth and sole out into a shallower detachment within unit 2 at approximately 700 m depth.

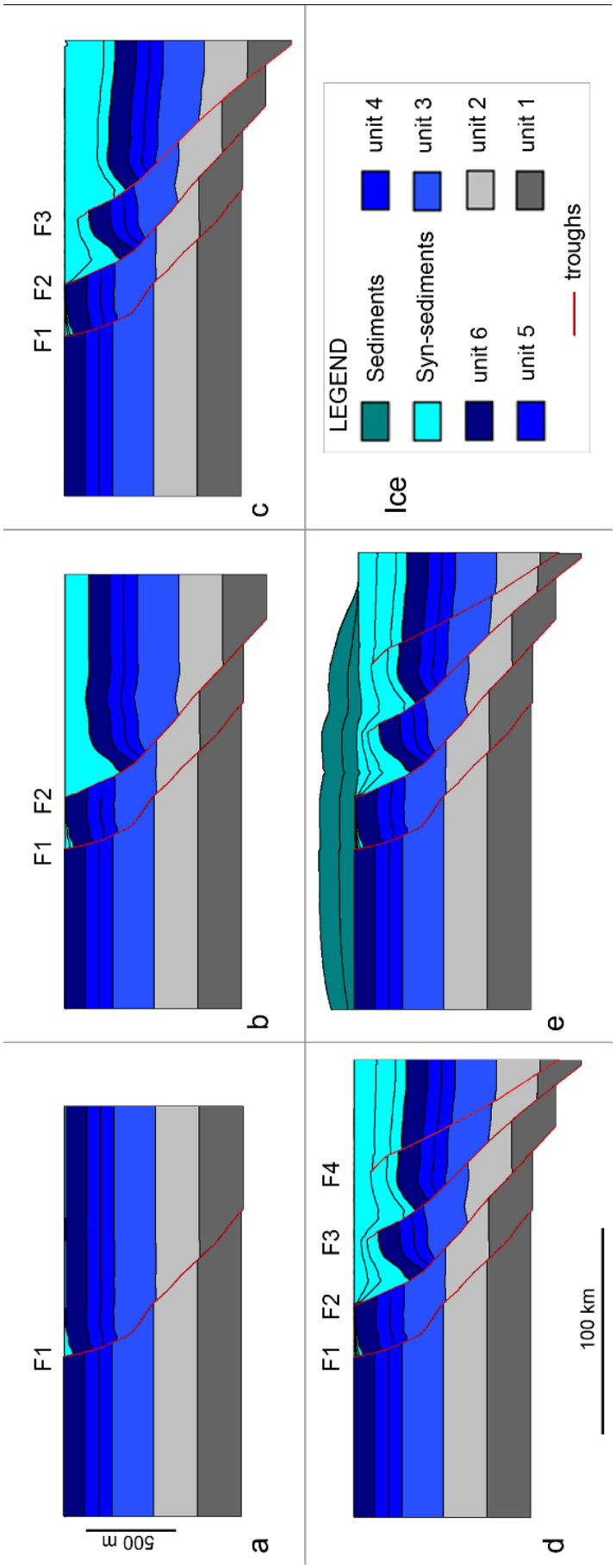

Fig. 6: Evolutionary model of the Mars polar troughs. a) propagation of the fault-1 with consecutive bending of the layers and syn-sedimentation; b) fault-2 development; c) fault-3 development; d) fault-4 development; e) sedimentation with dome shape of the ice cap with trough burial.

7. Discussion

The obtained results suggest that Planum Boreum ice cap is structurally controlled, and the troughs/faults represent structural features. The NPLD and the spiral troughs frame a well-defined tectonic scenario (e.g. Gibbs, 1984; Jones, 1988; Duval et al., 1992; Bosworth, 1994; Phillips et al., 2013; Robson et al., 2017). The troughs/faults are modelled as low-angle normal faults (Wernicke, 1981; Scott and Lister, 1992; Fossen, 2010; vertical exaggeration 90:1 in Fig. 4a) that cut and offset the NPLD with fault throws ranging between 30 m and 50 m. Evidence validates the trough/fault listric shape, as indicated by the NPLD bending in their hanging-wall. These are modelled as rollover anticlines with consequent syn-sedimentation (unit 7, Fig. 4a) that typically shows thickening toward the controlling fault (Childs et al., 2003; Fossen, 2010). The reverse migration of the shallow undulations (Cutts et al., 1979; Herny et al., 2014; Smith and Holt, 2015) recognized in several SHARAD data (e.g. the radar observations 6247_02, 933202, 2007101, 2007101; Smith and Holt, 2015) are similar to hanging-wall antithetic structures that form during the normal fault propagation process (Fossen, 2010).

The modelled troughs/faults (Fig. 4a) slightly differ from structures integrated from the radargrams (Fig. 2b). This suggests the coexistence of a horizontal component with extension. The HCA method allows to simulate only dip-slip processes and thus to reproduce the studied trough/fault geometry pure extension is considered. In this way in the HCA simulation dip-slip normal faults were modelled. The strike-slip component is revealed by minor misfit between the model and the interpreted radargram. In this way, the modelled traces of the fault were simplified since the HCA modelling considers the dip-slip displacement only.

As a result, the modelled trough/fault dips are steeper than the picked in the radargram, and may flatten into a weak deeper detachment, resulting in horizontal slip (Fossen, 2010). According to the proposed model the depth of the detachment is more than 1000 m. This may in turn testify the possible

presence of a ductile or semi-fluid layer within the ice cap that enhances internal horizontal slip. Grima et al. (2011) found listric structures in the south pole counterpart and suggested a detachment depth at approximately 1000 m. At a similar depth Orosei et al. (2018) found H_2O reflectors (approximately 1500 m of depth). Their study area is relatively close, further south to the study area of Grima et al. (2011). We deduced from their findings that the presence of H_2O fluid layers between approximately 1000-1500 m of depth may play a key role to develop detachments with consequent brittle deformation in the south pole (i.e. the listric faults found by Grima et al., 2011). In this way, a similar scenario can easily develop also in Planum Boreum with the detachment depths similar to the south pole ones. This suggests the occurrence of ice cap internal melting.

The observation of slope diversity of the spiral troughs at the surface of Planum Boreum also confirms the structural meaning of these features. The equator-facing slopes that show truncated layers represent the surface of the fault plane, and the pole-facing slopes represent the curved top of the hanging-wall rollover anticline and/or the sediments deposited during the trough/fault activity. The found heterogeneity of the trough/fault throws is typical of tectonic processes, in contrast with the nearly homogeneous, regular setting expected by the eolian activity.

The recognized lineament domains along the surface of the investigated radargram allow to relate the main lineament domain with the trough/fault activity (Fig. 4b). On the other hand, the longer lineaments of the main lineament domain, nearly parallel to the wind direction, trace the buried trough orientation of the investigated depth profile. According to Wise et al. (1985) this lineament setting is compatible with the presence of an extensional regime at depth within the ice cap, orthogonal to the main lineament domain. The second peak (Fig. 4b), at 45° with the wind direction, may relate to eolian factors.

The proposed model refers to the internal dynamics of Planum Boreum ice cap. It describes the structural nature of the troughs/faults that originated by extensional (gravitational) sliding within the cap. We propose the presence of a deep detachment whose kinematics develops brittle structures (i.e.

the troughs) on the upper ice layers. The selected profile shows buried troughs with orientation not compatible with the vector directions of the katabatic winds. The fourth trough/fault (F4 in Fig. 6d) also provides interesting evidence. It is well developed at depth and its upper tip seems to weakly reach the surface where a small trough can also be detected from the satellite images of the surface. This is typical of the fault propagation process that migrate upwards during the final stage (Salvini and Storti, 2004). The model considers the significance of the katabatic wind activity and the Coriolis effect (Smith and Holt, 2010). These play a secondary role by maintaining at the surface the troughs that are tailwind oriented. Their erosive action allows to preserve the upwind trough/fault planes at the surface (equator-facing slopes) and to accumulate syn-sediments in the downwind slopes, i.e. the hanging-wall (pole-facing slopes).

The analogy with the depth profile of the Antarctic glacier further strengthens the proposed structural model for the Martian North polar cap. The investigated HiCARS profile shows listric structures at a depth of 500 m related to the ice sheet dynamics. Terrestrial glaciers deform for the gravitational flow and underlying topographic variation. Crevasses, fractures and faults are typical features produced in glacial environment, and listric faults are frequently reported in terrestrial glaciers (e.g. Phillips et al., 2013). The modelled structures in the Antarctic analog are blind and have synchronous activity with subsequent bending of the ice internal layers. The formation of these faults also depends on the morphology of the underlying topography (as observed in the BEDMAP2, Fretwell et al., 2013). The layer bending is compared with rollover anticline (and synclines) and the blind structures present listric shape. These provide geometry similar to the martian troughs/faults and their activity possibly controls the surface lineaments (Fig. 5). As in Planum Boreum, two lineament domains were found and are considered the effect of two processes, the eolian and the structural one. The NW-SE main lineament domain can be associated with the stress-field that is characterized by NE-SW trending extension responsible of the blind listric faults. The second minor peak is related to exogenous activity (Fig. 5b). No surface troughs and no spiral pattern occur in the Antarctic ice sheet surface. Antarctic

ice sheet presents thickness higher than the North polar cap of Mars and the bedrock is more pronounced than the Basal Unit of Planum Boreum. The Antarctic wind regime (reaching their maximum around 300 km/h; Parish. 1984) is lower than the martian one (around 400 km/h; Howard, 2000) and different accumulation/ablation allows to maintain the mass balance stable. In this way, Antarctic katabatic winds allow to form eolian features that reach less than 100 m of depth (such as the megadunes, Frezzotti et al., 2004, that form in a different way than the martian spiral troughs), and weakly maintain brittle structures at the surface, that inevitably become buried.

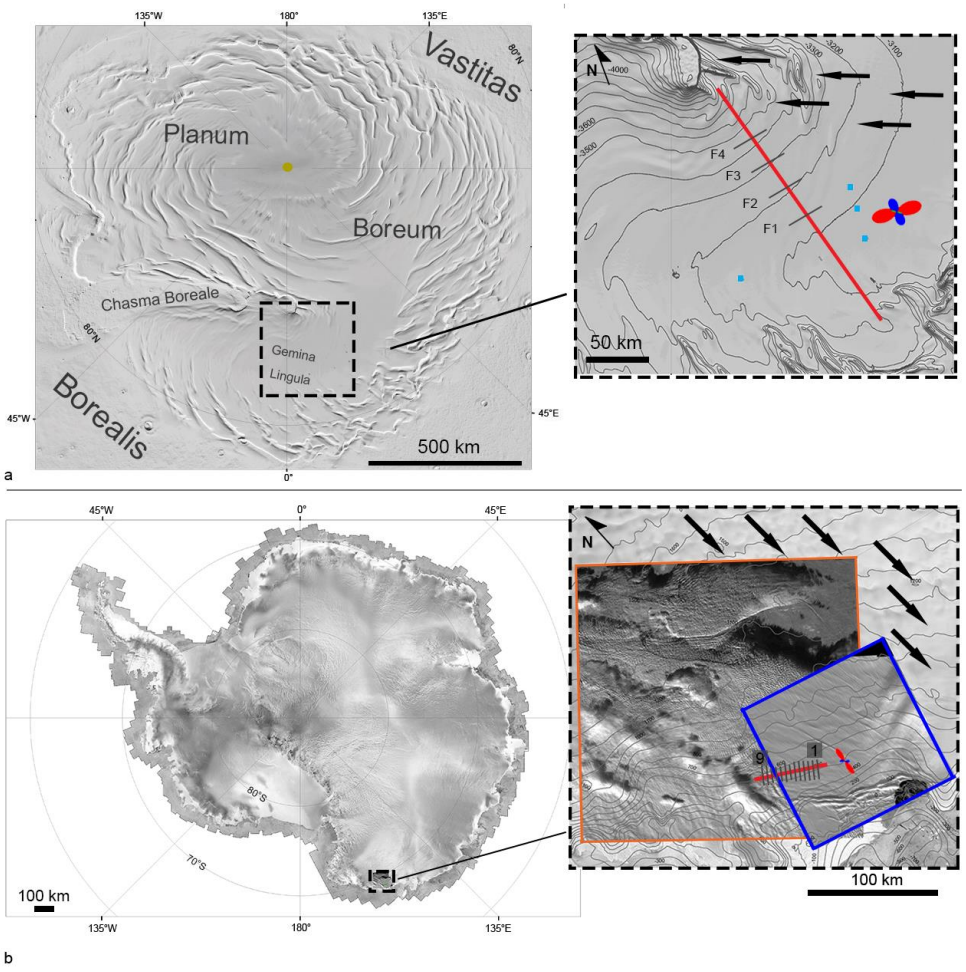

Fig. 7: Comparison and group of the obtained results. a) Gemina Lingula study area. The red line shows the track of the SHARAD profile dissected by four dark grey lines that represent the inferred fault locations (from F1 to F4, see Fig. 4). The black arrows show the katabatic wind vectors from Kostich and Smith (2018) and the small rose diagram represents the lineament domain recognized in the MOC images (light blue squares). b) Cook ice shelf glacier. The red line shows the track of the HiCARS profile dissected by 13 dark grey lines that represent the inferred fault locations (numbers 1-13 refer to FA1-13 of Fig. 5). The black arrows show the katabatic wind vectors from Parish and Bromvich (1986) and the small rose diagram represents the lineament domain recognized in the Sentinel-2 (blue square) and Landsat (orange square) images.

8. Conclusions

Tectonic processes play a key role in the formation of Planum Boreum troughs. Horizontal slip induced by a deep detachment (more than 1000 m deep) and glacial flow are responsible of internal dynamics. This induces brittle deformation (faulting) expressed by the troughs. Their listric shape and their structural setting assume that they formed under prevailing extensional tectonic regime. Katabatic winds are responsible of the subsequent syn-sediment deposition and the trough conservation at the surface. The modelled structural setting of the formation of the martian spiral troughs through the activity of listric normal faults within the ice cap shows similarities with blind faults found in Antarctica analog.

The evidence for trough structural origin opens new debate. The suggestion that troughs are triggered by fault activity provides the possibility to investigate preferential ways that connect the ice cap interior with the surface. The presence of detachment is significative for future investigation on the identification of internal ductile/fluid (H_2O) layers.

The used methods represent a potential tool that can be extended to provide information on the geological and structural evolution of Mars south polar cap, as well as of the icy satellite morphotectonic structures. The simulation of the structure evolution at depth by using radar sounding data was successful and represents a promising mean to investigate the tectonic setting of their icy crusts.

CHAPTER 5

DISCUSSION

5.1 Study case comparison

The investigated icy surfaces represent optimal examples of ice tectonics and their modeling allowed to identify the main tectonic styles that originated their structural setting. The large satellite Ganymede, the smaller Enceladus, and the martian northern ice cap present similarities and differences that allow to recognize the preferential way of tectonic structure formation and to infer the geodynamic implications. The three icy surface study cases are connected by their mainly water-ice composition and their regional scale brittle deformation.

A main difference clearly exists between the icy satellites and the ice cap of Mars.

5.1.1 Ganymede and Enceladus

Ganymede and Enceladus represent confined icy surfaces, characterized by an icy crust above a subsurface ocean. They belong to two different systems (the jovian and the saturnian), and differ in crustal thickness and timing of tectonic activity.

Ganymede crust is approximately 100 km thick and the surface structures formed during past tectonic activity, when the crust was assumed to be approximately 10 km thick (Golombek, 1982). This value is similar to the assumed thickness of Enceladus South Polar Terrain (less than 10 km) where recent tectonic activity has been observed. In both these icy satellites, the structures are investigated at the regional scale, with a maximum length of more than 100 km. Tectonic structures are classified into structural systems and are arranged into bands that are spatially distributed in their surface. Authors recognized extensional regime as the main responsible for their formation mechanism (McKinnon and Melosh, 1980; Pappalardo et al., 1998; Pappalardo et al., 2004; Pizzi et al., 2017), while this dissertation identifies the frequency and importance of regional shear in their surfaces.

5.1.2 Mars northern ice cap

The northern polar cap of Mars, Planum Boreum, represents an unconfined, "open" system above a basal unit that is mostly composed by sand (Brothers et al., 2015). In comparison with the mentioned icy satellites, that present several systems that intersect and crosscut each other, Planum Boreum presents a system of troughs rather equally spaced (about 30 km) with a similar length of about 60 km disposed in a spiral arrangement. This dissertation proposes their structural origin, interpreted as extensional low-angle faults that connect into a detachment. The tectonics of Planum Boreum troughs is compared to the dip-slip structures recognized in the icy satellite Ganymede and Enceladus. Many authors modelled extensional tectonic setting in icy satellites with listric normal faults that sole out on a detachment at depth, similarly to the scenario proposed in Planum Boreum ice cap (e.g. Pappalardo and Greeley, 1995; Pappalardo et al., 1998; Yin and Pappalardo, 2015).

5.1.3 Antarctica

Antarctica dynamic ice cap presents structures that reveal analogies with the recognized tectonic styles in the icy planetary surfaces. In map-view, the icy satellite strike-slip structures are similar to those formed in glacial environment related to glacier flow. At depth, the Antarctic structures show analogies with the low-angle internal structure of Planum Boreum troughs.

In comparison with the icy planetary surfaces that show more developed deformation at the regional scale, glaciers and ice cap on Earth provide local scale deformation (as the crevasses). Their water ice composition differs from those of the icy planetary surfaces that include smaller percentage of other components (e.g. ammonia, CO_2; Prockter, 2005; Porco et al., 2006). These may have influenced the pervasive regional scale ice fracturing that occurs in icy planetary surfaces.

5.2 Tectonic style endmembers

The comparison of the obtained results and the proposed tectonic models allows to recognize two endmembers of the icy surface tectonic styles at the regional scale. These are the strike-slip and the low-angle dip-slip that represent the preferential way of planetary ice deformation. These tectonic styles occur with different frequency in confined and unconfined icy surfaces.

Obtained results show that strike-slip tectonics play a key role at the regional scale in confined icy surfaces, represented by the icy satellite crusts. Dip-slip extension is recognized at the local scale with low-angle structures and is assumed to play a secondary role. The low frequency of compression is supported by the amount of transpression that could represent the balancing way for the recognized extension.

On the other hand, dip-slip tectonics occurs with non-Andersonian mechanism and forms low-angle structures. This is evident in the unconfined icy surface of Planum Boreum, where the open configuration allows to create dip-slip faulting. Unconfined icy regions are also associated to a strike-slip component that, in this case, plays a secondary role.

5.3 Topographic flattening

Although the topographic database of icy satellites is very limited, it is commonly suggested that icy satellite topography is relatively flat (Schenk et al., 2018; Kay et al., 2019). The icy surfaces often show low topographic amplitudes, with gently undulating deformation (Kay et al., 2019). Tectonic structures play a main role in shaping icy satellite surfaces and the obtained results of this dissertation show that they contribute to control the topography variation. Their high density and abrupt interruption of the landscape characterizes more the surface roughness than a significant topographic variation. This is well observed on Europa, that presents one of the best examples of compression in icy satellites. Here compressional bands that subduct at low-angle characterize the subsumption tectonic model (Kattenhorn and Prockter, 2014). Conversely to what occurs along the subduction

zones on Earth that present uplift zones, the Europa subsumption bands are basically topographically flat (Kattenhorn and Prockter, 2014). On the other hand, Antarctica represents a good terrestrial analog. Its plateau lack in structural high, and the domes that occur at the surface are formed by ice accumulation and are not tectonic related. Several Earth active glaciers present no high topographic variation but rather landscape roughness, although they cover and reproduce the bedrock topography. Fig. 1 shows an example of ice landscape roughness. The terrestrial ice cap and glaciers reach their steady state until the equilibrium line altitude, where the equilibrium between accumulation/ablation occurs. This suggests that ice weakly maintain the topography variation, and, in planetary surfaces, tectonics is supposed to contribute to the ice topography flattening.

Also unconfined icy surfaces, as Planum Boreum example, show low-angle detachment structures that create gently variating topography. The topography undulation formed by the troughs slightly variates the gentle dome slope profile of the ice cap, in contrast to the vertically exaggerated profile that shows an apparent disrupted cap topography.

The two endmembers, strike-slip and low-angle dip-slip, both support the flattening of the icy planetary surfaces. High-angle dip-slip structures are hardly present since these create a significant increase of crustal thickness. Conversely, low-angle structures lead to a moderate and gentle lateral topographic variation as observed at the larger scale. Their presence develops to avoid strong variations in thickening. In this way, icy surface tectonics is supposed to control topography that reaches stability by maintaining a nearly flat landscape. The low amplitude of topographic low and high testifies this setting. The prevalence of strike-slip tectonics in icy satellite surfaces supports a topographic balancing, where tectonics could contribute to accommodate the ice thickening variations. In this way, the tectonic style endmembers are dependent on topographic flattening. Tectonic deformation, caused by several processes, is supposed to contribute to the flattening by preferring low-angle dip-slip structures and by producing strike-slip that moderately shape the surface. High-angle dip-slip structures possibly develop at the early stages and are erased or

subsequently re-used as strike-slip. In this way, strike-slip represents the prevailing structures that develop with high-angle dip in icy surfaces and their contribution to vertical variation is faint.

Fig. 1: Campbell Glacier terminus, near Gondwana station in Antarctica (74°37’56’’S 164°16’13’’E). PNRA XXXIV expedition.

5.3.1 Thin-skinned tectonics and fault inversion

Low-angle tectonic styles refer to the so-called thin-skinned deformation (Rodgers, 1949; Harris and Milici, 1977; Vendeville and Jackson, 1992; Lundin, 1992; Lankreijer et al., 1995; Pfiffner, 2017). This model suggests the prevalence of flat geometries that structurally thins the overburden (Vendeville and Jackson, 1992). Earth thin-skinned tectonics involves the deformation of sedimentary cover that is connected to a basal sole thrust or detachment (Vendeville and Jackson, 1992; Fossen, 2010; Pfiffner, 2017). In icy planetary surfaces thin-skinned deformation is supposed to involve the upper layers without deep penetration of dip-slip structures. In this way, shortening and extension develop a sort of smoothed topography, vertical thinning, and possibly share the same low-angle structures. Fault inversion from horizontal contraction may lead to the reactivation of pre-

existing reverse faults and the formation of new normal faults, and conversely, from a low-angle normal fault to a thrust. These exhibit a trend from thin-skinned deformation and experience similar low-angle structures that can evolve and variates their kinematics. Thin-skinned tectonics leads to the development of low-angle structures used in both contraction and extension regimes. In this way, the icy satellite extensional detachments represent a potential result of old compressional structure reactivation or, conversely, could be reactivated by future variation of tectonic regime.

5.4 Geodynamic processes

Results from this dissertation allow to identify possible geodynamic processes responsible of the tectonics in the investigated icy surfaces. Tidal heating (Beuthe, 2016), convection (Barr, 2008), and ocean crystallization (Johnston & Montési, 2017) are some of the several proposed processes. Obtained results provide support for geodynamic processes such as Polar wandering, Coriolis, and regional-scale flow.

5.4.1 Polar wander

The prevalence and distribution of strike-slip structures provides evidence for polar wander in the icy satellites (Sarid et al., 2002). This infers that mass migration and redistribution within these bodies occurs/occurred with subsequent perturbations of tectonic stresses (Vening Meinesz, 1947; Matsuyama and Nimmo, 2008; Matsuyama et al., 2014). The drifting of crustal masses is framed in the polar wandering model (Matsuyama and Nimmo, 2008). Polar wander could play a significant role to develop tectonic deformation at the surface. The continuous readjustment of the rotation (and tidal) axis orientation leads the reorientation of the body and in turn can generate global-scale tectonic patterns (Vening Meinesz, 1947; Sarid et al., 2002; Matsuyama and Nimmo, 2008; Matsuyama et al., 2014). Matsuyama and Nimmo (2008) proposed that polar wander characterizes pervasive strike-slip regime that could represent preferential ways for crustal drifting paths. The structural geology results of this dissertation support the polar wandering model proposed for both the investigated icy satellites

(Ganymede, Matsuyama et al., 2014; Enceladus, Tajeddine et al., 2017) as possible geodynamic process in conjunction with other ones.

5.4.2 Coriolis force

Similarly to the polar wander process effects, the Coriolis force effect is also taken into account as possible process that could influence icy surface tectonics. Enceladus SPT and the martian study area are both localised at the poles. Both areas show rotation of the structures that follow the prograde sense of their rotation axis (Dougherty et al., 1982). The spiral setting of Planum Boreum troughs is disposed in a counterclockwise path and the SPT Tiger Stripes propagates with a CW rotation. The transpressional regime of Enceladus SPT could be subjected to Coriolis deflection that causes the CW rotation of the internal Tiger Stripes. The compressional component that is present in the region leads to the structure approaching to the pole. This approaching could deflect CW the structures by Coriolis force. On the other hand, the spiral pattern of Planum Boreum troughs is supposed to be related to katabatic winds deflection by Coriolis effect. This force represents a potential perturbation also of the flow lines that kinematically induce the internal detachments that provide a spiral pattern.

5.4.3 Flow

The presence of low-angle faults leads to the inference that flow represents a significative factor as structural dynamic driving. As terrestrial glaciers flow downslope and deform under the force of gravity, the icy planetary surfaces show predisposition to flow. The formation of master detachments testifies this mechanism and represents a behavior variation at depth of the internal ice layering. Horizontal gradients of ice thickness are expected to drive a global ice flow that separates the upper brittle ice surface from a more ductile ice at depth. Flow represents a possible mechanism that equilibrates and stabilizes the ice thickness variations. Where topography thickens, due to several factors, the flow is manifested by detachment development to rebalance the ice thickness disparity

and to reach topographic stability. The resulting kinematics induces upper brittle deformation that in turn generates tectonic structures at surface.

This is well shown in Planum Boreum and Antarctica ice caps that are subjected by collapse driven by dynamic flow to equilibrate the line altitude rises. Low-angle normal faulting could also be the consequence of this flow.

These processes are supposed to coexist and possibly are responsible for the thin-skinned tectonics. This could be driven by flow that constantly generates mass redistribution within the icy surface to balance any surface thickening. In this way, ice tectonics is strictly influenced by a topographic balancing pursuit of the icy surfaces that tend to reach the steady state level.

CHAPTER 6

CONCLUSIONS

This dissertation addresses four scientific issues related to the tectonics of icy planetary surfaces. These are: i) the modeling of the tectonic evolution of study areas in confined versus unconfined icy surfaces; ii) the tectonic styles in icy surfaces; iii) their deformation mechanisms; iv) structural balancing and geodynamic implications.

i) The investigations of Ganymede, Enceladus and Mars northern ice cap allow to propose a total of three tectonic models that describe the kinematic evolution of the studied icy surfaces. Regional transpression inducing extension/compression prevail in the confined icy crusts of Ganymede and Enceladus. Mars unconfined icy surface reveals internal dynamics that forms extensional troughs/faults with a secondary strike-slip component. Their evolutionary models allow to understand the preferential ways of ice failure in planetary surfaces. Ganymede and Enceladus tectonic model shows regional scale transpression, and the proposed model of Mars north ice cap show extensional regime.

ii) Two tectonic style endmembers characterize the investigated surfaces at the regional scale. These are strike-slip and low-angle dip-slip tectonic faults. The strike-slip represents the main component that deforms the confined icy satellites, and low-angle dip-slip regime develops in the unconfined ice cap of Mars. These endmembers relate to a well-defined tectonic deformation due to topographic flattening of the icy surfaces.

iii) This is represented by thin-skinned tectonics that is suggested to play a key role in the deformation of the icy planetary surfaces. This scenario is supposed to support topographic flattening of the icy surfaces. Tectonic structures are related to the upper layers and possibly can experience kinematic inversions since they possibly share the

same low-angle features. In this way, thin-skinned deformation and fault inversion are suggested to balance the ice tectonics.

iv) Geodynamic considerations are taken into account. The pervasive spatial distribution of strike-slip structures in the icy satellites suggests that polar wandering may play a key role in the formation of tectonic patterns in their crusts. The presence of rotation in the polar study cases of Enceladus and Mars suggests deflection driven by Coriolis effect. The low-angle dip-slip endmember is possibly characterized by internal flow activity that controls the structural kinematics of detachment/thrusts.

Results provide an important step toward the understanding of the tectonic evolution of icy planetary surfaces. The recognized two endmembers provide inferences on the ice setting at depth, and in particular of icy satellite internal crust. Low-angle dip slip structures are not supposed to reach significant depth, rather, these are supposed to develop along a shallow detachment (or thrust). On the other hand, the strike-slip endmember follows the Andersonian fault theory and is supposed to develop a nearly vertical structures that can potentially reach great depth (e.g. the San Andreas fault on Earth reaches more than 4 km at depth; Hickman et al., 2007). In this way, the strike-slip structures represent the optimal way to connect surface with deep layers such as the subsurface liquid ocean of the icy satellites. These faults represent the optimal tectonic candidate for fracture-controlled permeability (Cox, 2010), being more inclined to fluid raising, and plumes, as observed along the Enceladus strike-slip Tiger Stripes.

As in the terrestrial counterparts, the recognized thin-skinned style of deformation in icy surfaces possibly characterizes subsurface structural traps of liquid reservoir accumulation in non-exposed tectonic structures (Harris, 1977). In this way, thin-skinned tectonics represents a potential mean to reach subsurface fluids, shallower than the ocean. This has been observed in the Ganymede icy crust, where the recognized tectonic structures can improbably cross the 100 km crust thickness and connect to the underlying ocean.

The study case comparison in this dissertation has proved an effective tool to unravel the tectonic evolution and the deformation styles of the icy planetary surfaces. This was strengthened by the investigation of the terrestrial analogs that represented decisive means.

The used methodologies represent a powerful tool to unravel the raised scientific issues and a promising means to the preparation of the future mission programs.

6.1 Perspectives

This dissertation opens possible directions for future work. Obtained results provide significant contributions for the future missions in the icy satellites and Mars polar cap (e.g. ESA JUICE mission, NASA Europa Clipper). These missions will be useful to the target areas identification from the geologic, tectonic, morphological and astrobiological point of views. The future data could be used for further investigations to explore the causes of the structural evolution of the icy bodies. Identification of possible connecting fractures with the internal layers is also an important task.

Moreover, the radar sounding data of the future exploration programs will be decisive for 3D modeling of the internal structural evolution in icy crusts and to unravel the structure relative ages.

ACKNOWLEDGEMENTS

The journey to a PhD is not made alone and I would like to recognize the people who have assisted, contributed and accompanied me along my way.

Many thanks go to my supervisor prof. Francesco Salvini, who gave me the opportunity to explore and to discover wonders of the solar system. Huge and special thanks to Paola Cianfarra for all that she has done for me and to be my guidance that kept me on the right path. Thanks to Olivier Bourgeois, Gabriel Tobie et Marion Massé, for their contribution to the work presented in this dissertation and their kind hospitality. Thanks to Matteo Maggi, because it is always a pleasure to discuss with him. I would like to acknowledge the reviewers Ernst Hauber and Goro Komatsu for their constructive remarks that improved the quality of this dissertation.

I would like to recognize all the people who have made the last three years enjoyable and productive. Thanks to my old friends Roberta, Chiaretta, Martina Torelli, Elisa, Matteo, Tullia, Carol, Lucrezia, Mimosa, Marzia, Marco, Ezio, Agnese, Fabrizio, Simone, Melissa and Mèric. Thanks to my university mates Simone, Federico, Alessandra, Dario and Azzurra. Thanks to the new friends that I met during these years thanks to this experience. Thanks to Martina Balestra, Apurva Oza, Laura Guzzetta, Jacopo Nava, Barbara De Toffoli. Many thanks to the antarctic friends Simona and Angelo, and the Litell Rocks remote camp group Gianni Capponi, Samuele Agostini, Laura Crispini, Sonia Sandroni.

I would like to warmly thank the people that always affected me personally and always supported me in my successes, failures and choices in life. Thanks to my beautiful family. Thanks to my mom Cristina, since she possibly thinks that her daughter will become astronaut, and thanks to my beloved sisters Francesca and Anna, since they possibly are scared that their little sister will become astronaut.

Heartfelt thanks to the shiny happy person that endured me in the ups and downs of the graduate school experience and supported me in the best possible way in these years. Thanks Renato. And, of course, thanks Havana for being so cute.

REFERENCES

Alberts, F. (Ed.) (1995). Geographic names of the Antarctic. National Science Foundation.

Anderson, J.D., Lau, E.L., Sjogren, W.L., Schubert, G., Moore, W.B., 1996. Gravitational constraints on the internal structure of Ganymede. Nature 384 (6609), 541–543. https://doi.org/10.1038/384541a0.

Anderson, J.D., Jacobson, R.A., Lau, E.L., Moore, W.B., Olsen, O., Schubert, G., Thomas, P.C., 2001. Shape, mean radius, gravity field and interior structure of Ganymede. Bull. Am. Astron. Soc. 33, 1101. https://doi.org/10.1006/icar.2001.6664.

Arragoni, S., Maggi, M., Cianfarra, P., & Salvini, F. (2016). The Cenozoic fold-and-thrust belt of Eastern Sardinia: Evidences from the integration of field data with numerically balanced geological cross section. Tectonics, 35(6), 1404-1422. https://doi.org/10.1002/2015TC004004.

Bai, T., & Pollard, D. D. (2000a). Fracture spacing in layered rocks: a new explanation based on the stress transition. Journal of Structural Geology, 22(1), 43-57. https://doi.org/10.1016/S0191-8141(99)00137-6

Bai, T., & Pollard, D. D. (2000b). Closely spaced fractures in layered rocks: initiation mechanism and propagation kinematics. Journal of Structural Geology, 22(10), 1409-1425. https://doi.org/10.1016/S0191-8141(00)00062-6

Barr, A. C. (2008). Mobile lid convection beneath Enceladus' south polar terrain. Journal of Geophysical Research: Planets, 113(E7). https://doi.org/10.1029/2008JE003114

Barr, A. C., & Preuss, L. J. (2010). On the origin of south polar folds on Enceladus. Icarus, 208(1), 499-503. https://doi.org/10.1016/j.icarus.2010.03.038

Becker, T., Archinal, B., Colvin, T., Davies, M., Gitlin, A., Kirk, R. L., & Weller, L. (2001). Final digital global maps of Ganymede, Europa, and Callisto. In Lunar and Planetary Science Conference, 32.

Bedle, H., Jurdy, D.M. (2005). Ganymede's sulci on global and regional scales. Lunar and Planetary Science XXXVI, 1161.

Bennett, M. R., Huddart, D., & Waller, R. I. (2000). Glaciofluvial crevasse and conduit fills as indicators of supraglacial dewatering during a surge, Skeiðarárjökull, Iceland. Journal of Glaciology, 46(152), 25-34. https://doi.org/10.3189/172756500781833232.

Berquin, Y., Kofman, W., Herique, A., Alberti, G., Beck, P. (2013). A study on Ganymede's surface topography: Perspectives for radar sounding. Planetary andSpaceScience77, 40–44. http://dx.doi.org/10.1016/j.pss.2012.07.004.

Beuthe, M. (2016). Crustal control of dissipative ocean tides in Enceladus and other icy moons. Icarus, 280, 278-299. https://doi.org/10.1016/j.icarus.2016.08.009

Bianchi, R., Casacchia, R., Pozio, S. (1984). Tectonics of the grooved terrain on Ganymede. Lunar and Planetary Science Conference 15, 54-55.

Bianchi, R., Casacchia, R., Lanciano, P., Pozio, S., Strom, R.G., 1986. Tectonic framework of grooved terrain on Ganymede. Icarus 67 (2), 237–250. https://doi.org/10.1016/0019-1035(86)90106-5.

Bingham, R. G., & Siegert, M. J. (2007). Radio-echo sounding over polar ice masses. Journal of Environmental and Engineering Geophysics, 12(1), 47-62. https://doi.org/10.2113/JEEG12.1.47.

Bland, M.T., Showman, A.P., 2007. The formation of Ganymede's grooved terrain: numerical modeling of extensional necking instabilities. Icarus 189 (2), 439–456. https://doi.org/10.1016/j.icarus.2007.01.012

Bland, M.T., Showman, A.P., Tobie, G., 2009. The orbital–thermal evolution and global expansion of Ganymede. Icarus 200 (1), 207–221. https://doi.org/10.1016/j.icarus.2008.11.016.

Bland, M. T., Becker, T. L., Edmundson, K. L., Roatsch, T., Archinal, B. A., Takir, D., et al. (2018). A new Enceladus global control network, image mosaic, and updated pointing kernels from Cassini's 13-year mission. Earth and Space Science, 5, 604– 621. https://doi.org/10.1029/2018EA000399

Blankenship, D. D., S. D. Kempf, D. A. Young, T. G. Richter, D. M. Schroeder, J. S. Greenbaum, T. van Ommen, R. C. Warner, J. L. Roberts, N. W. Young, E. Lemeur, M. J. Siegert, and J. W. Holt. 2017. IceBridge HiCARS 1 L1B Time-Tagged Echo Strength Profiles, Version 1. [Indicate subset used]. Boulder, Colorado USA. NASA National Snow and Ice Data Center Distributed Active Archive Center. doi: https://doi.org/10.5067/W2KXX0MYNJ9G.

Blasius, K. R., Cutts, J. A., & Howard, A. D. (1982). Topography and stratigraphy of Martian polar layered deposits. Icarus, 50(2-3), 140-160. https://doi.org/10.1016/0019-1035(82)90122-1.

Blumsack, S.L., Gierasch, P. J., Wessel, W. R. (1973). An analytical and numerical study of the Martian planetary boundary layer over slopes. Journal of Atmospheric Sciences 30,66–82. https://doi.org/10.1175/1520-0469(1973)030<0066:AAANSO>2.0.CO;2.

Bosworth, W., 1994. A model for the three-dimensional evolution of continental rift basins, northeast Africa. Geologische Rundschau, 83, 671–688. Coney, P. J., 1980. Cordilleran metamorphic core complexes: An overview. Geological Society of America Memoir, 153, 7–31. https://doi.org/10.1007/BF00251067.

Bramson, A. M., Byrne, S., Bapst, J., Smith, I. B., & McClintock, T. (2019). A Migration Model for the Polar Spiral Troughs of Mars. Journal of Geophysical Research: Planets, 124(4), 1020-1043. https://doi.org/10.1029/2018JE005806.

Bromwich, D. H., Parish, T. R., & Zorman, C. A. (1990). The confluence zone of the intense katabatic winds at Terra Nova Bay, Antarctica, as derived from airborne sastrugi surveys and mesoscale numerical modeling. Journal of Geophysical Research: Atmospheres, 95(D5), 5495-5509. https://doi.org/10.1029/JD095iD05p05495.

Brothers, T. c., Holt, J. W., Spiga, A. (2015). Planum Boreum basal unit topography, Mars: Irregularities and insights from SHARAD. JGR Planets. https://doi.org/10.1002/2015JE004830.

Bruzzone, L., Plaut, J.J., Alberti, G., Blankenship, D.D., Bovolo, F., Campbell, B.A., Ferro, A., Gim, Y., Kofman, W., Komatsu, G., McKinnon, W., Mitri, G., Orosei, R., Patterson, G.W., Plettemeier, D., Seu, R. (2013). RIME: Radar for icy moon exploration. In 2013 IEEE International Geoscience and Remote Sensing Symposium-IGARSS, 3907-3910. https://doi.org/10.1109/IGARSS.2013.6723686.

Budd, W. F., Jenssen, D., Leach, J. H. I., Smith, I. N., & Radok, U. (1986). The north polar ice cap of Mars as a steady-state system. Polarforschung, 56(1/2), 43-63.

Čadek, O., Souček, O., Běhounková, M., Choblet, G., Tobie, G., & Hron, J. (2019). Long-term stability of Enceladus' uneven ice shell. Icarus, 319, 476-484. https://doi.org/10.1016/j.icarus.2018.10.003.

Čadek, O., Tobie, G., Van Hoolst, T., Massé, M., Choblet, G., Lefèvre, A., et al. (2016). Enceladus's internal ocean and ice shell constrained from Cassini gravity, shape, and libration data. Geophysical Research Letters, 43(11), 5653-5660. https://doi.org/10.1002/2016GL068634

Cameron, M.E., Smith-Konter, B.R., Pappalardo, R.T., Collins, G., Nimmo, F., 2013. Tidally-driven strike-slip failure mechanics on Ganymede. In: Lunar and Planetary Science Conference. Technical Report 44. Lunar and Planetary Institute, pp. 2711.

Cameron, M.E., Smith-Konter, B.R., Burkhard, L., Pappalardo, R.T., Collins, G.C., 2016. Strike-slip faulting on Ganymede: morphological mapping and failure mechanics. In: Lunar and Planetary Science Conference. 47. pp. 2630.

Cameron, M.E., Smith-Konter, B.R., Burkhard, L., Collins, G.C., Seifert, F., Pappalardo, R.T. (2018). Morphological mapping of Ganymede: Investigating the role of strike-slip tectonics in the evolution of terrain types. Icarus 315, 92–114. https://doi.org/10.1016/j.icarus.2018.06.024.

Carr, J. R. (1996). Spectral and textural classification of single and multiple band digital images. Computers & Geosciences, 22(8), 849-865. https://doi.org/10.1016/S0098-3004(96)00025-8

Carr, M.H., Belton, M.J.S., Chapman, C.R., Davies, M.E., Geissler, P., Greenberg, R., McEwen, A.S., Tufts, B.R., Greeley, R., Sullivan, R., Head, J.W., Pappalardo, R.T., Klaasen, K.P., Johnson, T.V., Kaufman, J., Senske, D., Moore, J., Neukum, G., Schubert, G., Burns, J.A., Thomas, P., Veverka, J. (1998). Evidence for a subsurface ocean on Europa. Nature 391 (6665), 363–365. https://doi.org/10.1038/34857.

Casacchia, R., Strom, R.G., 1984. Geologic evolution of Galileo Regio, Ganymede. J. Geophys. Res. Solid Earth 89 (S02). https://doi.org/10.1029/JB089iS02p0B419.

Castaldo, L., Mège, D., Gurgurewicz, J., Orosei, R., & Alberti, G. (2017). Global permittivity mapping of the Martian surface from SHARAD. Earth and Planetary Science Letters, 462, 55-65. https://doi.org/10.1016/j.epsl.2017.01.012.

Chamberlin, R. T. (1936). Glacier movement as typical rock deformation. The Journal of Geology, 44(1), 93-104. https://doi.org/10.1086/624399.

Childs, C., Nicol, A., Walsh, J. J. and Watterson, J. (2003). The growth and propagation of synsedimentary faults. Journal of Structural Geology 25: 633–648. https://doi.org/10.1016/S0191-8141(02)00054-8.

Choblet, G., Tobie, G., Sotin, C., Běhounková, M., Čadek, O., Postberg, F., & Souček, O. (2017). Powering prolonged hydrothermal activity inside Enceladus. Nature Astronomy, 1(12), 841. https://doi.org/10.1038/s41550-017-0289-8

Choblet, G., Sotin, C., Tobie, G., Postberg, F., Čadek, O., Bouffard, M., et al. (2018). The interior of Enceladus just after Cassini. In 42nd COSPAR Scientific Assembly (Vol. 42).

Christensen, P. R., Engle, E., Anwar, S., Dickenshied, S., Noss, D., Gorelick, N., & Weiss-Malik, M. (2009, December). JMARS-a planetary GIS. In AGU Fall Meeting Abstracts.

Cianfarra, P., A. Forieri, F. Salvini, I. E. Tabacco, and A. Zirizotti (2009), Geological setting of the Concordia trench-lake system in East Antarctica, Geophys. J. Int., 177(3), 1305–1314. https://doi.org/10.1111/j.1365-246X.2009.04123.x.

Cianfarra, P., Salvini, F., 2014. Ice sheet surface lineaments as nonconventional indicators of East Antarctica bedrock tectonics. Geosphere 10 (6), 1411–1418. https://doi.org/10.1130/GES01074.1.

Cianfarra, P., Salvini, F., 2015. Lineament domain of regional strike-slip corridor: insight from the Neogene transtensional De Geer transform fault in NW Spitsbergen. Pure Appl. Geophys. 172 (5), 1185–1201. https://doi.org/10.1007/s00024-014-0869-9.

Cianfarra, P., Salvini, F., 2016a. Quantification of fracturing within fault damage zones affecting late Proterozoic carbonates in Svalbard. Rendiconti Lincei 27 (1), 229–241. https://doi.org/10.1007/s12210-016-0527-5.

Cianfarra, P., Salvini, F., 2016b. Origin of the adventure subglacial trench linked to Cenozoic extension in the East Antarctic Craton. Tectonophysics 670, 30–37. https://doi.org/10.1016/j.tecto.2015.12.011.

Cianfarra, P., Maggi, M. (2017). Cenozoic extension along the reactivated Aurora Fault System in the East Antarctic Craton. Tectonophysics 703, 135-143. https://doi.org/10.1016/j.tecto.2017.02.019.

Clarke, T. S., & Bentley, C. R. (1994). High-resolution radar on Ice Stream B2, Antarctica: measurements of electromagnetic wave speed in firn and strain history from buried crevasses. Annals of Glaciology, 20, 153-159. https://doi.org/10.3189/1994AoG20-1-153-159.

Clifford, S. M. (1987). Polar basal melting on Mars. Journal of Geophysical Research: Solid Earth, 92(B9), 9135-9152. https://doi.org/10.1029/JB092iB09p09135.

Colgan, W., Rajaram, H., Abdalati, W., McCutchan, C., Mottram, R., Moussavi, M. S., & Grigsby, S. (2016). Glacier crevasses: Observations, models, and mass balance implications. Reviews of Geophysics, 54(1), 119-161. https://doi.org/10.1002/2015RG000504.

Collins, G.C., Head III, J.W., Pappalardo, R.T., 1998. The role of extensional instability in creating Ganymede grooved terrain: insights from Galileo high-resolution stereo imaging. Geophys. Res. Lett. 25 (3), 233–236. https://doi.org/10.1029/97GL03772.

Collins, G. C., Head, J. W., Pappalardo, R. T., & Galileo SSI Team. (2000). A global database of grooves and dark terrain on Ganymede, enabling quantitative assessment of terrain features. In Lunar and Planetary Science Conference, 31.

Collins, G. C., & Goodman, J. C. (2007). Enceladus' south polar sea. Icarus, 189(1), 72-82. https://doi.org/10.1016/j.icarus.2007.01.010.

Collins, G. C. (2009). The origin of grooved terrain on Ganymede. European Planetary Science Congress, 4, 516.

Collins, G. C., McKinnon, W. B., Moore, J. M., Nimmo, F., Pappalardo, R. T., Prockter, L. M., & Schenk, P. M. (2009). Tectonics of the outer planet satellites. Planetary Tectonics, 11(264), 229.

Collins, G. C., Patterson, G. W., Head, J. W., Prockter, L., Pappalardo, R. T., Lucchitta, B. K., & Kay, J. P. (2013). Global geologic map of Ganymede. US Department of the Interior, US Geological Survey. https://dx.doi.org/10.3133/sim3237.

Cox, S. F. (2010). The application of failure mode diagrams for exploring the roles of fluid pressure and stress states in controlling styles of fracture-controlled permeability enhancement in faults and shear zones. Geofluids, 10(1-2), 217-233. https://doi.org/10.1111/j.1468-8123.2010.00281.x.

Cremonese, G., Lucchetti, A., Simioni, E., 2016. New global maps of Europa's lineaments. In: AAS/Division for Planetary Sciences Meeting Abstracts. 48.

Crow-Willard, E. N., & Pappalardo, R. T. (2015). Structural mapping of Enceladus and implications for formation of tectonized regions. Journal of Geophysical Research: Planets, 120(5), 928-950. https://doi.org/10.1002/2015JE004818

Cutts, J. A. (1973). Nature and origin of layered deposits of the Martian polar regions, J. Geophys. Res., 78(20), 4231-4249. https://doi.org/10.1029/JB078i020p04231.

Cutts, J. A., Blasius, K. R., & Roberts, W. J. (1979). Evolution of Martian polar landscapes: Interplay of long-term variations in perennial ice cover and dust storm intensity. Journal of Geophysical Research: Solid Earth, 84(B6), 2975-2994. https://doi.org/10.1029/JB084iB06p02975.

Das, S. B., Joughin, I., Behn, M. D., Howat, I. M., King, M. A., Lizarralde, D., & Bhatia, M. P. (2008). Fracture propagation to the base of the Greenland Ice Sheet during supraglacial lake drainage. Science, 320(5877), 778-781. https://doi.org/10.1126/science.1153360.

Davison, I. (1986). Listric normal fault profiles: calculation using bed-length balance and fault displacement. Journal of Structural Geology, 8(2), 209-210. https://doi.org/10.1016/0191-8141(86)90112-4.

Deschamps, F., Sotin, C., 2001. Thermal convection in the outer shell of large icy satellites. J. Geophys. Res. Planets 106 (E3), 5107–5121. https://doi.org/10.1029/2000JE001253.

Dombard, A.J., McKinnon, W.B., 2001. Formation of grooved terrain on Ganymede: extensional instability mediated by cold, superplastic creep. Icarus 154 (2), 321–336. https://doi.org/10.1006/icar.2001.6728.

Dougherty, M., Esposito, L., & Krimigis, S. (Eds.). (2009). Saturn from Cassini-huygens. Springer Science & Business Media.

Drewry, D. J., Jordan, S. R., & Jankowski, E. (1982). Measured properties of the Antarctic ice sheet: surface configuration, ice thickness, volume and bedrock characteristics. Annals of Glaciology, 3, 83-91. https://doi.org/10.3189/S0260305500002573.

Duval, B., Cramez, C. and Jackson, M. P. A., 1992, Raft tectonics in the Kwanza Basin, Angola. Marine and Petroleum Geology 9: 389–390. https://doi.org/10.1016/0264-8172(92)90050-O.

Dzurisin, D., & Blasius, K. R. (1975). Topography of the polar layered deposits of Mars. Journal of Geophysical Research, 80(23), 3286-3306. https://doi.org/10.1029/JB080i023p03286.

Edgett, K. S., Williams, R. M., Malin, M. C., Cantor, B. A., & Thomas, P. C. (2003). Mars landscape evolution: Influence of stratigraphy on geomorphology in the north polar region. Geomorphology, 52(3-4), 289-297. https://doi.org/10.1016/S0169-555X(02)00262-3.

Emetc, V., Tregoning, P., Morlighem, M., Borstad, C., & Sambridge, M. (2018). A statistical fracture model for Antarctic ice shelves and glaciers. https://doi.org/10.5194/tc-12-3187-2018.

von Engeln, O. D. (1934). The Motion of Glaciers. Science, 80(2079), 401-403.

Fanale, F. P., Johnson, T. V., Matson, D. L. (1977). Io's surface and the histories of the Galilean satellites. In IAU Colloq. 28: Planetary Satellites, pp. 379-405.

Fern, C. J., & Warner, T. A. (2002). Scale and texture in digital image classification. Photogrammetric Engineering & Remote Sensing, 68(1), 51-63.

Filacchione, G., D'Aversa, E., Capaccioni, F., Clark, R. N., Cruikshank, D. P., Ciarniello, M., et al. (2016). Saturn's icy satellites investigated by Cassini-VIMS. IV. Daytime temperature maps. Icarus, 271, 292-313. http://dx.doi.org/10.1016/j.icarus.2016.02.019.

Fimmel, R.O., Van Allen, J., Burgess, E. (1980). Pioneer: first to Jupiter, Saturn, and beyond. NASA Special Publication 446.

Fink, J.H., Fletcher, R.C., 1981. A mechanical analysis of extensional instability on Ganymede. In: Reports of Planetary Geology Program, pp. 51–53.

Fisher, D. A. (2000). Internal layers in an "accublation" ice cap: A test for flow. Icarus, 144(2), 289-294. https://doi.org/10.1006/icar.1999.6293.

Fisher, D. A., Winebrenner, D. P., & Stern, H. (2002). Lineations on the "white" accumulation areas of the residual northern ice cap of Mars: Their relation to the "accublation" and ice flow hypothesis. Icarus, 159(1), 39-52. https://doi.org/10.1006/icar.2002.6877.

Fortuin, J. P. F., & Oerlemans, J. (1990). Parameterization of the annual surface temperature and mass balance of Antarctica. Annals of Glaciology, 14, 78-84. https://doi.org/10.3189/S0260305500008302.

Fossen, H., 2010. Structural Geology. Cambridge University Press, Cambridge, UK (463 pp.).

Freers T.F. 1968. Crevasse. In: Geomorphology. Encyclopedia of Earth Science. Springer, Berlin, Heidelberg.

Fretwell, P., Pritchard H. D., Vaughan D. G, Bamber J. L., Barrand N. E., Bell R., Bianchi C., Bingham R. G., Blankenship D. D, Casassa D., Catania D., Callens D., Conway H., Cook A. J., H. F. J. Corr, D. Damaske, V., Damm, F. Ferraccioli, R. Forsberg, S. Fujita, Y. Gim, P. Gogineni, J. A., Griggs, R. C. A. Hindmarsh, P. Holmlund, J. W. Holt, R. W. Jacobel, A., Jenkins, W. Jokat, T., Jordan, E. C. King, J. Kohler, W. Krabill, M. RigerKusk, K. A. Langley, G. Leitchenkov, C., Leuschen, B. P. Luyendyk, K., Matsuoka, J. Mouginot, F. O. Nitsche, Y. Nogi, O. A. Nost, S. V. Popov, E. Rignot, D. M. Rippin, A. Rivera, J. Roberts, N. Ross, M. J. Siegert, A. M. Smith, D. Steinhage, M. Studinger, B. Sun, B. K. Tinto, B. C., Welch, D. Wilson, D. A. Young, C. Xiangbin, and A. Zirizzotti, 2013, Bedmap2: Improved ice bed, surface, and thickness datasets for Antarctica: The Cryosphere, 7, 375–393. https://doi.org/10.5194/tc-7-375-2013.

Frezzotti, M., Pourchet, M., Flora, O., Gandolfi, S., Gay, M., Urbini, S., ... & Severi, M. (2004). New estimations of precipitation and surface sublimation in East Antarctica from snow accumulation measurements. Climate Dynamics, 23(7-8), 803-813.

Frezzotti, M., Gandolfi, S., & Urbini, S. (2002). Snow megadunes in Antarctica: Sedimentary structure and genesis. Journal of Geophysical Research: Atmospheres, 107(D18), ACL-1. https://doi.org/10.1029/2001JD000673.

Gabrielsen, R.H., Braathen, A., 2014. Models of fracture lineaments - joint swarms, fracture corridors and faults in crystalline rocks, and their genetic relations. Tectonophysics 628, 26–44. https://doi.org/10.1016/j.tecto.2014.04.022.

Gaddis, L., Anderson, J., Becker, K., Becker, T., Cook, D., Edwards, K., Eliason, E., Hare, T., Kieffer, H., Lee, E.M., Mathews, J., Soderblom, L., Sucharski, T., Torson, J., 1997. An overview of the integrated software for imaging spectrometers (ISIS). In: Lunar and Planetary Science Conference. 28. pp. 387.

Gibbs, A.D., 1984, Structural evolution of extensional basin margins. Journal of the Geological Society 141: 609–620. https://doi.org/10.1144/gsjgs.141.4.0609.

Giese, B., Wagner, R., Neukum, G., Pappalardo, R.T., Head, J.W., and the Galileo SSI Team (2001). The topography of Ganymede's Arbela Sulcus. Lunar and Planetary Science XXXII, 1743.

Gioia, G., Chakraborty, P., Marshak, S., & Kieffer, S. W. (2007). Unified model of tectonics and heat transport in a frigid Enceladus. Proceedings of the National Academy of Sciences, 104(34), 13578-13581. https://doi.org/10.1073/pnas.0706018104.

Giordano, G., Pinton, A., Cianfarra, P., Baez, W., Chiodi, A., Viramonte, J., Norini, G., Groppelli, G., 2013. Structural control on geothermal circulation on the Cerro Tuzgle-Tocomar geothermal volcanic area (Puna plateau, Argentina). J. Volcanol. Geotherm. Res. 249, 77–94. https://doi.org/10.1016/j.jvolgeores.2012.09.009.

Golombek, M.P., 1982. Constraints on the expansion of Ganymede and the thickness of the lithosphere. J. Geophys. Res. Solid Earth 87 (S01), A77–A83. https://doi.org/10.1029/JB087iS01p00A77.

Grasset, O., Dougherty, M.K., Coustenis, A., Bunce, E.J., Erd, C., Titov, D., Blanc, M., Coates, A., Drossart, P., Fletcher, L.N:, Hussmann, H., Jaumann, R., Krupp, N., Lebreton, JP., Prieto-Ballesteros, O., Tortora, P., Tosi, F., Van Hoolst, T. (2013). Jupiter Icy moons Explorer (JUICE): An ESA mission to orbit Ganymede and to characterise the Jupiter system. Planetary and Space Science 78, 1-21. https://doi.org/10.1016/j.pss.2012.12.002.

Grima, C., Kofman, W., Mouginot, J., Phillips, R. J., Hérique, A., Biccari, D., ... & Cutigni, M. (2009). North polar deposits of Mars: Extreme purity of the water ice. Geophysical Research Letters, 36(3). https://doi.org/10.1029/2008GL036326.

Grima, C., Costard, F., Kofman, W., Saint-Bézar, B., Servain, A., Rémy, F., ... & Seu, R. (2011). Large asymmetric polar scarps on Planum Australe, Mars: Characterization and evolution. Icarus, 212(1), 96-109. https://doi.org/10.1016/j.icarus.2010.12.017.

Hambrey, M. J., & Müller, F. (1978). Structures and ice deformation in the white glacier, Axel Heiberg Island, Northwest Territories, Canada. Journal of Glaciology, 20(82), 41-66. https://doi.org/10.3189/S0022143000021213.

Hammond, N.P., Barr, A.C. (2014). Formation of Ganymede’s grooved terrain by convection-driven resurfacing. Icarus 227, 206-209. https://doi.org/10.1016/j.icarus.2013.08.024.

Hansen, C. J., Esposito, L., Stewart, A. I. F., Colwell, J., Hendrix, A., Pryor, W., et al. (2006). Enceladus' Water Vapor Plume. Science, 311(57669), 1422-1425. https://doi.org/10.1126/science.1121254.

Harding, T.P., 1974. Petroleum traps associated with wrench faults. AAPG Bull. 58 (7), 1290–1304.

Hargitai, H., Kereszturi, Á., 2015. Encyclopedia of Planetary Landforms. Springer, New York. https://doi.org/10.1007/978-1-4614-9213-9.

Harris, L., Milici, R. (1977). Characteristics of Thin-Skinned Style of Deformation in the Southern Appalachians, and Potential Hydrocarbon Traps. Geological Survey Professional Paper, 1018.

Hartmann, W.K., 1980. Surface evolution of two-component stone/ice bodies in the Jupiter region. Icarus 44 (2), 441–453. https://doi.org/10.1016/0019-1035(80)90036-6.

Head, J.W., Pappalardo, R.T., Collins, G.C., Belton, M.J.S., Giese, B., Wagner, R., Breneman, H., Spaun, N., Nixon, B., Neukum, G., Moore, J. (2002). Evidence for Europa-like tectonic resurfacing styles on Ganymede. Geophysical Research Letters 29 (24), 2151. https://doi.org/10.1029/2002GL015961.

Helfenstein, P., Veverka, J., Denk, T., Neukum, G., Head, J. W., Pappalardo, R. T., and the Galileo Imaging Team (1997). Dark-floor craters: Galileo constraints on a Ganymede regolith component. Lunar and Planetary Science XXVIII. 547-548.

Helfenstein, P., & Porco, C. C. (2015). Enceladus' geysers: relation to geological features. The Astronomical Journal, 150(3), 96. https://doi.org/10.1088/0004-6256/150/3/96.

Hendrix, A. R., Hansen, C. J., & Holsclaw, G. M. (2010). The ultraviolet reflectance of Enceladus: Implications for surface composition. Icarus, 206(2), 608-617. https://doi.org/10.1016/j.icarus.2009.11.007.

Herny, C., Massé, M., Bourgeois, O., Carpy, S., Le Mouélic, S., Appéré, T., ... & Rodriguez, S. (2014). Sedimentation waves on the Martian North Polar Cap: analogy with megadunes in Antarctica. Earth and Planetary Science Letters, 403, 56-66. https://doi.org/10.1016/j.epsl.2014.06.033.

Herrick, D.L., Stevenson, D.J., 1990. Extensional and compressional instabilities in icy satellite lithospheres. Icarus 85 (1), 191–204. https://doi.org/10.1016/0019-1035(90)90110-U.

Hickman, S., Zoback, M., Ellsworth, W., Boness, N., Malin, P., Roecker, S., Thurber, C. 2007. Structure and Properties of the San Andreas Fault in Central California: Recent Results from the SAFOD Experiment, Sci. Dril., SpecialIssue, 29–32, https://doi.org/10.2204/iodp.sd.s01.39.2007.

Hillgren, V.J., Melosh, H.J., 1989. Crater relaxation on Ganymede: implications for ice rheology. Geophys. Res. Lett. 16 (11), 1339–1342. https://doi.org/10.1029/GL016i011p01339.

Howard, A. D. 1978. Origin of the stepped topography of the martian poles. Icarus 34, 581–599. https://doi.org/10.1016/0019-1035(78)90047-7.

Howard, A. D., Cutts, J. A., & Blasius, K. R. (1982). Stratigraphic relationships within Martian polar cap deposits. Icarus, 50(2-3), 161-215. https://doi.org/10.1016/0019-1035(82)90123-3.

Howard, A. D. (2000). The role of eolian processes in forming surface features of the Martian polar layered deposits. Icarus, 144(2), 267-288. https://doi.org/10.1006/icar.1999.6305.

Hsu, H. W., Postberg, F., Sekine, Y., Shibuya, T., Kempf, S., Hora´nyi, M., et al. (2015). Ongoing hydrothermal activities within Enceladus, Nature, 519, 207–210. https://doi.org/10.1038/nature14262.

Hussmann, H., Sotin, C., Lunine, J.I., 2007. Interiors and evolution of icy satellites. In: Spohn, T., Schubert, G. (Eds.), Treatise on Geophysics. 10. Elsevier, pp. 509–539.

Iess, L., Stevenson, D. J., Parisi, M., Hemingway, D., Jacobson, R. A., Lunine, J. I., & Tortora, P. (2014). The gravity field and interior structure of Enceladus. Science, 344(6179), 78-80. https://doi.org/10.1126/science.1250551.

Ilyushin, Y. A., Orosei, R., Witasse, O., & Sánchez-Cano, B. (2017). CLUSIM: A synthetic aperture radar clutter simulator for planetary exploration. Radio Science, 52(9), 1200-1213. https://doi.org/10.1002/2017RS006265.

Jaumann, R., Clark, R.N., Nimmo, F., Hendrix, A.R., Buratti, B.J., Denk, T., Moore, J.M., Schenk, P.M., Ostro, S.J., Srama, R. (2009). Icy Satellites: Geological Evolution and Surface Processes. In: Saturn from Cassini-Huygens, 637-682. Springer, Dordrecht.

Jezek, K. C., & Bentley, C. R. (1983). Field studies of bottom crevasses in the Ross Ice Shelf, Antarctica. Journal of Glaciology, 29(101), 118-126. https://doi.org/10.3189/S0022143000005189.

Johnston, S. A., & Montési, L. G. (2017). The impact of a pressurized regional sea or global ocean on stresses on Enceladus. Journal of Geophysical Research: Planets, 122(6), 1258-1275. https://doi.org/10.1002/2016JE005217

Jones, W. B. (1988). Listric growth faults in the Kenya Rift Valley. Journal of structural geology, 10(7), 661-672. https://doi.org/10.1016/0191-8141(88)90074-0.

Jones, K.B., Head III, J.W., Pappalardo, R.T., Moore, J.M., 2003. Morphology and origin of palimpsests on Ganymede based on Galileo observations. Icarus 164 (1), 197–212. https://doi.org/10.1016/S0019-1035(03)00128-3.

Jordan, G., Schott, B., 2005. Application of wavelet analysis to the study of spatial pattern of morphotectonic lineaments in digital terrain models. A case study. Remote Sens. Environ. 94 (1), 31–38. https://doi.org/10.1016/j.rse.2004.08.013.

Kattenhorn, S. A., & Prockter, L. M. (2014). Evidence for subduction in the ice shell of Europa. Nature Geoscience, 7(10), 762. https://doi.org/10.1038/ngeo2245.

Kay, J., Schenk, P., Prockter, L., (2019). Triton, Europa, Enceladus & Pluto, oh my!: Topography of active icy ocean worlds. Lunar and Planetary Science Conference, 50.

Khurana, K. K., Kivelson, M. G., Stevenson, D. J., Schubert, G., Russell, C. T., Walker, R. J., & Polanskey, C. (1998). Induced magnetic fields as evidence for subsurface oceans in Europa and Callisto. Nature, 395(6704), 777. https://doi.org/10.1038/27394.

Kirk, R. L., Stevenson, D. J. (1987). Thermal evolution of a differentiated Ganymede and implications for surface features. Icarus, 69 (1), 91-134. https://doi.org/10.1016/0019-1035(87)90009-1.

Kivelson, M.G., Khurana, K.K., Russell, C.T., Volwerk, M., Walker, R.J., Zimmer, C. (2000). Galileo magnetometer measurements: A stronger case for a subsurface ocean at Europa. Science 289 (5483), 1340–1343. https://doi.org/10.1126/science.289.5483.1340.

Kivelson, M.G., Khurana, K.K., Volwerk, M., 2002. The permanent and inductive magnetic moments of Ganymede. Icarus 157, 507–522. https://doi.org/10.1006/icar.2002.6834.

Knowles, B. (2016). Cassini Imaging Science Subsystem (ISS) Data User's Guide. Cassini Imaging Central Laboratory for Operations (CICLOPS), Space Science Institute.

Kostic, S., & Smith, I. B. (2018). Water on Mars: Do submarine cyclic steps exist on the red planet?. Progress in Earth and Planetary Science, 5(1), 76. https://doi.org/10.1186/s40645-018-0225-2.

Kreslavsky, M., Head, J., 2000. Kilometer-scale roughness of Mars: Results from MOLA data analysis. J. Geophys. Res. 105, 26695–26711. https://doi.org/10.1029/2000JE001259.

Kuiper, G. P. (1952). Planetary atmospheres and their origins. In Kuiper, G. P. (ed.) Atmospheres of the Earth and planets, pp. 306{405. University of Chicago Press.

Lachenbruch, A. H. (1961). Depth and spacing of tension cracks. Journal of Geophysical Research, 66(12), 4273-4292. https://doi.org/10.1029/JZ066i012p04273.

Lankreijer, A., Kovac, M., Cloetingh, S., Pitonak, P., Hloska, M., Biermann, C. (1995). Quantitative subsidence analysis and forward modelling of the Vienna and Danube basins: thin-skinned versus thick-skinned extension. Tectonophysics 252, 433-451. https://doi.org/10.1016/0040-1951(95)00099-2.

Lawson, W. J., Sharp, M. J., & Hambrey, M. J. (1994). The structural geology of a surge-type glacier. Journal of Structural Geology, 16(10), 1447-1462. https://doi.org/10.1016/0191-8141(94)90008-6.

Le Gall, A., Leyrat, C., Janssen, M. A., Choblet, G., Tobie, G., Bourgeois, O., et al. (2017). Thermally anomalous features in the subsurface of Enceladus's south polar terrain. Nature Astronomy, 1(4), 0063. https://doi.org/10.1038/s41550-017-0063.

Lewis, S. R., Collins, M., Read, P. L., Forget, F., Hourdin, F., Fournier, R., ... & Huot, J. P. (1999). A climate database for Mars. Journal of Geophysical Research: Planets, 104(E10), 24177-24194. https://doi.org/10.1029/1999JE001024.

Lianchong, L., Shaohua L., & Chun'an, T. (2014). Fracture spacing behavior in layered rocks subjected to different driving forces: a numerical study based on fracture infilling process. Frontiers of earth science 8(4), 472-489. https://doi.org/10.1007/s11707-014-0427-x.

Lucchetti, A., Pozzobon, R., Mazzarini, F., Cremonese, G., Massironi, M. (2017). Brittle ice shell thickness of Enceladus from fracture distribution analysis. Icarus 297, 252–264. http://dx.doi.org/10.1016/j.icarus.2017.07.009.

Lucchitta, B.K., 1980. Grooved terrain on Ganymede. Icarus 44 (2), 481–501. https://doi.org/10.1016/0019-1035(80)90039-1.

Lucchitta, B.K., McEwen, A.S., Clow, G.D., Geissler, P.E., Singer, R.B., Schultz, R.A., Squyres, S.W., Mars, H., 1992. In: Kieffer, H. (Ed.), The canyon system on Mars. Univ. of Arizona, Tucson, pp. 453–492.

Lucianetti, G., Cianfarra, P., Mazza, R., 2017. Lineament domain analysis to infer groundwater flow paths: clues from the Pale di San Martino fractured aquifer, Eastern Italian Alps. Geosphere 13 (5), 1729–1746. https://doi.org/10.1130/GES01500.1.

Lundin, E.R. (1992). Thin-skinned extensional tectonics on a salt detachment, northern Kwanza Basin, Angola. https://doi.org/10.1016/0264-8172(92)90051-F.

Maggi, M., Cianfarra, P., Salvini, F., de Lima, C.C., 2015. Staircase fractures in microbialites and the role of lamination-related mechanical anisotropy: the example of the acquasanta terme travertine deposits (central Italy). Geol. Soc. Am. Bull. 127 (5–6), 879–896. https://doi.org/10.1130/B31163.1.

Maggi, M., Cianfarra, P., Salvini, F. (2016). Erosion by tectonic carving in the Concordia subglacial fault zone, East Antarctica. Earth and Planetary Science Letters 433, 99-108. https://doi.org/10.1016/j.epsl.2015.10.045.

Mahrt, L. (1982). Momentum balance of gravity flows. J. Atmos. Sci. 39 (12), 2701–2711. https://doi.org/10.1175/1520-0469(1982)039<2701:MBOGF>2.0.CO;2.

Martin, E. S. (2016). The distribution and characterization of strike-slip faults on Enceladus. Geophysical Research Letters, 43(6), 2456-2464. https://doi.org/10.1002/2016GL067805.

Masoud, A.A., Koike, K., 2011. Morphotectonics inferred from the analysis of topographic lineaments auto-detected from DEMs: application and validation for the Sinai Peninsula, Egypt. Tectonophysics 510 (3–4), 291–308. https://doi.org/10.1016/j.tecto.2011.07.010.

Massé, M., Bourgeois, O., Le Mouélic, S., Verpoorter, C., Spiga, A., & Le Deit, L. (2012). Wide distribution and glacial origin of polar gypsum on Mars. Earth and Planetary Science Letters, 317, 44-55. https://doi.org/10.1016/j.epsl.2011.11.035.

Matson, D.L., Spilker, L.J., Lebreton, JP. (2003). The Cassini-Huygens mission to the Saturnian system. the cassini Huygens mission, 1-58. https://doi.org/10.1007/978-94-017-3251-2_1.

Matson, D. L., Castillo, J. C., Lunine, J., & Johnson, T. V. (2007). Enceladus' plume: Compositional evidence for a hot interior. Icarus, 187(2), 569-573. https://doi.org/10.1016/j.icarus.2006.10.016.

Matsuyama, I., & Nimmo, F. (2008). Tectonic patterns on reoriented and despun planetary bodies. Icarus, 195(1), 459-473. https://doi.org/10.1016/j.icarus.2007.12.003.

Matsuyama, I., Nimmo, F., Mitrovica, J.X. (2014). Planetary Reorientation. Annual Review of Earth and Planetary Sciences 42, 605-34. https://doi.org/10.1146/annurev-earth-060313-054724.

Mazzarini, F., & Salvini, F. (1994). Tectonic blocks in northern Victoria Land (Antarctica): Geological and structural constraints by satellite lineament domain analysis. Terra Antartica, 1(1), 74-77.

McKenzie, D., & Jackson, J. (1986). A block model of distributed deformation by faulting. Journal of the Geological Society, 143(2), 349-353. https://doi.org/10.1144/gsjgs.143.2.0349.

McKinnon, W.B., Melosh, H.J., 1980. Evolution of planetary lithospheres: evidence from multiringed structures on Ganymede and Callisto. Icarus 44 (2), 454–471. https://doi.org/10.1016/0019-1035(80)90037-8.

McKinnon, W. B. (2015). Effect of Enceladus's rapid synchronous spin on interpretation of Cassini gravity. Geophysical Research Letters, 42(7), 2137-2143. https://doi.org/10.1002/2015GL063384.

Milkovich, S. M., & Head III, J. W. (2006). Surface textures of Mars' north polar layered deposits: A framework for interpretation and future exploration. Mars, 2, 21-45.

Mohit, P.S., Greenhagen, B.T., McKinnon, W.B. (2004). Polar wander on Ganymede. Bulletin of the American astronomical society 36, 1084.

Moore, W. B., Schubert, G. (1996). New models of Ganymede's internal structure from Galileo observations. In Bulletin of the American Astronomical Society, 28, p. 1139.

Morrison, S. J., Thomas, P. C., Tiscareno, M. S., Burns, J. A., Veverka, J. (2009). Grooves on small saturnian satellites and other objects: Characteristics and significance. Icarus 204, 262–270. https://doi.org/10.1016/j.icarus.2009.06.003.

Murchie, S.L., Head, J.W. (1986). Global reorientation and its effect on tectonic patterns on Ganymede. Geophysical Research Letters 13 (4), 345-348. https://doi.org/10.1029/GL013i004p00345.

Murchie, S., Head, J.W. (1988). Possible breakup of Dark Terrain on Ganymede by large-scale shear faulting. Journal of Geophysical Research, 93 (B8), 8795-8824. https://doi.org/0148-0227/88/007B-4008505.00.

Murchie, S.L., Head, J.W., Plescia, J.B., 1990. Tectonic and volcanic evolution of dark terrain and its implications for the internal structure and evolution of Ganymede. J. Geophys. Res. Solid Earth 95 (B7), 10743–10768. https://doi.org/10.1029/JB095iB07p10743.

Nahm, A. L., & Kattenhorn, S. A. (2015). A unified nomenclature for tectonic structures on the surface of Enceladus. Icarus, 258, 67-81. https://doi.org/10.1016/j.icarus.2015.06.009.

Ng, F. S., & Zuber, M. T. (2006). Patterning instability on the Mars polar ice caps. Journal of Geophysical Research: Planets, 111(E2). https://doi.org/10.1029/2005JE002533.

Nimmo, F., Pappalardo, R.T. (2004). Furrow flexure and ancient heat flux on Ganymede. Geophysical Research Letters, 31. https://doi.org/10.1029/2004GL020763.

Nimmo, F. (2004). What is the young's modulus of ice? In: Workshop on Europa's Icy Shell: Past, Present, and Future.

Nimmo, F., & Pappalardo, R. T. (2006). Diapir-induced reorientation of Saturn's moon Enceladus. Nature, 441(7093), 614. https://doi.org/10.1038/nature04821.

Ojakangas, G. W., Stevenson, D. J. (1989). Thermal state of an ice shell on Europa. Icarus, 81 (2), 220-241. https://doi.org/10.1016/0019-1035(89)90052-3.

Olgin, J. G., Smith-Konter, B. R., & Pappalardo, R. T. (2011). Limits of Enceladus's ice shell thickness from tidally driven tiger stripe shear failure. Geophysical Research Letters, 38(2). https://doi.org/10.1029/2010GL044950.

Orosei, R., Lauro, S. E., Pettinelli, E., Cicchetti, A., Coradini, M., Cosciotti, B., ... & Soldovieri, F. (2018). Radar evidence of subglacial liquid water on Mars. Science, 361(6401), 490-493. https://doi.org/10.1126/science.aar7268.

Pappalardo, R.T., Greeley, R., 1995. A review of the origins of subparallel ridges and troughs: generalized morphological predictions from terrestrial models. J. Geophys. Res. Planets 100 (E9), 18985–19007. https://doi.org/10.1029/94JE02638.

Pappalardo, R.T., Head, J.W., Collins, G.C., Kirk, R.L., Neukum, G., Oberst, J., Giese, B., Greeley, R., Chapman, C.R., Helfenstein, P., Moore, J.M., McEwen, A., Tufts, B.R., Senske, D.A., Breneman, H.H., Klaasen, K., 1998. Grooved terrain on Ganymede: first results from Galileo high-resolution imaging. Icarus 135, 276–302. https://doi.org/10.1006/icar.1998.5966.

Pappalardo, R.T., Belton, M.J.S., Breneman, H.H., Carr, M.H, Chapman, C.R., Collins, G.C., denk, T., Fagents, S., Geissler, P.E., Giese, B., Greeley, R., Greenberg, R., Head, J.W., Helfenstein, P., Hoppa, G., Kadel, S.D., Klaasen, K.P., Klemaszewski, J.E., Magee, K., McEwen, A.S., Moore, J.M., Neukum, G., Phillips, C.B., Prockter, L.M., Schubert, G., Senske, D.A., Sullivan, R.J., Tufts, B.R., Turtle, E.P., Wagner, R., Williams, K.K. (1999). Does Europa have a subsurface ocean? Evaluation of the geological evidence. Journal of Geophysical Research: Planets 104 (E10), 24015-24055. https://doi.org/10.109/1998JE000628.

Pappalardo, R.T., Collins, G.C., Head III, J.W., Helfenstein, P., McCord, T.B., Moore, J.M., Prockter, L.M., Schenk, P.M., Spencer, J.R., 2004. Geology of Ganymede. In: Bagenal, F., Dowling, T., McKinnon, W.B. (Eds.), Jupiter - The Planet, Satellites, and Magnetosphere. Cambridge Univ. Press, Cambridge, U.K., pp. 363–396.

Pappalardo, R.T., Collins, G.C. (2005). Strained craters on Ganymede. Journal of Structural Geology 27 (5), 827-838. https://doi.org/10.1016/j.jsg.2004.11.010.

Pappalardo, R.T. (2006). Ridge and trough terrains on outer planet satellites. AGU Fall Meeting, 32A-02A2.

Parish, T. R. (1984). A numerical study of strong katabatic winds over Antarctica. Monthly weather review, 112(3), 545-554. https://doi.org/10.1175/1520-0493(1984)112<0545:ANSOSK>2.0.CO;2.

Parish, T. R., and D. H. Bromwich (1986). The inversion wind pattern over West Antarctica. Mon. Weather Rev. 114, 849–860. https://doi.org/10.1175/1520-0493(1986)114<0849:TIWPOW>2.0.CO;2.

Parish, T. R. (1988). Surface winds over the Antarctic continent: A review. Reviews of Geophysics, 26(1), 169-180. https://doi.org/10.1029/RG026i001p00169.

Parkinson, C. D., Liang, M. C., Yung, Y. L., & Kirschivnk, J. L. (2008). Habitability of Enceladus: planetary conditions for life. Origins of Life and Evolution of Biospheres, 38(4), 355-369. https://doi.org/10.1007/s11084-008-9135-4.

Parmentier, E. M. and J. W. Head (1979). Internal processes affecting surfaces of low-density satellites: Ganymede and Callisto. J. Geophys. Res., 84, pp. 6263-6276. https://doi.org/10.1029/JB084iB11p06263.

Parmentier, E.M., Squyres, S.W., Head, J.W., Allison, M.L. (1982). The tectonics of Ganymede. Nature 295, 290-293. https://doi.org/10.1038/295290a0.

Passey, Q.R., Shoemaker, G., 1982. Craters and basins on Ganymede and Callisto: morphological indicators of crustal evolution. In: Morrison, D. (Ed.), Satellites of Jupiter. Univ. of Ariz. Press, Tucson, pp. 379–434.

Patterson, G.W., Collins, G.C., Head, J.W., Pappalardo, R.T., Prockter, L.M., Lucchitta, B.K., Kay, J.P., 2010. Global geological mapping of Ganymede. Icarus 207 (2), 845–867. https://doi.org/10.1016/j.icarus.2009.11.035.

Patthoff, D.A., & Kattenhorn, S. (2011). A fracture history on Enceladus provides evidence for a global ocean. Geophysical Research Letter, 38(18). https://doi.org/10.1029/2011GL048387.

Pelletier, J. D. (2004). How do spiral troughs form on Mars?. Geology, 32(4), 365-367. https://doi.org/10.1130/G20228.2.

Petrovic, J.J. (2003). Review Mechanical properties of ice and snow. Journal of Materials Science 38, 1– 6. https://doi.org/10.1023/A:1021134128038.

Pettinelli, E., Cosciotti, B., Di Paolo, F., Lauro, S. E., Mattei, E., Orosei, R., & Vannaroni, G. (2015). Dielectric properties of Jovian satellite ice analogs for subsurface radar exploration: A review. Reviews of Geophysics,53(3), 593–641. https://doi.org/10.1002/2014RG000463.

Pfiffner, O.A. (2017). Thick-Skinned and Thin-Skinned Tectonics: A Global Perspective. Geosciences, 7, 71. https://doi.org/10.3390/geosciences7030071.

Phillips, R. J., Zuber, M. T., Smrekar, S. E., Mellon, M. T., Head, J. W., Tanaka, K. L., ... & Safaeinili, A. (2008). Mars north polar deposits: Stratigraphy, age, and geodynamical response. Science, 320(5880), 1182-1185. https://doi.org/10.1126/science.1157546.

Phillips, E., Finlayson, A., & Jones, L. (2013). Fracturing, block faulting, and moulin development associated with progressive collapse and retreat of a maritime glacier: Falljökull, SE Iceland. Journal of Geophysical Research: Earth Surface, 118(3), 1545-1561. https://doi.org/10.1002/jgrf.20116.

Philpott, R. (1988). Formation of sulci, grooves and associated stress regimes on Ganymede. Lunar and Planetary Science Conference 19, 919.

Picardi, G., Plaut, J. J., Biccari, D., Bombaci, O., Calabrese, D., Cartacci, M., ... & Federico, C. (2005). Radar soundings of the subsurface of Mars. science, 310(5756), 1925-1928. https://doi.org/10.1126/science.1122165.

Pinheiro, M. R., Cianfarra, P., Villela, F. N. J., & Salvini, F. (2019). Tectonics of the Northeastern border of the Parana Basin (Southeastern Brazil) revealed by lineaments domain analysis. Journal of South American Earth Sciences, 102231. https://doi.org/10.1016/j.jsames.2019.102231.

Pischiutta, M., Anselmi, M., Cianfarra, P., Rovelli, A., & Salvini, F. (2013). Directional site effects in a non-volcanic gas emission area (Mefite d'Ansanto, southern Italy): Evidence of a local transfer fault transversal to large NW–SE extensional faults?. Physics and Chemistry of the Earth, Parts A/B/C, 63, 116-123. https://doi.org/10.1016/j.pce.2013.03.008.

Pizzi, A., Di Domenica, A., Komatsu, G., Cofano, A., Mitri, G., Bruzzone, L., 2017. Spreading vs. rifting as modes of extensional tectonics on the globally expanded Ganymede. Icarus 288, 148–159. https://doi.org/10.1016/j.icarus.2017.01.034.

Plaut, J. J., Picardi, G., Safaeinili, A., Ivanov, A. B., Milkovich, S. M., Cicchetti, A., ... & Clifford, S. M. (2007). Subsurface radar sounding of the south polar layered deposits of Mars. science, 316(5821), 92-95. https://doi.org/10.1126/science.1139672.

Plewes, L. A., and Hubbard, B. (2001). A review of the use of radio-echo sounding in glaciology. Progress in Physical Geography, 25(2), 203-236. https://doi.org/10.1177/030913330102500203.

Porco, C.C., Helfenstein, P., Thomas, P.C., Ingersoll, A.P., Wisdom, J., West, R., et al. (2006). Cassini observes the active south pole of Enceladus. Science 311, 1393–1401. https://doi.org/10.1126/science.1123013.

Porco, C., DiNino, D., & Nimmo, F. (2014). How the geysers, tidal stresses, and thermal emission across the South Polar terrain of Enceladus are related. Astron J 148. https://doi.org/10.1088/0004-6256/148/3/45.

Postberg, F., Khawaja, N., Abel, B., Choblet, G., Glein, C. R., Gudipati, M. S., et al. (2018). Macromolecular organic compounds from the depths of Enceladus. Nature, 558(7711), 564. https://doi.org/10.1038/s41586-018-0246-4.

Prieto-Ballesteros, O., Bonales, L.J., Munoz-Iglesias, V. (2012). Potential habitability of the Jupiter system: deep aqueous environments in Europa, Ganymede and Callisto. Highlights of Spanish Astrophysics VII, Proceedings of the X Scientific Meeting of the Spanish Astronomical Society.

Prockter, L.M., Head, J.W., Pappalardo, R.T., Senske, D.A., Neukum, G., Wagner, R., Wolf, U., Oberst, J.O., Giese, B., Moore, J.M., Chapman, C.R., Helfenstein, P., Greeley, R., Breneman, H., Belton, M.J.S., 1998. Dark terrain on Ganymede: geological mapping and interpretation of Galileo Regio at high resolution. Icarus 135 (1), 317–344. https://doi.org/10.1006/icar.1998.5981.

Prockter, L.M., Figueredo, P.H., Pappalardo, R.T., Head, J.W., Collins, G.C., 2000. Geology and mapping of dark terrain on Ganymede and implications for grooved terrain formation. J. Geophys. Res. Planets 105 (E9), 22519–22540. https://doi.org/10.1029/1999JE001179.

Prockter, L. M., Thomas, P., Robinson, M., Joseph, J., Milne, A., Bussey, B., Veverka, J., Cheng, A. (2002). Surface Expressions of Structural Features on Eros. Icarus 155, 75–93. https://doi.org/10.1006/icar.2001.6770.

Prockter, L. M. (2005). Ice in the solar system. Johns Hopkins APL Technical Digest, 26(2), 175-188.

Putzig, N. E., Smith, I. B., Perry, M. R., Foss II, F. J., Campbell, B. A., Phillips, R. J., & Seu, R. (2018). Three-dimensional radar imaging of structures and craters in the Martian polar caps. Icarus, 308, 138-147. https://doi.org/10.1016/j.icarus.2017.09.023.

Ramsay, J.G., 1980. Shear zone geometry: a review. J. Struct. Geol. 2 (1–2), 83–99. https://doi.org/10.1016/0191-8141(80)90038-3.

Riedel, W., 1929. Zur Mechanik geologischer Bruchersche, Centralblatt fur Mineralogie Geologie and Palaeontologie, Abhandlung B. pp. 354–368.

Rignot, E., Mouginot, J., & Scheuchl, B. (2011). Ice flow of the Antarctic ice sheet. Science, 333(6048), 1427-1430. https://doi.org/10.1126/science.1208336.

Roberts, J. H. (2016). Evolution of the Ice Shell on Enceladus. In Lunar and Planetary Science Conference, 47, 1503.

Robson, A. G., King, R. C., & Holford, S. P. (2017). Structural evolution of a gravitationally detached normal fault array: Analysis of 3D seismic data from the Ceduna Sub-Basin, Great Australian Bight. Basin Research, 29(5), 605-624. https://doi.org/10.1111/bre.12191.

Rodgers, J. (1949). Evolution of thought on structure of middle and southern Appalachians. Bulletin of the American Association of Petroleum Geologists, 33(10), 1643-1654.

Rossetti, F., Storti, F., Salvini, F., 2000. Cenozoic noncoaxial transtension along the western shoulder of the Ross Sea, Antarctica, and the emplacement of McMurdo dyke arrays. Terra Nova 12 (2), 60–66. https://doi.org/10.1111/j.1365-3121.2000.00270.x.

Rossi, C., Cianfarra, P., Salvini, F., Mitri, G., Massé, M. (2018). Evidence of transpressional tectonics on the Uruk Sulcus region, Ganymede. Tectonophysics 749, 72–87. https://doi.org/10.1016/j.tecto.2018.10.026.

Rott, H., Stuefer, M., Siegel, A., Skvarca, P., & Eckstaller, A. (1998). Mass fluxes and dynamics of Moreno glacier, southern Patagonia icefield. Geophysical research letters, 25(9), 1407-1410. https://doi.org/10.1029/98GL00833.

Salvini, F., 1985. Slope-intercept-density plots - a new method for line detection in images. In: International Geoscience and Remote Sensing Symposium (IGARSS'85), Amherst, MA, pp. 715–720.

Salvini, F., Billi, A., & Wise, D. U. (1999). Strike-slip fault-propagation cleavage in carbonate rocks: the Mattinata Fault Zone, Southern Apennines, Italy. Journal of Structural Geology, 21(12), 1731-1749. https://doi.org/10.1016/S0191-8141(99)00120-0.

Salvini, F., F. Storti, and K. McClay (2001), Self-determining numerical modeling of compressional fault-bend folding, Geology, 29, 839–842, https://doi.org/10.1130/0091-7613(2001)029<0839:SDNMOC>2.0.CO;2.

Salvini, F., 2004. Daisy 3: The Structural Data Integrated System Analyzer Software. University of Roma Tre, Rome. http://host.uniroma3.it/progetti/fralab.

Salvini, F., and Storti, F. (2004). Active-hinge-folding-related Deformation and its Role in Hydrocarbon Exploration and Development Insights from HCA Modeling. American Association of Petroleum Geologists 82, 453-472.

Salvini, F., 2013. The fault zone deformation architecture. In: 40th Workshop of the International School of Geophysics on properties and processes of crustal fault zones, Erice, Italy, pp. 18–24. ftp://ingv.it/pro/web_ingv/Erice2013_40th%20Course.pdf/Salvini_Erice2013.pdf.

Salvini, F. (2019). Daisy 3: The Structural Data Integrated System Analyzer Software. University of Roma Tre, Rome. http://host.uniroma3.it/progetti/fralab.

Sarid, A. R., Greenberg, R., Hoppa, G. V., Hurford, T. A., Tufts, B. R., & Geissler, P. (2002). Polar wander and surface convergence of Europa's ice shell: Evidence from a survey of strike-slip displacement. Icarus, 158(1), 24-41. https://doi.org/10.1006/icar.2002.6873.

Sarson, G.R., Jones, C.A., Zhang, K., Schubert, G., 1997. Magnetoconvection dynamos and the magnetic fields of Io and Ganymede. Science 276 (5315), 1106–1108. https://doi.org/10.1126/science.276.5315.1106.

Scheiber, T., Fredin, O., Viola, G., Jarna, A., Gasser, D., Łapińska-Viola, R., 2015. Manual extraction of bedrock lineaments from high-resolution LiDAR data: methodological bias and human perception. GFF 137 (4), 362–372. https://doi.org/10.1080/11035897.2015.1085434.

Schenk, P., McKinnon, W.B. (1987). Ring geometry on Ganymede and Callisto. Icarus 72 (1), 209-234. https://doi.org/10.1016/0019-1035(87)90126-6.

Schenk, P.M., McKinnon, W.B., 1991. Dark-ray and dark-floor craters on Ganymede, and the provenance of large impactors in the Jovian system. Icarus 89 (2), 318–346. https://doi.org/10.1016/0019-1035(91)90181-R.

Schenk, P.M., Moore, J.M., 1995. Volcanic constructs on Ganymede and Enceladus: topographic evidence from stereo images and photoclinometry. J. Geophys. Res. Planets 100 (E9), 19009–19022. https://doi.org/10.1029/95JE01854.

Schenk, P. M., & McKinnon, W. B. (2009). One-hundred-km-scale basins on Enceladus: Evidence for an active ice shell. Geophysical Research Letters, 36(16). https://doi.org/10.1029/2009GL039916.

Schenk, P. M., Clark, R. N., Howett, C. J., Verbiscer, A. J., & Waite, J. H. (Eds.). (2018). Enceladus and the icy moons of Saturn. University of Arizona Press.

Schubert, G., Zhang, K., Kivelson, M.G., Anderson, J.D., 1996. The magnetic field and internal structure of Ganymede. Nature 384 (6609), 544. https://doi.org/10.1038/384544a0.

Schubert, G., Turcotte, D.L., Olson, P., 2001. Mantle Convection in the Earth and Planets. Cambridge University Press, Cambridge, UK.

Schubert, G., Anderson, J.D., Spohn, T., McKinnon, W.B., 2004. Interior composition, structure and dynamics of the Galilean satellites. In: Bagenal, Fran, Dowling, Timothy E., McKinnon, William B. (Eds.), Jupiter: The Planet, Satellites and Magnetosphere. 1. Cambridge University Press, Cambridge, UK, pp. 281–306.

Scipioni, F., Schenk, P., Tosi, F., D'Aversa, E., Clark, R., Combe, J. P., & Dalle Ore, C. M. (2017). Deciphering sub-micron ice particles on Enceladus surface. Icarus, 290, 183-200. https://doi.org/10.1016/j.icarus.2017.02.012.

Scott, R. J., and Lister, G. S. (1992). Detachment faults: Evidence for a low-angle origin. Geology, 20(9), 833-836. https://doi.org/10.1130/0091-7613(1992)020<0833:DFEFAL>2.3.CO;2.

Seifert, F., Cameron, M.E., Smith-Konter, B.R., Pappalardo, R.T., Collins, G.C., 2015. Global morphological mapping of strike-slip structures on Ganymede. In: Lunar and Planetary Science Conference. 46. pp. 2985.

Seu, R., Phillips, R. J., Biccari, D., Orosei, R., Masdea, A., Picardi, G., ... & Smrekar, S. E. (2007). SHARAD sounding radar on the Mars Reconnaissance Orbiter. Journal of Geophysical Research: Planets, 112(E5). https://doi.org/10.1029/2006JE002745.

Shoemaker, E.M., Wolfe, R.F., 1982a. Cratering time scales for the Galilean satellites. In: Morrison, D. (Ed.), Satellites of Jupiter. Univ. of Arizona Press, Tucson, pp. 277–339.

Shoemaker, E.M., Lucchitta, B.K., Wilhelms, D.E., Plescia, J.B., Squyres, S.W. (1982b). The geology of Ganymede. In: Morrison, D. (Ed.), Satellites of Jupiter. University of Arizona Press, Tucson, 435–520.

Showman, A.P., Malhotra, R., 1997. Tidal evolution into the Laplace resonance and the resurfacing of Ganymede. Icarus 127 (1), 93–111. https://doi.org/10.1006/icar.1996.5669.

Smith, B.A., Soderblom, L.A., Johnson, T.V., Ingersoll, A.P., Collins, S.A., Shoemaker, E.M., Hunt, G.E., Masursky, H., Carr, M.H., Davies, M.E., Cook, A.F., Boyce, J., Danielson, G.E., Owen, T., Sagan, C., Beebe, R.F., Veverka, J., Strom, R.G., McCauley, J.F., Morrison, D.,Briggs, G.A., Suomi, V.E. (1979a). The Jupiter system through the eyes of Voyager 1. Science 204 (4396), 951-972. https://doi.org/10.1126/science.204.4396.51

Smith, B.A., Soderblom, L.A., Beebe, R.F., Boyce, J.M., Briggs, G.A., Carr, M.H., Collins, S.A., Cook, A.F., Danielson, G.E., Davies, M.E., Hunt, G.E., Ingersoll, A.P., Johnson, T.V., Masursky, H., McCauley, J.F., Morisson, D., Owen, T., Sagan, C., Shoemaker, E.M., Strom, R.G., Suomi, V.E., Veverka, J. (1979b). The galilean satellites and Jupiter: voyager 2 imaging science results. Science 206, 927-950. https://doi.org/10.1126/science.204.4396.951.

Smith, I. B., & Holt, J. W. (2010). Onset and migration of spiral troughs on Mars revealed by orbital radar. Nature, 465(7297), 450. https://doi.org/10.1038/nature09049.

Smith, I. B., & Holt, J. W. (2015). Spiral trough diversity on the north pole of Mars, as seen by Shallow Radar (SHARAD). Journal of Geophysical Research: Planets, 120(3), 362-387. https://doi.org/10.1002/2014JE004720.

Smith, I. B., Putzig, N. E., Holt, J. W., & Phillips, R. J. (2016). An ice age recorded in the polar deposits of Mars. Science, 352(6289), 1075-1078. https://doi.org/10.1126/science.aad6968.

Soderblom, L. A., M. C. Malin, J. A. Cutts, and B. C. Murray 1973. Mariner 9 observations of the surface of Mars in the north polar region. J. Geophys. Res. 78, 4197–4210. https://doi.org/10.1029/JB078i020p04197.

Sohl, F., Spohn, T., Breuer, D., Nagel, K., 2002. Implications from Galileo observations on the interior structure and chemistry of the Galilean satellites. Icarus 157 (1), 104–119. https://doi.org/10.1006/icar.2002.6828.

Souček, O., Bourgeois, O., Pochat, S., & Guidat, T. (2015). A 3 Ga old polythermal ice sheet in Isidis Planitia, Mars: Dynamics and thermal regime inferred from numerical modeling. Earth and Planetary Science Letters, 426, 176-190. https://doi.org/10.1016/j.epsl.2015.06.038.

Souček, O., Běhounková, M., Čadek, O., Hron, J., Tobie, G., & Choblet, G. (2019). Tidal dissipation in Enceladus' uneven, fractured ice shell. Icarus, 328, 218-231. https://doi.org/10.1016/j.icarus.2019.02.012.

Spencer, J. R., Pearl, J. C., Segura, M., Flasar, F. M., Mamoutkine, A., Romani, P., et al. (2006). Cassini encounters Enceladus: Background and the discovery of a south polar hot spot. science, 311(5766), 1401-1405. https://doi.org/10.1126/science.1121661.

Spencer, J. R., & Nimmo, F. (2013). Enceladus: An active ice world in the Saturn system. Annual Review of Earth and Planetary Sciences, 41, 693-717.

Spiga, A. (2011). Elements of comparison between Martian and terrestrial mesoscale meteorological phenomena: Katabatic winds and boundary layer convection. Planetary and Space Science, 59(10), 915-922. https://doi.org/10.1016/j.pss.2010.04.025.

Spiga, A., and Smith, I. (2018). Katabatic jumps in the Martian northern polar regions. Icarus, 308, 197-208. https://doi.org/10.1016/j.icarus.2017.10.021.

Squyres, S. W. (1979). The evolution of dust deposits in the Martian north polar region. Icarus, 40(2), 244-261. https://doi.org/10.1016/0019-1035(79)90070-8.

Squyres, S.W., 1980. Volume changes in Ganymede and Callisto and the origin of grooved terrain. Geophys. Res. Lett. 7 (8), 593–596. https://doi.org/10.1029/GL007i008p00593.

Squyres., S.W., Croft, S.K. (1986). The tectonics of icy satellites. IAU Colloq. 77: Some Background about Satellites, 293-341.

Storti, F., Holdsworth, R. E., Salvini, F., Editors (2003). Intraplate strike-slip deformation belts. Geological Society, London, Special Publication 210, 302pp.

Tabacco, I. E., Cianfarra, P., Forieri, A., Salvini, F., & Zirizotti, A. (2006). Physiography and tectonic setting of the subglacial lake district between Vostok and Belgica subglacial highlands (Antarctica). Geophysical Journal International, 165(3), 1029-1040. https://doi.org/10.1111/j.1365-246X.2006.02954.x.

Tajeddine, R., Soderlund, K. M., Thomas, P. C., Helfenstein, P., Hedman, M. M., Burns, J. A., & Schenk, P. M. (2017). True polar wander of Enceladus from topographic data. Icarus, 295, 46-60. https://doi.org/10.1016/j.icarus.2017.04.019.

Tanaka, K., and Kolb, E. (2001). Geologic history of the polar regions of Mars based on Mars Global Surveyor data. I. Noachian and Hesperian Periods. Icarus 154, 22–39. https://doi.org/10.1006/icar.2001.6675.

Tanaka, K. L., Rodriguez, J. A. P., Skinner Jr, J. A., Bourke, M. C., Fortezzo, C. M., Herkenhoff, K. E., ... & Okubo, C. H. (2008). North polar region of Mars: Advances in stratigraphy, structure, and erosional modification. Icarus, 196(2), 318-358. https://doi.org/10.1016/j.icarus.2008.01.021.

Tchalenko, J.S., 1970. Similarities between shear zones of different magnitudes. Geol. Soc. Am. Bull. 81 (6), 1625–1640. https://doi.org/10.1130/0016-7606(1970)81[1625:SBSZOD]2.0.CO;2.

Tchalenko, J.S., Ambraseys, N.N., 1970. Structural analysis of the Dasht-e Bayaz (Iran) earthquake fractures. Geol. Soc. Am. Bull. 81 (1), 41–60. https://doi.org/10.1130/0016-7606(1970)81[41:SAOTDB]2.0.CO;2.

Thomas, P. C. (1989). The shapes of small satellites. Icarus, 77 (2), 248-274. https://doi.org/10.1016/0019-1035(89)90089-4.

Thomas, P. C., Burns, J. A., Helfenstein, P., Squyres, S., Veverka, J., Porco, C., et al. (2007). Shapes of the saturnian icy satellites and their significance. Icarus, 190(2), 573-584. https://doi.org/10.1016/j.icarus.2007.03.012.

Thomas, P.C., Tajeddine, R., Tiscareno, M.S., Burns, J.A., Joseph, J., Loredo, T.J., et al. (2016). Enceladus's measured physical libration requires a global subsurface ocean. Icarus 264, 37–47. https://doi.org/10.1016/j.icarus.2015.08.037.

Tobie, G., Čadek, O., & Sotin, C. (2008). Solid tidal friction above a liquid water reservoir as the origin of the south pole hotspot on Enceladus. Icarus, 196(2), 642-652. https://doi.org/10.1016/j.icarus.2008.03.008.

Tobie, G. (2015). Planetary science: Enceladus' hot springs. Nature, 519(7542), 162. https://doi.org/10.1038/519162a.

Turcotte, D.L., 1997. Fractals and Chaos in Geology and Geophysics. Cambridge Univ. Press, New York (398 pp.).

Turcotte, D.L., Schubert, G., 2002. Geodynamics. Cambridge University Press, Cambridge, UK0 521 66624 4 (456 pp.).

Utsi, E. C. (2017). Ground Penetrating Radar: Theory and Practice. Butterworth-Heinemann.

Van der Pluijm, B., Marshak, S., 1997. Earth Structure. McGrawHill, New York (495 pp.).

Vance, S. D., Panning, M. P., Stähler, S., Cammarano, F., Bills, B. G., Tobie, G., Kamata, S., Kedar, S., Sotin, C., Pike, W. T., Lorenz, R., Huang, H., Jackson, J. M., Banerdt, B. (2018). Geophysical investigations of habitability in ice-covered ocean worlds. Journal of Geophysical Research: Planets, 122. https://doi.org/10.1002/2017JE005341.

Vendeville, B.C., Jackson, M.P.A. (1992). The fall of diapirs during thin-skinned extension. Marine and Petroleum Geology, 9. https://doi.org/10.1016/0264-8172(92)90048-J.

Vening Meinesz, F. A. (1947). Shear patterns in the earth's crust. Transactions of the American Geophysical Union, 28, 1-61.

Walsh, J. J., and Watterson, J. (1991). Geometric and kinematic coherence and scale effects in normal fault systems. Geological Society, London, Special Publications, 56(1), 193-203. https://doi.org/10.1144/GSL.SP.1991.056.01.13.

Watters, T.R., Schultz, R.A. (Eds.), 2010. Planetary Tectonics. Cambridge University Press (518 pp.).

Weijermars, R. (1986). The polar spirals of Mars may be due to glacier surges deflected by Coriolis forces. Earth and planetary science letters, 76(3-4), 227-240. https://doi.org/10.1016/0012-821X(86)90075-0.

Wernicke, B. (1981). Low-angle normal faults in the Basin and Range Province: nappe tectonics in an extending orogen. Nature, 291(5817), 645. https://doi.org/10.1038/291645a0.

Whipple, F. L. (1950). A comet model. I. The acceleration of Comet Encke. The Astrophysical Journal, 111, 375-394.

Williams, G., and Vann, I. (1987). The geometry of listric normal faults and deformation in their hangingwalls. Journal of Structural Geology, 9(7), 789-795. https://doi.org/10.1016/0191-8141(87)90080-0.

Wise, D.U., 1982. Linesmanship and the practice of linear geo-art. Geol. Soc. Am. Bull. 93 (9), 886–888. https://doi.org/10.1130/0016-7606(1982)93<886:LATPOL>2.0.CO;2.

Wise, D.U., Funiciello, R., Parotto, M., Salvini, F., 1985. Topographic lineament swarms: clues to their origin from domain analysis of Italy. Geol. Soc. Am. Bull. 96 (7), 952–967. https://doi.org/10.1130/0016-7606(1985)96<952:TLSCTT>2.0.CO;2.

Woodward, N. B., Boyer, S. E., & Suppe, J. (1989). Balanced geological cross-sections. Short Course in Geology, 6, 132.

Yin, A., Hansen, V., 2014. Styles of strike-slip faulting in the solar system and the corresponding modes of thermal-boundary-layer deformation. In: Lunar and Planetary Science Conference. 45. pp. 1657.

Yin, A., & Pappalardo, R.T. (2015). Gravitational spreading, bookshelf faulting, and tectonic evolution of the South Polar Terrain of Saturn's moon Enceladus. Icarus 260, 409–439. https://doi.org/10.1016/j.icarus.2015.07.017.

Young, R.E. (1998). The Galileo probe mission to Jupiter: Science overview. Journal of Geophysical Research: Planets 103 (E10), 22775-22790. https://doi.org/10.1029/98JE01051.

Zahnle, K., Dones, L., Levison, H.F. (1998). Cratering Rates on the Galilean Satellites. Icarus 136, 202–222. https://doi.org/10.1006/icar.1998.6015.

Zahnle, K., Schenk, P., Levison, H., Dones, L. (2003). Cratering rates in the outer Solar System. Icarus 163 (2), 263-289. https://doi.org/10.1016/S0019-1035(03)00048-4.

Zeng, Z., Xie, H., Birnbaum, S., Liu, L., & Yang, W. (2007, July). New insight on the origin of spiral troughs in martian polar ice caps. In Seventh International Conference on Mars (Vol. 1353, p. 3368).

Zeng, Z., Putzig, N. E., Xie, H., Birnbaum, S. J., Ackely, S. F., & Liu, L. (2008, March). Evidence of fractures in NPLD and their significance to the formation of Martian polar spiral troughs. In Lunar and Planetary Institute Science Conference Abstracts (Vol. 39, p. 2179).

STRUCTURAL GEOLOGY OF GANYMEDE REGIONAL GROOVE SYSTEMS (60°N - 60°S)

Rossi Costanza, Cianfarra Paola, Salvini Francesco

Dipartimento di Scienze, Università degli Studi Roma Tre

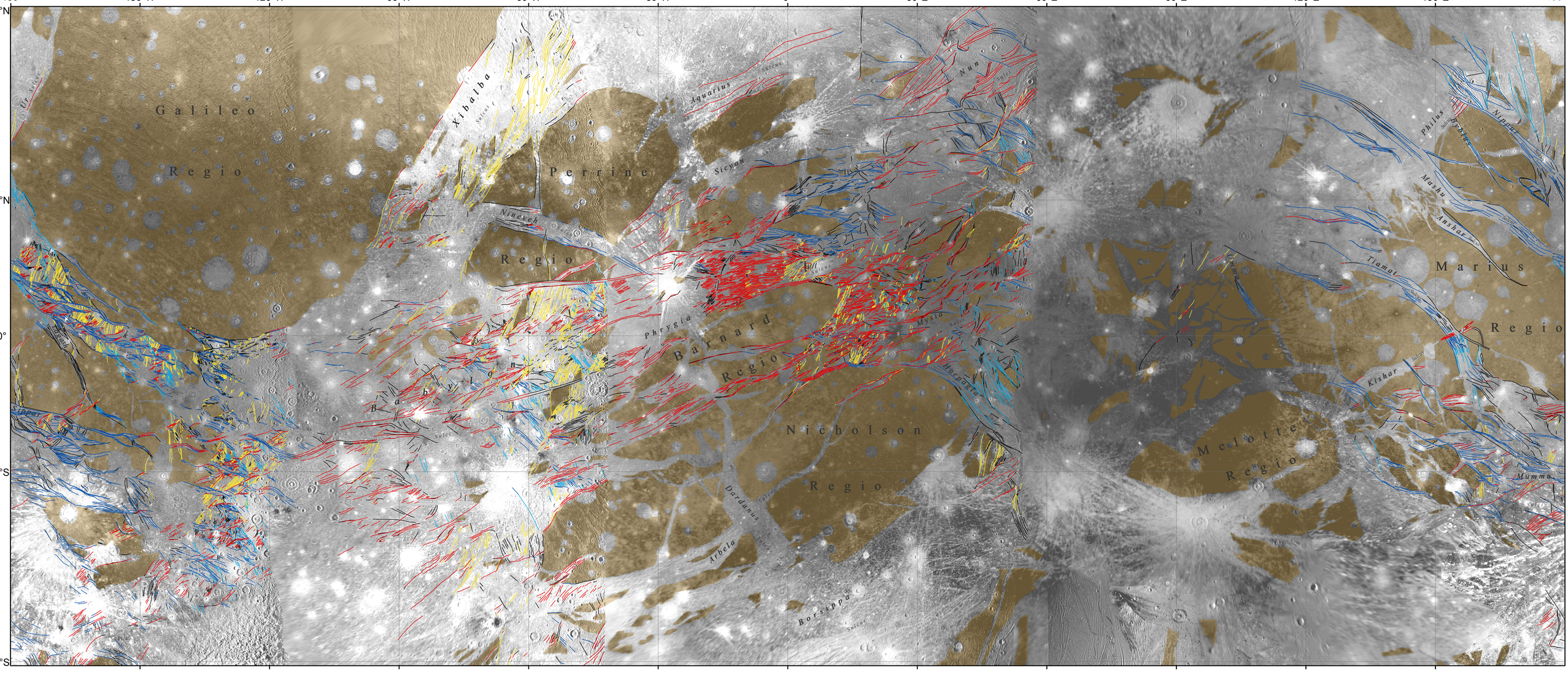

SCALE 1:10 000 000 (at the equator)

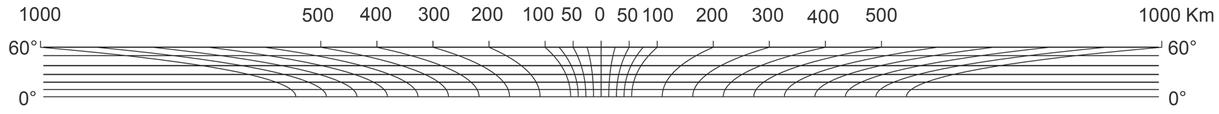

Mercator Projection

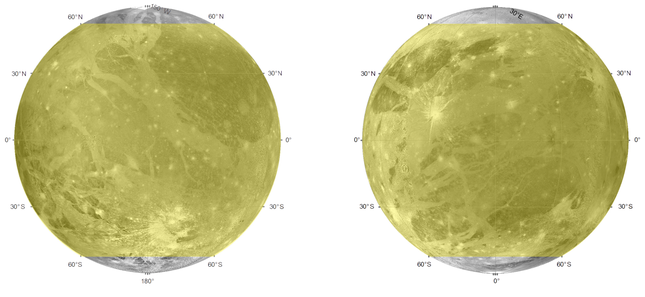

Locator map
Ganymede orthographic projection of the leading (left) and trailing (right) hemispheres.
The investigated area is represented in yellow.

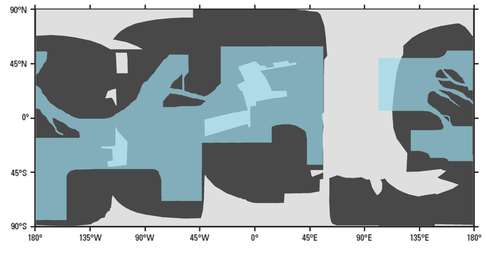

Image of high-resolution (dark grey) and low-resolution (light grey) of the basemap mosaic.
The light blue color delimits the investigated area.
(Modified from Patterson et al., 2010).

Terrains

- Light Terrain
- Dark Terrain

Grooves

- Super-system NE
- Super-system WNW
- Super-system NW
- Super-system N-S
- Unclassified

Light and dark terrain place names used on map follow the International Astronomical Union nomenclature

Dark terrain boundaries derive from USGS global geologic map of Ganymede (Collins et al., 2013)

Basemap from USGS Ganymede Voyager and Galileo Global Mosaics (https://astrogeology.usgs.gov)